Implicit Large Eddy Simulation of Environmental Urban Flows

Charikleia Papachristou

Submitted for the Degree of Ph.D.

Department of Aerospace Sciences
Cranfield University
Cranfield, UK

Cranfield University

School of Engineering

PhD

Academic Year: 2009-2010

Charikleia Papachristou

Implicit Large Eddy Simulation of Environmental Urban Flows

Supervisors: Dimitris Drikakis, Evgeniy Shapiro

July 18, 2010

Abstract

MANY environmental flows are turbulent flows. Depending on the physical aspects of the wind and the urban topology, turbulence might result into unfavourable or even dangerous conditions for the pedestrians. Turbulence can also play a very important role in the transport of toxic pollutants from accidental or intentional releases. Thus, it is vital to understand its complex characteristics so that its features are accurately predicted when computational methods are used. Real urban environment involving separation and reattachment regions provides an excellent testcase for investigating such complex flows.

This thesis is focused on analysing the physics involved in flows around building models pertinent to environmental flows in urban areas and to evaluate the applicability of Implicit Large-Eddy Simulation in simulating the specific type of flows. For this purpose, a number of high resolution schemes in the context of Implicit Large-Eddy Simulation (each representing different degrees of spatial discretisation accuracy) was assessed.

The evaluation of the schemes involved direct validation against experimental data as well as comparisons with DNS and LES data regarding flows within roughness element arrays in staggered arrangements. Initially, the flow within an uniform height cubical matrix was simulated. Four numerical schemes were tested in three different grid resolutions. The results were found in very good agreement with the Laser Doppler Anemometry data and they even exhibit DNS-like characteristics in specific locations of comparisons. Thus, it was concluded that high order spatial discretisation schemes allow the accurate representation of reality even in relatively coarse computational meshes.

The second case under investigation involved flows within a more realistic representation of urban topology. Results obtained within an array of sixteen elements with five different heights reveal that although the roughness of the area is increased, the wind's velocity profile above the obstacles shares almost the same slope as in the case of the array of the four cubical element.

It is believed that this thesis has expanded the range of applications in the context of Implicit Large Eddy Simulation using high resolution schemes and contributed in persuading the scientific community for its potentials.

Acknowledgements

FIRSTLY, I would like to thank my supervisor Professor Dimitris Drikakis for his guidance and constructive comments on my work throughout the years and also for offering me the opportunity of starting this PhD. Secondly, I would like to thank Dr. Evgeniy Shapiro who always provided essential inputs on my work but really went the extra mile during the final stages of this thesis.

Within our research group, FMACS, I am grateful to Dr. Ben Thornber and Dr. Ioannis Kokkinakis for sharing their knowledge in numerical methods and coding, and also Dr. Sanjay Patel for resolving further software issues. I would also like to thank Dr. Les Oswald for his prompt help, regardless time and day, every time a problem occurred when running on the HPC.

I also have to express my gratitude to Mr. David Brown and Dr. Mick Dawson, my managers in BHR Group Limited, for giving time to complete my PhD while working at the same time.

After three years sharing the same office, one year sharing the same house and working in the same company, I really have to thank first my very good friend Nikos. Thank you for cheering me up. Thanks must also go to the friends I made in England, Nafsika and Giota, for making the Cranfield experience more enjoyable. Special thanks must go to my friends in Greece, Alexandra, Maria and Evi, who always called to see how I was holding on.

On a more personal note, I would like to thank my partner Marco who entered my life during the most difficult time and he is still here.

Last but not least, I am deeply indebted to my family. Without their financial and psychological support I would never have made it so far. There were times, I was losing my faith but I continued trying because I knew that my family was always there. There is nothing that could replace that feeling. This thesis is dedicated to my parents, Fofo and Christos and my brother Danis.

Charikleia Papachristou

Contents

Abstract **i**

Acknowledgements **iii**

1 Introduction **1**

1.1 Atmospheric Flows 2

1.1.1 Urban Aerodynamics 2

1.1.2 Building Aerodynamics 6

1.2 Characteristics of Turbulence 13

1.2.1 The History of Turbulence 13

1.2.2 The Scales of Turbulence 13

1.2.3 Energy Spectrum Analysis 15

1.3 Numerical Models 16

1.4 Aims and Objectives 25

2 Numerical Approach **27**

2.1 Governing Equations 27

2.1.1 Cartesian And Curvilinear Equations in Matrix Form 30

2.2 The Finite Volume Concept 32

2.3 High-Resolution Methods 33

2.3.1 MUSCL Schemes 34

2.3.2 WENO Schemes 35

2.4 Low Mach Number Modification 37

2.5 Riemann Solver 38

2.5.1 HLLC Riemann solver 39

2.6 Time Marching 40

2.6.1 First-Order Runge-Kutta 40

2.6.2 Third-Order Runge Kutta 41
2.6.3 CFL Condition 41
2.7 Parallel Computing 42
2.8 Case Specific Methodology 42
2.8.1 Numerical Settings 43
2.8.2 Flow Statistics 44

3 Uniform Height Building Array 49
3.1 Numerical Details and Settings 49
3.2 Flow topology 53
3.3 Results 60
3.3.1 Grid Resolution Dependency 60
3.3.2 Numerical Scheme Dependency 64
3.3.3 Low Mach Correction Treatment Dependency 67
3.3.4 Spatial Averaged Velocity Profile 83
3.3.5 Computational Time Step Dependency 86
3.3.6 Energy Spectral Analysis 87
3.4 Summary 90

4 Random Height Building Array 93
4.1 Numerical Details and Settings 93
4.2 Flow Topology 95
4.3 Results 102
4.3.1 Constant Pressure Gradient Dependency 103
4.3.2 Reynolds Number Dependency 104
4.3.3 Obstacle Configuration Dependency 106
4.3.4 Energy Spectral Analysis 110
4.4 Summary 113

5 Conclusions and Future Work 115
5.1 Conclusions 115
5.2 Future Work 117

A Viscous Stress Tensor A-1

B Reynolds Stresses Comparisons With LDA Data **B-1**

C Reynolds Stresses Comparisons With DNS and LES Data **C-1**

List of Figures

1.1 Schematic representation of flow over an urban area [9] 3
1.2 Areas of interest in determination of the λ parameters. 5
1.3 Schematic representation of the flow field around a cube [53] 6
1.4 Areas of interest in determination of the R_B [73] 9
1.5 Modern building construction. 12
1.6 Schematic of a typical turbulent kinetic energy spectrum [62]. 16

2.1 Three-dimensional notation for a finite volume [30] 33
2.2 Decomposition of a two-dimensional global data domain over four processes [30]. 42
2.3 Computational starting point. 45
2.4 Effect of the computational time window. 46

3.1 Three dimensional illustration of the domain. 50
3.2 Computational grids. 52
3.3 Three dimensional impression of the flow. 54
3.4 Time averaged velocity contours and vectors in XY planes. 56
3.5 Time averaged velocity contours and vectors at y=0.5. 57
3.6 Q-criterion in MUSCL schemes - Isosurfaces of instantaneous Q=0.3. 58
3.7 Q-criterion in WENO schemes - Isosurfaces of instantaneous Q=0.3. . 59
3.8 Highlighted locations of comparison. 60
3.9 Grid resolution dependency of mean velocity profiles. 62
3.10 Grid resolution dependency of mean stress profiles. 63
3.11 Scheme dependency investigation at locations p0 and p1. 64
3.12 Scheme dependency investigation at locations p2 and p3. 65
3.13 Low Mach Correction effect at location p0. 68
3.14 Low Mach Correction effect at location p1. 69
3.15 Low Mach Correction effect at location p2. 70

3.16 Low Mach Correction effect at location p3. 71
3.17 Reynolds stresses at location p1. 72
3.18 Reynolds stresses at location p2. 73
3.19 Reynolds stresses at location p3. 74
3.20 ILES against DNS data at location p0. 75
3.21 ILES against DNS data at location p1. 76
3.22 ILES against DNS data at location p2. 77
3.23 ILES against DNS data at location p3. 78
3.24 ILES against LES data at location p0. 79
3.25 ILES against LES data at location p1. 80
3.26 ILES against LES data at location p2. 81
3.27 ILES against LES data at location p3. 82
3.28 Highlighted locations of spatial averaging. 85
3.29 LDA against ILES in terms of spatial averaged velocity profiles. . . . 86
3.30 Highlighted locations for calculating the energy spectrum. 87
3.31 Energy spectra. 89

4.1 Computational domain. 94
4.2 Computational grid. 94
4.3 Plan view of the building array. 95
4.4 Flow structure within the domain. 96
4.5 Flow structure in Unit A (y=0.14). 97
4.6 Flow structure in Unit B (y=0.5). 98
4.7 Flow structure in Unit C (y=0.5). 99
4.8 Flow structure in Unit D (y=0.5). 100
4.9 Instantaneous flow field visualisation using the Q-criterion - Isosurfaces of Q=0.2. 101
4.10 Highlighted locations of comparisons. 102
4.11 Pressure gradient dependency in terms of mean statistics. 103
4.12 Reynolds number dependency in terms of mean statistics. 105
4.13 Obstacle configuration dependency in terms of mean statistics. 106
4.14 Reynolds stresses at location (3,2) - Station A. 107
4.15 Reynolds stresses at location (1,6) - Station B. 108
4.16 Comparison between random and uniform element array. 108

4.17 Locations of spatial averaged mean velocity profiles. 110
4.18 Energy spectral in non uniform obstacle array. 112

B.1 Time-averaged crosswise stresses at location p1. . . . . B-1
B.2 Time-averaged spanwise stresses at location p1. . . . . B-2
B.3 Time-averaged streamwise stresses at location p2. . . . . B-3

C.1 Time-averaged turbulent intensities obtained with 2ndVA scheme at location p1. . . . . C-1
C.2 Time-averaged turbulent intensities obtained with 5thM scheme at location p1. . . . . C-2
C.3 Time-averaged turbulent intensities obtained with 5thWN scheme at location p1. . . . . C-3
C.4 Time-averaged turbulent intensities obtained with 9thWN scheme at location p1. . . . . C-4

List of Tables

1.1 Summary of the surface roughness length (z_0) based on the work of Davenport et al. [15]. The table has been cited originally in the work of Britter and Hanna [9]. 4

3.1 Summary of ILES grid characteristics. 51

3.2 Summary of the grid resolutions of referenced numerical studies [87], [14]. 51

3.3 LDA surface characteristics [12]. 84

3.4 ILES surface parameters using the 2-parameter fit over 25 points. . . . 85

3.5 ILES surface parameters using the 3-parameter fit over 4 points. . . . 85

3.6 ILES surface parameters using the 3-parameter fit. 86

3.7 Percentage difference between ILES and LDA surface parameters using 3-parameter curve fitting. 86

3.8 Surface parameters obtained from 25 points for evaluating the CFL condition. 87

3.9 Surface parameters obtained from 4 points for evaluating the CFL condition. 87

3.10 Energy spectra slopes for schemes in their original form. 88

3.11 Energy spectra slopes for schemes using Low Mach Correction Treatment. 88

3.12 CPU requirements in hours. 91

4.1 Surface parameters obtained from ILES data. 110

4.2 Percentage difference between ILES and HWA surface parameters. . . 110

4.3 Energy spectral slopes for random height array. 111

Nomenclature

Acronyms

CFL	Courant-Friedrichs-Lewy number
*CNS*3*D*	Compressible Navier Stokes Solver in 3D
DNS	Direct Numerical Simulation
RANS	Reynolds Averaged Navier Stokes
ENO	Essentially Non-Oscillatory Scheme
FFT	Fast Fourier Transform
HWA	Hot Wire Anemometer
HWA_RH	HWA for random height obstacle array
HLLC	Harten, Lax and van Leer solver with contact wave
ILES	Implicit Large Eddy Simulation
ILES_RH2	Two parameters fit for random height array
ILES_RH3	Three parameters fit for random height array
ILES_UH	ILES for uniform height obstacle array
ILES_UH2	Three parameters fit for uniform height array
ILES_UH3	Two parameters fit for uniform height array
LDA	Laser Doppler Anemometer
LDA_UH	LDA for uniform height obstacle array
LES	Large Eddy Simulation
MUSCL	Monotonic Upwind Scheme for Scalar Conservation Laws
WENO	Weighted Essentially Non-Oscillatory Scheme

Greek Symbols

α_k	Weight
$\bar{a}$	Averaged speed of sound
ϵ	Dissipation rate
γ	Ratio of specific heats
η	Kolmogorov length-scale
κ	Thermal conductivity coefficient
λ_T	Taylor micro-scale
μ	Dynamic viscosity coefficient
μ_∞	Characteristic reference viscosity
ν	Kinematic viscosity
ϕ	Limiter function
$\bar{\rho}$	Averaged speed of sound
ρ	Density
ρ_∞	Characteristic reference density
τ	Truncation error
τ^{sgs}	Subgrid scale stress tensor
τ_η	Kolmogorov time-scale
τ_{ij}	Viscous stresses component
$\bar{\omega_k}$	optimal weight
$\mathbf{\Omega}$	Vorticity
ω_k	Weight

Latin Symbols

$\mathbf{C}_{ij}$	Cross stress term
c_p	Specific heat at constant pressure
c_v	Specific heat at constant volume
$\mathbf{E}, \mathbf{F}, \mathbf{G}$	Inviscid flux vectors

e	Total energy per unit volume
e_i	Internal energy
$\mathbf{I}$	Unity tensor
$\mathbf{L}, \mathbf{M}, \mathbf{N}$	Viscous flux vectors
$\mathbf{L}_{ij}$	Leonard stress term
l_∞	Characteristic reference length
$\mathbf{m}$	Commutation error term
p	Pressure
Pr	Prandtl number
$\mathbf{q}$	Heat flux
Q	Second invariant of the velocity gradient tensor
$\mathbf{R}_{ij}$	Reynolds stress term
R	Gas constant
r	Ratio of the slopes of conserved variables
Re	Reynolds number
Re_τ	Roughness Reynolds number
$\mathbf{S}$	Stress tensor
S_*	Star wave speed
$S_{0,1,2}$	Stencils for the WENO reconstruction
S_L	Left wave speed
S_R	Right wave speed
Δt	Total step
$\mathbf{T}$	Viscous stress tensor
T	Temperature
t	Total time
$\mathbf{U}$	Array of conservative variables
$\mathbf{u}$	Velocity vector

u_η	Kolmogorov velocity-scale
u_∞	Characteristic reference velocity
u_τ	Total wall friction velocity

CHAPTER 1

Introduction

THIS thesis focuses on turbulent flows in urban environment. From the earlier Neolithic and Bronze Age up to modern period, the design of building structures was, most of the times, influenced by the need to withstand unfavourable wind and weather conditions. Nearly all of the most difficult phenomena to predict in the field of fluid dynamics are encountered in flows around stationary obstacles. Separation, reattachment and vortical structures are just a few of the flow features due to the complex interaction of wind and buildings. Depending on the wind's speed and direction, the local topology and the building characteristics, turbulence occurs in different scales contributing in various ways to the pedestrian comfort and safety. Additionally, in cases of accidental or intentional release of high concentrations of toxic chemicals, turbulence plays an important role in the dispersion and transport of the pollutant in the urban environment. Thus, it is of vital importance to understand and predict as accurately as possible the complex features of turbulence in order to determine a viable environment for the populace.

The subject of building aerodynamics has attracted enormous interest during the last decades and because of its complexity it is far from being closed. Important information about the flow characteristics around single and multiple building configurations has been provided by experiments. However, full scale experiments may become relatively expensive and time consuming. Therefore, scaling of the model and investigation of individual physical parameters is essential most of the times. During the last decades, Computational Fluid Dynamics (hereafter CFD) has developed rapidly as a new analysis tool in many engineering applications, attempting to overcome the experimental drawbacks. Nonetheless, CFD has to face its own challenges. Higher numerical accuracy without increasing the requirements in CPU time is one of them.

In this chapter, the description of environmental flows in urban areas will be given, followed by a brief description of the basic ideas of the turbulence. Moving from single isolated elements to arrays of roughness elements (a more realistic representation of urban areas), the flow structure will be discussed based on published experimental results. In addition, a review of state of the art numerical methods for simulating turbulence in wind engineering will be included. Finally, the chapter will close with an outline of the aims and objectives of the thesis.

1.1 Atmospheric Flows

In this section, the features of atmospheric flows will be discussed. Specifically, the definition and concepts of the Atmospheric Boundary Layer will be given, followed by a description of the flow mechanisms observed in building aerodynamics.

1.1.1 Urban Aerodynamics

One of the most important environmental factors with a great impact on people's daily activities is wind. Wind is the consequence of the air moving from areas of higher to lower pressure due to the pressure gradient force. As soon as the air sets into motion, the Coriolis force occurs as a result of the Earth's rotation. As the air moves from high to low pressure its speed increases, so does its Coriolis deflection until the Coriolis and pressure gradient force are in geostrophic equilibrium. In that ideal situation the air flows along the isobars. However, due to the friction near the Earth's surface, this equilibrium breaks and the air moves slightly across the isobars.

The lowest part of the atmosphere directly affected by the Earth's surface is called Atmospheric Boundary Layer (hereafter ABL). The ABL extends from ground level to *Gradient Height*, which is considered as the minimum height at which the wind speed is equal to the *Wind Gradient speed*. Above this point the wind velocity remains constant. The actual thickness of the ABL can vary from hundreds to a few thousands of meters.

Two regions can be identified within the ABL depending on the effects of surface friction. The *outer* and the *inner* region. In the outer region, also known as *Ekman layer*, the effects of surface friction are negligible and the wind is nearly undisturbed. In the inner region, air circulates closer to the Earth's surface giving rise to frictional forces which cause sudden changes in wind speed and direction. Thus turbulence is generated. Significant exchange of momentum, heat and mass between the atmosphere and the surface takes place in the ABL due to the presence of turbulence [4]. These phenomena appear more intense as the roughness of Earth's surface is increased because of mankind activities such as growth of urbanisation.

The inner region can be divided further: the urban canopy layer which is directly affected by the presence of the roughness elements, the roughness sublayer still adjusting to the effects of the urban surface and finally the inertial sublayer that has already adapted and can be described with standard Atmospheric Boundary Layer formulas. A schematic representation of the inner region is given in Figure 1.1.

Three types of flow can be identified in the ABL, mean wind, waves and turbulence. Those types exist either on their own or in combination with one or both of the remaining types. Mean wind corresponds to the streamwise velocity component and its magnitude ranges between 2 and 10 m/s in the outer region, whereas its minimum value (zero) is reached on the surface. The other two velocity components are considered generally negligible.

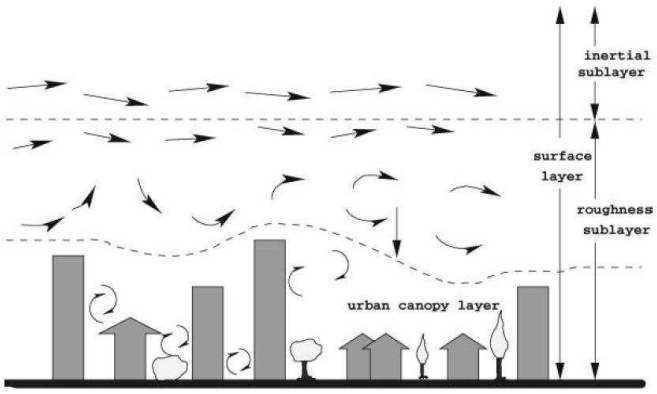

Figure 1.1: Schematic representation of flow over an urban area [9] .

When the suitability of a building structure and its environment are under investigation, a mathematical expression of the wind profile in the vicinity of the ground and over rough obstacles is required. Therefore, measurements of the boundary layer are essential in order to identify consistent and repeatable parameters that characterise the flow. Once the parameters are found, they can be combined into empirical relationships to describe the wind profile.

In the boundary layer, important key parameters are friction velocity (u_*) due to surface shear stress, zero plane displacement (d) and surface roughness parameter (z_0). The zero plane displacement (d) expresses the height above ground (in meters) at which the mean wind velocity is zero due to the presence of roughness elements, whereas the surface roughness parameter (z_0) is a measure of the effect of the obstacle's roughness.

By taking the above parameters into account, the wind speed profile can be approximated as a logarithmic profile given by

$$u = \frac{u_*}{k}\left(ln\left(\frac{z-d}{z_0}\right) + \psi(z, z_0, L)\right) , \tag{1.1.1}$$

where k is the Von Karman constant (approximately equal to 0.4), ψ a stability term and L is the Monin-Obukhov length as described in the similarity theory [24].

Due to diurnal heating and cooling of Earth, atmospheric conditions alter between thermally unstable and stable states [55]. More precisely, during the day, temperature changes with height above the Earth's surface leading to buoyancy production. Convective turbulence is then dominant and instabilities arise which are controlled using a stability term as in Equation 1.1.1.

During the night, however, when little heating or cooling occurs at the surface, temperature stays approximately constant with height. Hence, the shear production of turbulent kinetic energy is much larger than the buoyant production. In situations where the mechanical shear influences in a greater extent the turbulence production and buoyancy remains negligible, atmosphere tends to neutral conditions [3]. Under neutral conditions the stability term drops out and Equation 1.1.1 becomes

$$u = \frac{u_*}{k} ln\left(\frac{z-d}{z_0}\right) . \tag{1.1.2}$$

This thesis will only be focusing in flows under neutral conditions.

Parameters z_0 and d can be determined using several methods. Land-use methods provide tables with values of z_0 corresponding to different types of land. The land-use categories are widely defined in order to cover as many land types as possible. Therefore, there are times where the suggested categories do not take into account urban/industrial areas as in the work of Stull [75]. The relation of z_0 with five urban areas is detailed in the study of Davenport et al. [15] (see Table 1.1). However, it is noted that further analysis is required in order to determine the zero plane displacement (d). In Grimmond and Oke [26], twelve land use types are proposed based on extensive wind velocity profile measurements in many urban areas. According to their conclusions, d ranges from 2 to 5 m in residential and industrial sites, whereas z_0 varies between 0.2 and 1.3 m.

Category	z_0	Description of urban/industrial areas
Roughly open	0.1 m	Moderately open country with occasional obstacles such as low height buildings at relative separations of at least twenty obstacles heights.
Rough	0.25 m	Scattered buildings and/or industrial obstacles at relative separations of eight to twelve obstacle heights.
Very rough	0.5 m	Area moderately covered by low building and/or industrial tanks at relative separations of three to seven obstacle heights.
Skimming	1.0 m	Densely built-up area without much obstacle height variation.
Chaotic	2.0 m	City centers with mixture of low- and high-rise buildings.

Table 1.1: Summary of the surface roughness length (z_0) based on the work of Davenport et al. [15]. The table has been cited originally in the work of Britter and Hanna [9].

A more precise method of estimating z_0 and d is through the calculation of the λ_f (the non-dimensional frontal area) and λ_p (the non-dimensional plan area) parameters using information regarding the size and spacing of buildings. The λ parameters are calculated as

$$\lambda_f = \frac{A_f}{A_T},\ \lambda_p = \frac{A_p}{A_T} , \tag{1.1.3}$$

where A_p is the total building plan view, A_f is the total building frontal area and A_T is

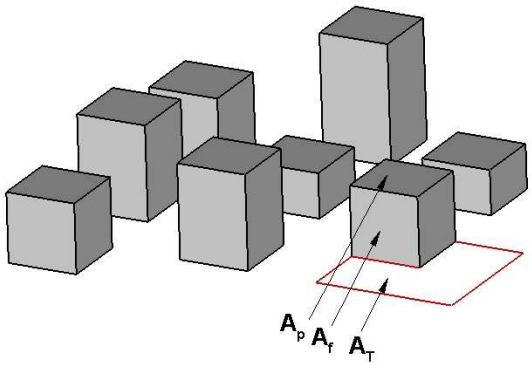

Figure 1.2: Areas of interest in determination of the λ parameters.

the building lot area as shown in Figure 1.2. An evaluation of many techniques using the λ parameters was performed by Grimmond and Oke [26]. They found three types of flows within urban areas: for small values of λ_f, the buildings act in isolation; for larger values of λ_f the wakes of the buildings interfere with each other while for much larger values of λ_f, the skimming flow over the buildings has limited access to the empty areas between the buildings.

Based on field and laboratory measurements of λ_f and λ_p parameters, Britter and Hanna [9] proposed the set of mathematical formulas for z_0 and d as given below

$$\frac{z_0}{H_r} = \begin{cases} \lambda_f & \text{for} \quad \lambda_f < 0.15 \\ 0.15 & \text{for} \quad \lambda_f > 0.15 \end{cases} \tag{1.1.4}$$

$$\frac{d}{H_r} = \begin{cases} 3\lambda_f & \text{for} \quad \lambda_f < 0.05 \\ 0.15 + 5.5(\lambda_f - 0.05) & \text{for} \quad 0.05 < \lambda_f < 0.15 \\ 0.7 + 0.35(\lambda_f - 0.15) & \text{for} \quad 0.15 < \lambda_f < 1.0\ , \end{cases} \tag{1.1.5}$$

where H_r represents the mean building height.

All the above discussion was made on the basis that there was a possible way to estimate the key parameters in order to obtain the logarithmic wind profile. Nonetheless, in cases where it is not possible to define z_0 and d the wind profile is approximated with the power law as follows

$$\frac{u}{u_r} = \left(\frac{z}{z_r}\right)^a \ . \tag{1.1.6}$$

According to Equation 1.1.6, the wind speed u at a height z can be expressed through a known reference velocity u_r at a a reference height z_r. When the conditions are neutral, the value of a is approximately 1/7.

1.1.2 Building Aerodynamics

As mentioned before, when rough elements such as buildings are placed in the ABL, they submerge in an already turbulent and three dimensional atmosphere. Hence, the interaction with the airflow results in a modification of the existing turbulent structure and transfer procedure [67]. Proper understanding of the flow mechanisms in urban areas is vital for preserving pedestrian safety and comfort. Therefore, the features of three dimensional flows around buildings will be discussed. A review of experimental studies, concerned with both the fundamental case of flow around an individual obstacle and the more complex flow fields around multiple building structure is presented.

Major contribution in the field of building aerodynamics has been made by experimental studies whose main aim was to represent the fundamental physics in the most accurate way possible. Most of the times, experiments were conducted in environmental wind tunnels using scale models. However, a few full scale experiments have been reported in the literature. Parameters affecting the flow pattern such as building geometry, wind speed and direction, dependency on Reynolds number, scaling of the model and the extent of boundary layers, were the main areas of interest.

The most comprehensive experimental study that can be found in the literature, describing in detail the aerodynamics around an isolated cube is the one performed by Martinuzzi and Tropea [53]. A typical flow field around a cuboid obstacle is given in Figure 1.3. According to Martinuzzi and Tropea [53], when air reaches the solid

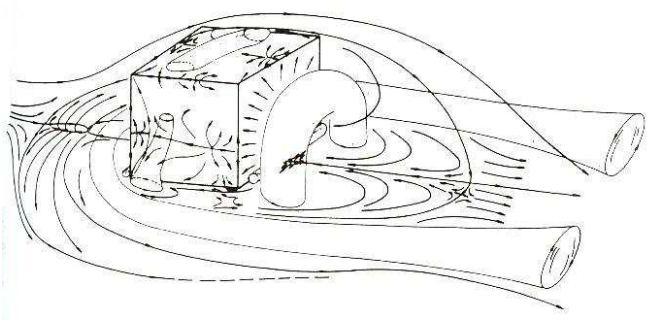

Figure 1.3: Schematic representation of the flow field around a cube [53] .

boundaries (walls) of the cube, a rapid change in its direction occurs leading to the presence of vortices (recirculation areas) in front of the cube close to ground level, after the upstream leading edge of the roof and in the wake. Due to the redirected flow around the sides of the cubes a system of vortices is created. A horseshoe vortex and side vortices are formulated, whereas an arc vortex appears in the lee of the cube. Separation and reattachment of the flow are observed at the sharp leading edge of the roof of the cube. From the above, it can be noted that just a single snapshot of the field pattern around a simplified geometry such as a cube reveals the complexity and unsteadiness of the flow.

Very limited early studies were reported in the literature dealing with the wake behind

the cube due to its highly turbulent nature. However, Castro and Robins [10] conducted an experiment focusing mainly on this specific region as an attempt to understand the way it is affected by the upstream turbulence and shear. In particular, flow around a single cube placed either normal to the flow direction or at an angle of 45^0 was investigated. An indication for the total flow was extracted using measurements of surface pressure on the front and back face of the cube as well as mean and fluctuating velocities in the wake. A visualisation of the flow structure in the wake showed that when the flow was normal to the front face of the cube, the addition of upstream turbulence and shear resulted into reduced cavity zone. Regarding the second case where the cube was placed at an angle of 45^0, the wake was dominated by strong vortices very similar to the ones observed in delta wings.

An oil visualisation technique for highly turbulent recirculation flows around cuboids with various shapes was conducted by Hunt et al. [38]. Separation and reattachment locations were shown by identifying the nodal and saddle points. The mean flow patterns were sketched using mean flow streamlines and surface stress lines, leading to the conclusion that in flows around surface mounted obstacles closed surface streamlines did not exist. This conclusion contradicts an earlier study of Halitsky [32] that supported the exact opposite assumption.

A comprehensive study of flow around a three dimensional rectangular prism was conducted by Schofield [68]. Although the geometry under investigation was different, the conclusions drawn were similar to the case of single cube. Two main regions of interest were identified around the obstacle: the perturbation and recovery region. Here, three major features of the flow were outlined in conjunction with previous studies on the same subject. Firstly, it was stated that formulation of closed bubbles did not exist on the wall around the three dimensional obstacle; a statement that confirmed the conclusions drawn by Hunt et al. [38]. Secondly, four vortices were traced near the frontal face of the prism despite the fact that it was stated that it was often difficult to visualise the vortices by using mean surface streamlines. The third feature involved the reattachment of the mean flow at the top of the obstacle at shorter streamwise lengths than for flows around two dimensional obstacles.

A very recent wind tunnel experiment regarding the flow around a medium rise rectangular building was conducted by Bartoli and Ricciardelli [7]. The aim of the study was to investigate the features of pressure fluctuations on the leeward and side faces of buildings and to assess the accuracy of calculating the wind load using the quasi-steady method. A number of wind tunnel tests were performed simulating flows around two scale models, two flow regimes (open land and urban exposure) and two directions of incoming flow (perpendicular to the wide and narrow faces of the building respectively). Based on the results, it was concluded that the propagation of pressure fluctuations in the wake is related to the length of the wake and it lasts longer than the time it takes for a particle to travel along the depth of the building with the flow velocity. Finally, regarding the evaluation of the quasi-steady approach, it was found that it was indeed a valid method for estimating the pressure distributions on the faces of a building.

A more realistic representation of urban areas is given by experimental studies investigating flows within arrays of rough elements resembling buildings. The studies were focusing on examining the effects of the building height, building configuration and spatial density of the buildings, as well as the direction of the wind. A number of the above parameters was investigated by Stathopoulos and Storms [72] and Stathopoulos and Wu [73]. More precisely, results were obtained from a boundary layer wind tunnel experiment simulating flows around two rectangular based buildings [72]. The study was focusing on the ramifications of a number of parameters such as building height, passage width (distance between the buildings) and wind directions (imposed along the centreline of the building passage). Comparisons in terms of amplification and reduction ratios of velocities and turbulent intensities, with and without the presence of the buildings, led to the following conclusions. When the passage width remained constant and the buildings were of equal heights, it was found that for a wind direction ranging between 0 and 30 degrees, the difference of velocity amplification ratios was very small and the highest velocity was noticed at 30 degrees. However, a reduction of velocity occurred when the wind direction belonged in the range from 60 to 90 degrees. For the latter range, the turbulent intensities were drastically increased. By choosing to keep the wind azimuth constant and modify the height and passage width, it was found that any increase of the passage width resulted in a decrease of the velocity amplification, where buildings of different heights are affected the most.

A similar study can be found in Stathopoulos and Wu [73]. The wind tunnel experiment was examining the flow conditions in a street block consisting of eight uniform low rise buildings and one high rise placed in the center of the group. The effects of height difference were investigated by modifying the height of the tall building. Firstly, it was deduced that, when buildings were uniformly distributed, the wind speed could be defined as a function of the blockage ratio R_B. The blockage ratio is given by

$$R_B = \frac{A_S}{A_F} \, , A_S = Wh \, , A_F = (W + L_A)^2 \, . \tag{1.1.7}$$

A schematic representation of the areas of interest is given in Figure 1.4.

Therefore, any increase of R_B (resulting from increased building height or decreased passage width) would lead to a reduction in velocity magnitude. Secondly, the wind speed variation within the given building configuration was related to the height difference between the high and low rise buildings, the passage width and the blockage ratio by using linear regression analysis. Based on the above relation, it was stated that the wind reached its maximum value at the leading edge of the tall building. An observation like that could be explained by stating that with increasing height difference, the air flow of the upper levels is drifting sideways around the building rather than moving vertically to the street level.

An early study is the one found in Murakami et al. [60]. The main purpose of the study was to specify the extent to which a high rise building affects the flow pattern when the surrounding area consists of lower height blocks. Very important conclusions were drawn using field observations before and after the actual construction of a high rise

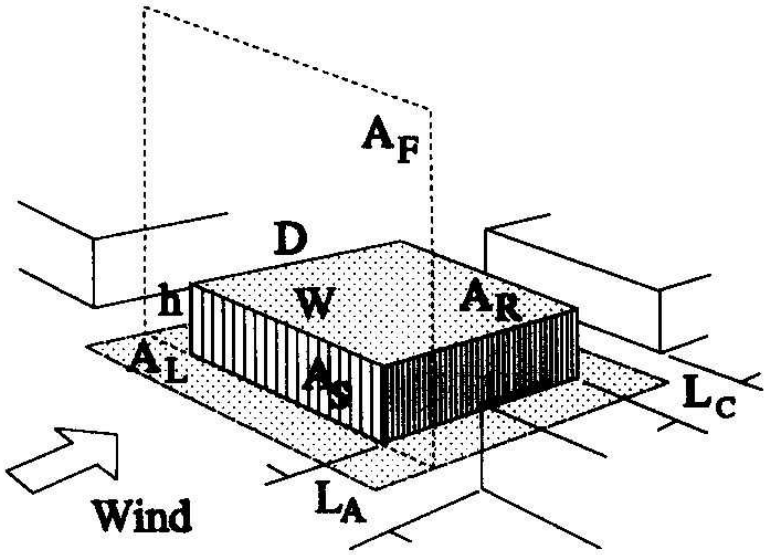

Figure 1.4: Areas of interest in determination of the R_B [73] .

building in the city of Tokyo; as well as by conducting wind tunnel experiments investigating the connection between buildings shapes, building heights and wind conditions. According to field measurements, the existence of the high rise building changed the direction of the wind dramatically. Specifically, at a location where the most frequent wind directions were North-West and South originally, the presence of the building redirected the wind to North-West and East. The amplification factor of wind speed almost got double in some cases, whereas the gust factor (the ratio of gust speed to mean wind speed) was reduced. Important information was gathered from the experimental study by using a surface film of pigmented oil for flow visualisation at the tall building, at first on its own and then with the surrounding building. The presence of the surrounding buildings altered the flow pattern significantly with the adverse flow at the upstream face of the building appearing more intense due to the interaction of the circulation areas generated from the high building and the surrounding ones. Regarding the flow over the top of the building, it appeared reinforced with strong recirculation at the back of the building resulting in a strong upward reverse flow at ground level. An approximately 2.5 times higher amplification factor was observed when the surrounding buildings were present when comparing with only one building. By examining the effects of the height of the building, it was noticed that any increase in the height of the building with the building area being constant led to an increase in amplification factor and velocity magnitude. However, the rate of increase started reducing when the height of the building reached 6 times the height of the surrounding ones. Furthermore, a very strong wind area was developed at the front of the building and the sideways when the height of the tall building was 2 to 3 times the height of the small ones.

Meinders and Hanjalic [54] also performed a wind tunnel experiment investigating the flow around a cubical matrix consisting of 25x10 elements along the streamwise and

spanwise direction, respectively. The experimental study provides very useful information about the flow characteristics within the array. Specifically, it was found that the flow appeared to be highly turbulent in the immediate vicinity of the buildings, whereas above them and in the passage between them the flow was almost undistorted. Flow separation took place as soon as the flow reached the top leading edge by creating a recirculation bubble whereas additional vortices were formed at the side edges. A horseshoe vortex, detected at the upstream face of the cube, was diverted towards the wake where it started weakening due to its interaction with the vortices of the neighbour cubes. The wake of the cube was dominated by the existence of an arch vortex. The presence of vortex shedding in the wake of the building caused high velocity gradients which were believed to be resulting in high turbulent kinetic energy.

One of the latest wind tunnel experiment that provides a detailed description of flow around arrays of roughness elements is the one performed by Cheng and Castro [12]. The high Reynolds number flow around groups of buildings of different configuration (staggered or aligned) and of different heights (cases with uniform heights or random heights) was measured. The existence of three dimensional turbulent flow within the building envelope has been confirmed by the results. From the results, it was concluded that the depth of the roughness sublayer is a function of the building height and that the staggered building alignment produces a greater drag than the aligned configuration for the same building array. The spatially averaged mean velocity profile within both sublayers, roughness and inertial, was fitted in a log law profile at a given friction velocity. Finally, it was found that the upper limits of the inertial sublayer for the cases of random and uniform building heights were very similar with the only difference being the thicker roughness sublayer in case of the random height building array. The work of Cheng and Castro [12] was discussed further in Castro et al. [11].

A wind tunnel study aiming in revealing the relationship between the building density and the mean wind speed in residential areas was performed by Kubota et al. [47]. Two measures of building density were used in the present study, the gross building coverage ratio and the gross floor area of the neighborhood. Twenty two test cases (under the same wind conditions) were performed each one corresponding to a different Japanese residential area. The results revealed the strong connection between the gross building coverage ratio and wind speed. Any increase in the coverage ratio will consequently lead to a decrease of the mean velocity magnitude. It was also found that for areas with the same percentage of coverage, favorable or unfavorable pedestrian conditions were created depending on current climatic conditions.

The flow feature of lateral channeling within two arrays of aligned cubes was discovered during the water channel experiment conducted by Princevac et al. [63]. The definition of lateral channeling was given as followed: As flow enters the three dimensional array, it gets redirected at the sideways after the first row of building elements. If the second row of elements is considered as ”one block” with gaps, then this block will still produce a longitudinal resistance leading to outflow conditions for the first row; thus lateral channeling. Based on a detailed investigation for a range of Reynolds numbers, it was concluded that the specific flow feature was visible in all different flow

conditions and that it was the result of streamlines being deflected by the array and low pressures regions at the sides of the array.

Boundary layer wind tunnel experiments investigating the effect of urban design in flows within city street models were performed by Hang et al. [33]. Two forms of cities were assessed; a round and a rectangular city with one or more intersecting streets. From the results obtained it was concluded that the structure of the city model had a great influence on the generated flow pattern around and within the model. More precisely, for a single street city model, it was found that the round city model produced smaller separation flow and fewer vertical structures than the square city model. The flow pattern became more complex when two intersecting streets (a primary and a secondary) were included. The most important flow features seemed to be present in the secondary street and their characteristics depended on the city model. On one hand, helical inflow was formed in the square city model whereas on the other hand, a helical outflow was generated in the round city model. Finally, it was shown that the wind within a round city model with more than two intersecting streets was much stronger than in the similar structure of a square city model.

By summing up all the above observations, it can be stated that building aerodynamics are very complex with highly turbulent features and with a flow field being affected by any change of the outdoor environment regarding the shape, size and orientation of the building elements. Important information has been gathered from the experimental studies conducted over the decades. However, the simplified geometries and the requirements for model scaling due to limited physical space will never allow full scale investigation of the flow physics neither around very complex building structures nor in real modern urban areas such as the ones shown in Figure 1.5.

(a) Dubai Towers (construction on hold)

(b) Burj al Arab, Dubai development

(c) Tokyo city

Figure 1.5: Modern Building Construction [1].

1.2 Characteristics of Turbulence

In the chapter so far, atmospheric flows were always referred to as turbulent flows. Before continuing further, it is important to provide a description of this complex phenomenon called turbulence. In the section that follows, the characteristics of turbulence will be outlined as part of completing the understanding of the physics behind it.

1.2.1 The History of Turbulence

Turbulence manifests itself in nature in various ways: smoke coming out of a chimney, waterfalls and strong wind. In 1937, Taylor and Von Karman characterised turbulence as *an irregular motion which in general makes its appearance in fluids, gaseous or liquid, when they flow past solid surfaces or even when the neighboring streams of the same fluid flow past or over one another* [85]. The distorted fluid motion in whirlpools seemed to fascinate Leonardo da Vinci who was the first one to conceive the idea of turbulence and imprint it into his sketches. However, the first representation of turbulence using the physical properties of a fluid is attributed to Osborne Reynolds [50]. Reynolds used a flow visualization technique in order to investigate the conditions under which a flow is laminar or turbulent. His investigation resulted in the establishment of a parameter that indicates the ratio of inertial to viscous forces and distinguishes the two states of a flow. The parameter was named after him and is the well known *Reynolds number*.

During the period between the two World Wars, important advances in the field of turbulence were made by von Karman, Prandtl and Taylor. The physical behaviour of various sized eddies composing turbulence was described by Richardson [64] in the concept of *energy cascade*. According to *Richardson's hypothesis* energy transfer occurs from the large scales to the smaller, following a multi-stage procedure until energy is dissipated into heat. The smallest scales in turbulence responsible for dissipating energy were determined by Kolmogorov [45]. A more detailed description of the energy transfer procedure and the scales of turbulence will follow.

Despite all these important studies through the centuries, there is no complete definition of turbulence to date. Nevertheless, in typical free shear flows, the three dimensional motion of the fluid can be described as random, chaotic and unsteady with the velocities varying significantly in time and space.

1.2.2 The Scales of Turbulence

Turbulence consists of vortical structures in various scales that coexist. The dynamics of turbulence involved can be described through the *energy cascade* concept as given in Richardson's hypothesis.

Richardson's Hypothesis

According to Richardson's hypothesis, turbulence is composed of vortical structures (also called *eddies*) of different sizes. Eddies with a length comparable to the characteristic length l exhibit a velocity equal to the characteristic velocity *u(l)* and the timescale *t=u(l)/ l*. Thus, the Reynolds number of the large eddies is comparable to the global Reynolds number $Re = u(l)l/\nu$. In high Reynolds numbers, where the viscous effects are negligible and dissipation does not take place, the fluid accumulates kinetic energy in the large scales that has to be transferred to the smaller scales. The shape of the eddies gets distorted and finally they break down into smaller scales. In the same fashion, smaller eddies break down into even smaller ones until the Reynolds number is sufficiently small enough so that the smallest eddies are dissipated into heat. At that point, the multi stage energy transferring procedure following a hierarchy order of eddy scales comes to an end and energy is dissipated into heat due to viscous stresses.

The rate of energy transfer can be calculated as

$$\frac{u^2}{\tau} = \frac{u^3}{l} \tag{1.2.1}$$

where u^2 the energy contained in a large scale and τ is the eddy turnover time $\tau = l/u$ denoting the lifetime of a large eddy.

Kolmogorov's Hypotheses

Kolmogorov's hypotheses answered fundamental questions regarding the scales of turbulent flows and the assessment of energy transfer. In his first hypothesis, Kolmogorov states that large eddies are anisotropic and their geometry is affected by the boundary and mean flow conditions. Due to the energy cascade anisotropy is lost, resulting in locally isotropic small eddies.

Kolmogorov's hypothesis of local isotropy: *At sufficiently high Reynolds number, the small scale turbulent motions are statistically isotropic [62].*

Apart from losing anisotropy, information regarding the geometry of large scales is lost as well. Since the small eddies are not affected by the boundaries, Kolmogorov argued that the small eddies have a universal character for all turbulent flows of a similar Reynolds number. Because of their relatively short lifespan, smaller scales are directly influenced by molecular interactions and have the ability to adapt quickly in order to obtain an equilibrium with the rate of energy transfer from the larger scales. Based on the above characteristics of small eddies, it can be concluded that their universal character depends on two parameters: the kinematic viscosity ν and the heat dissipation rate ϵ.

Kolmogorov's first similarity hypothesis: *In every turbulent flow at sufficiently high Reynolds number, the statistics of the small scale motions have a universal form that is uniquely determined by ν and ϵ [62].*

By using the above, the following definitions of the Kolmogorov length, velocity and time scales can be given

$$\begin{aligned} \eta &\equiv (\nu^3/\epsilon)^{1/4} , \\ u_\eta &\equiv (\nu\epsilon)^{1/4} , \\ \tau_\eta &\equiv (\nu/\epsilon)^{1/2} . \end{aligned}$$

These scales are known as *Kolmogorov scales*. The Reynolds number using the Kolmogorov scales is equal to unity, a fact that shows consistency with Richardson's hypothesis, according to which dissipation occurs for the smallest possible eddies.

The ratios of the Kolmogorov scales over the characteristic scales present in the mean flow, are related to the global Reynolds number and are given by

$$\begin{aligned} \eta/\ell &\equiv Re^{-3/4} , \\ u_\eta/u &\equiv Re^{-1/4} , \\ \tau_\eta/\tau &\equiv Re^{-1/2} . \end{aligned}$$

Since the largest and the smallest scales of turbulence have been defined, that leaves out a range containing scales which are smaller than l but higher than η. In this intermediate range, only energy transfer occurs from the largest to the smallest scales. Thus, the region can be characterised by only one parameter, the heat dissipation rate ϵ.

Kolmogorov's second similarity hypothesis: *In every turbulent flow at sufficiently high Reynolds number, the statistics of scales ranging between l and η have a universal form that is uniquely determined by ϵ, independent of ν [62].*

The length scale of turbulence that belongs to the specific range is called *Taylor's microscale* λ_T. The ratios of λ_T over the global length scale and over Kolmogorov's length scale verifies that λ_T is indeed smaller than l, but higher than η

$$\begin{aligned} \lambda_T/\ell &\equiv Re^{-1/2} , \\ \lambda_T/\eta &\equiv Re^{1/4} . \end{aligned}$$

1.2.3 Energy Spectrum Analysis

The typical distribution of kinetic energy of homogeneous turbulence among eddies of different sizes is given in Figure 1.6. The motion of the different length scales corresponds to a wavenumber *k* and the velocity profile *u(k)* is decomposed into Fourier series. The amount of energy *E(k)* that each length scale contains is then calculated by multiplying the velocity with its complex conjugate.

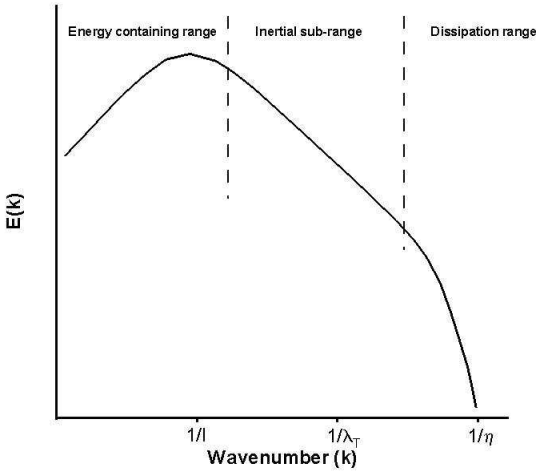

Figure 1.6: Schematic of a typical turbulent kinetic energy spectrum [62].

According to Figure 1.6, the energy spectrum can be divided into three ranges on the basis of the corresponding length scales; the energy containing range, the inertial subrange and the dissipation range.

In the energy containing range, the large scales are anisotropic and their geometry is influenced by the mean flow and the boundary conditions. They are characterised by small wavenumbers. Kinetic energy is piled up at larger scales, up to the point where breakdown of the large scales takes place and energy is transfered to the smaller scales. The parameters that dominate this range are the shear stress and the dissipation rate.

In the inertial subrange, the viscous effects are negligible and kinetic energy is transfered to progressively smaller scales. Kolmogorov's realisation of the energy spectrum within the inertial sublayer is given by

$$E(k) = C\epsilon^{2/3}k^{-5/3} \ ,$$

where C is a universal constant.

Finally, the last range of the energy spectrum is the dissipation range. This region is characterised by the smallest possible scales (high wavenumbers). The viscous effects are present and dissipate energy into heat. The dominant parameters are the kinematic viscosity and the dissipation rate.

1.3 Numerical Models

Experimental studies provide essential information about one of the most complicated flow fields. However, they can be relatively expensive, time consuming and produce

limited data. In order to overcome the experimental drawbacks, CFD has gained popularity as a new analysis tool during the last decades. CFD allows for combinations of solution parameters in one single case without being unaffordable in CPU requirements and without any scaling of the model.

Numerical modelling in the field of building aerodynamics has to face several challenges. Firstly, an accurate representation of the wind profile in an urban area and any effects that the building structures have upon it requires good knowledge of the features of the ABL and mean speed and turbulent data. Often though, it is not possible to extract this information from the available meteorological data. Additionally, modern urban areas involve complex geometries and topologies that result into a challenging domain discretisation.

As mentioned in Section 1.2.2, turbulence consists of eddies appearing in different sizes. Depending on the scales of the vortical structures that are resolved or modelled, there are three main numerical approaches: Direct Numerical Simulation (DNS), Large Eddy Simulation (LES) and Reynolds Averaged Numerical Simulation (RANS). More precisely, all scales are modelled in RANS, whereas the large scales are resolved and the smallest are modelled in LES. Finally, the complete range of scales, even the smallest ones, are captured by the DNS. A fourth approach called Implicit Large Eddy Simulation (ILES) has also been introduced. Although ILES belongs to the family of LES, it is considered simpler and more computational efficient than classical LES. In order to provide the reader with an insight into the advances of each approach, a description of all the available numerical approaches will follow.

Direct Numerical Simulation (DNS)

DNS is considered the most accurate approach to simulate turbulence. The Navier-Stokes equations are solved directly without any additional turbulence model. Thus, DNS is free from any modelling errors. Since all motions are captured, excessive grid refinement is required in order to resolve all scales even the smallest ones including the Kolmogorov microscales. To meet this requirement, the total number of grid points (in one dimension) is proportional to the ratio of characteristic length over Kolmogorov length scale, $l/\eta = Re^{3/4}$. Therefore, for a three dimensional case the number of grid points reaches the value of $Re^{9/4}$. Additionally, the time step is limited by the short lifetime of Kolmogorov microscales which leads to a total number of time steps of order of $Re^{3/4}$.

The cost of DNS is calculated from the product of the total number of grid points and time steps, according to which the total cost is estimated as Re^3. Based on the last remark, it can be said that the computational cost of DNS increases rapidly with an increasing Reynolds number. It becomes clear that DNS is limited to simulate flows on low Reynolds numbers due to its prohibitive computational cost. The restriction is the reason why DNS cannot be used as a design tool for industrial applications, but only as a research tool for understanding the mechanisms of turbulence. In the future, the rapid technological progress might allow computers with sufficient speed

and memory to resolve turbulent flows at high Reynolds numbers.

Very few DNS studies of flows around solid obstacles are reported in the literature. Therefore only three conducted by Hwang and Yang [39], Yakhot et al. [89] and Coceal et al. [14] as validation studies against experimental studies are mentioned here.

A very detailed description of the vortical structure around a single element located in a channel was provided in the work of Hwang and Yang [39]. The changes in flow structure at the front and the rear of the building were discussed in cases where the Reynolds number was ranging from 5 to 3500. Specifically, it was found that the horseshoe vortex became visible only when the Reynolds number was increased above 300. Any further increase in Reynolds number led to an increase in the number of vortices appearing in pairs. An equation defining the relationship between the Reynolds number and the distance between the saddle point and the upstream face of the building was defined as well. Finally, it was stated that despite the fact that the windward region was steady, the leeward region was turbulent even at low Re.

A DNS study of flows around a cube in a fully developed channel flow was performed by Yakhot et al. [89] as part of investigating the applicability of the immersed boundary method to turbulent flows. The study involved flows at Reynolds number of 5610. From the results, it was noticed that the flow reattached at the top of the cube and that the recirculation region in the wake of the cube appeared shorter than the one described in the experimental study of flows at Reynolds numbers of 40000 by Martinuzzi and Tropea [53]. However, comparisons with existing experimental studies were found to be in good agreement with the DNS data when mean and turbulent statistics were used.

Finally, a recent DNS study by Coceal et al. [14] is reported in the literature involving flows within cubic obstacles representing urbanlike areas. The results revealed that the flow features between aligned and staggered arrays were completely different, indicating the high dependency of the vortical structure upon the building configuration. Comparisons with experimental data in terms of mean flow statistics showed very good agreement. The importance of the specific DNS study lies in the fact that through the detailed resolution of the flow, essential information was gathered for the characteristics of turbulence around roughness elements.

Reynolds Averaged Navier Stokes (RANS)

The most popular approach for engineering applications is the Reynolds Averaged Navier Stokes (hereafter RANS). RANS was named after Osborne Reynolds, according to whom the instantaneous flow properties can be decomposed into an averaged and a fluctuating part. Consequently, the instantaneous variables in Navier Stokes equations are replaced by the sum of these two components. However, this transformation results in additional unknowns, the so-called Reynolds stresses. For the sake of system closure, a turbulence model has to be introduced, most of the time in the form of additional PDEs. It becomes clear, due to the complexity of each turbulent flow, that it is unlikely that they can be represented by one single model.

A review of the most representative studies using the Standard k-ϵ RANS model will be discussed here. The robustness and reduced requirements in CPU time of the RANS model was presented in the work of Ehrhard and Moussiopoulos [22]. However, it overpredicts the turbulent kinetic energy near stagnation points and specifically at the leeward face of a single cube. Studies testing the ability of RANS in predicting the complex flow around cubical models for moderate and high Reynolds numbers are reported in Tutar and Oguz [81]. In Tutar and Oguz [81], the performance of two RANS models, the Standard and the RNG k-ϵ, was investigated for three test cases involving flows around one, two and nine building structures. The results showed that the accurate prediction of the basic flow features depended on the choice of turbulence model and grid resolution. It was found that RNG model produced data that was in better agreement with available experimental data when compared with the Standard k-ϵ model, which failed in predicting the anisotropy of turbulence. Regarding the channeling effect, it was observed that an increase of the width of the passage between buildings resulted in an increase of the length of the recirculation region. Therefore, the strength of the vortical structures and the velocity magnitude within the passage were reduced.

In Murakami [58, 59], it is stated that RANS appears to be inaccurate in the near wall region. Specifically, it is noted that it fails to accurately predict the complex flow pattern around a surface mounted obstacle representing a building. The reason lies in the oveprediction of kinetic energy near the stagnation points due to inability to accurately calculate the adverse pressure gradient at the frontal face of a cube.

Large Eddy Simulation (LES)

Although great advances have been made in the field of numerical modelling, difficulties still remain due to the high complexity of the flow field. With the rapid increase in computer technology, Large Eddy Simulation (hereafter LES) has been developed in order to bridge the gap of computational expense between DNS and RANS. LES, derived from the pioneering work of Smagorinsky [71], can be used for simulating three dimensional time dependent problems at higher Reynolds number. LES exhibits superior performance in comparison with RANS without requiring the high refined computational grids of DNS.

According to Kolmogorov's theory, large eddies depend on the mean flow conditions whereas the small eddies have an universal character for all types of turbulence. Hence, large eddies can be calculated explicitly while the small ones (also referred as sub grid scales) are modelled, using most of the times, a sub-grid scale model (hereafter SGS). In classical LES, the separation of the large from the small scales is obtained by using filters. Filters associated with both spatial and temporal cutoff scales can be employed. However, the spatial filters, written as $G(\mathbf{x}, \Delta)$ where Δ is the filter width, are the most commonly applied ones in the context of LES.

Assume the incompressible Euler set of equations as given below

$$\nabla \cdot \mathbf{u} = 0 \,, \tag{1.3.1}$$

$$\frac{\partial \mathbf{u}}{\partial t} + \nabla \cdot (\mathbf{u} \otimes \mathbf{u}) + \frac{1}{\rho}\nabla p = 0 \tag{1.3.2}$$

where $\mathbf{u}$, t, ρ and p are the velocity vector, time, density and pressure, respectively. Once the filtering operation has been performed, variable f, which stands for any of the variables appearing in the equations above, is decomposed into $f = \overline{f} + f'$ where $\overline{f} = G(\mathbf{x}, \Delta) \cdot f$ is the resolved and f' is the sub grid part. Therefore, the filtered form of Equation 1.3.1 and 1.3.2 is

$$\nabla \cdot \overline{\mathbf{u}} = 0 \,, \tag{1.3.3}$$

$$\frac{\partial \overline{\mathbf{u}}}{\partial t} + \nabla \cdot (\overline{\mathbf{u}} \otimes \overline{\mathbf{u}}) + \frac{1}{\rho}\nabla \overline{p} = -\nabla \cdot \tau^{sgs} - \mathbf{m}; \tag{1.3.4}$$

where τ^{sgs} is the subgrid scale stress tensor and $\mathbf{m}$ is the commutation error term.

Commutation errors occur in near wall regions and on stretched or non uniform grids where the differential operators do not commute with the filtering procedure, $\frac{\overline{\partial f}}{\partial x} \neq \frac{\partial \overline{f}}{\partial x}$. It is possible that commutations errors may not arise in cases where uniform grids are used and the Δ is constant [18]. Truncation errors are also originated from the discretisation of the above equations. Generally, the effect on the solution of this type of errors is assumed negligible and it is omitted. However, this assumption is not always valid [25].

The subgrid stress tensor, τ^{sgs}, in Equation 1.3.4 is defined as

$$\tau^{sgs} = \overline{\mathbf{u} \otimes \mathbf{u}} - \overline{\mathbf{u}} \otimes \overline{\mathbf{u}}. \tag{1.3.5}$$

From the filtering procedure u is equal to $\overline{u} + u'$, thus Equation 1.3.5 can be written as

$$\tau^{sgs} = \left(\overline{\overline{\mathbf{u}} \otimes \overline{\mathbf{u}}} - \overline{\mathbf{u}} \otimes \overline{\mathbf{u}}\right) + \left(\overline{\overline{\mathbf{u}} \otimes \mathbf{u}'} + \overline{\mathbf{u}' \otimes \overline{\mathbf{u}}}\right) + \left(\overline{\mathbf{u}' \otimes \mathbf{u}'}\right), \tag{1.3.6}$$

where $\mathbf{L}_{ij} = (\overline{\overline{\mathbf{u}} \otimes \overline{\mathbf{u}}} - \overline{\mathbf{u}} \otimes \overline{\mathbf{u}})$ is the Leonard stresses (representing the interactions between the resolved stresses), $\mathbf{C}_{ij} = \overline{\overline{\mathbf{u}} \otimes \mathbf{u}'} + \overline{\mathbf{u}' \otimes \overline{\mathbf{u}}}$ is the Cross stress tensor (corresponding to the interactions between the unresolved and the resolved stresses) and finally $\mathbf{R}_{ij} = \overline{\mathbf{u}' \otimes \mathbf{u}'}$ is the Reynolds stresses (standing for the interactions between the unsolved stresses). Despite the above decomposition, it is preferred that the τ^{sgs} is directly modelled as a single unit [18].

Consider now the following equation, which corresponds to the modified form of N-S in respect to only one dimension,

$$U_t + \nabla \cdot E(U) = \nabla \cdot \tau^{sgs}(U) \tag{1.3.7}$$

where **U** stands for the array of the dependent variables and **E** is the non-linear inviscid flux vector which will be discussed further in Chapter 2.

For Equation 1.3.7, the most widely applied sudgrid stress model in the context of LES is the Smagorinsky model [71] and it is given by Equation 1.3.8

$$\tau^{sgs} = -C\Delta^2|\nabla U|\nabla U \ , \tag{1.3.8}$$

where C is a constant and Δ is the width of the cell. In order to derive the formulation of the change of global kinetic energy [18], τ^{sgs} in Equation 1.3.9 is substituted with the one given in Equation 1.3.8

$$\bar{\mathcal{E}} = \int \frac{\partial \mathbf{U}}{\partial x} \tau^{sgs} \, dx' \ . \tag{1.3.9}$$

Consequently, Equation 1.3.10 is obtained according to which the global kinetic energy is always decreasing in time. Thus the Smagorinsky model is strictly dissipative.

$$\bar{\mathcal{E}} = -C\Delta^2 \int \left| \frac{\partial \mathbf{U}}{\partial x} \right|^3 \, dx' \leq 0 \ . \tag{1.3.10}$$

Apart from its dissipative characteristics, the Smagorinsky model does not take into account any interactions between the largest unresolved scales and the smallest resolved scales. In order to overcome these drawbacks, the scale similarity models were developed. Specifically, Bardina et al. [6] introduced a model in which the subgrid scale tensor represents the error difference between procedures using two different filter sizes (2Δ and 4Δ). The subgrid stress is then defined as

$$\tau^{sgs} = -C\Delta^2 \nabla U \nabla U \tag{1.3.11}$$

where as in Equation 1.3.8, C is a constant and Δ is the width of the cell.

Following the same procedure as above and substituting Equation 1.3.11 into Equation 1.3.9, the change of kinetic energy now becomes

$$\bar{\mathcal{E}} = -C\Delta^2 \int \left(\frac{\partial \mathbf{U}}{\partial x} \right)^3 \, dx'. \tag{1.3.12}$$

Based on Equation 1.3.12, it is concluded that the scale similarity models are hardly dissipative.

Finally, due their non dissipative character and the fact that they encounter for outscatter and backscatter, the scale similarity models are most of the times used in conjuction with the Smagorinsky model forming the mixed subgrid scale models [18].

The popularity of the LES method is evident in the literature. The collection of conducted studies include flows around single and multiple wall mounted obstacles. The first application of LES to meteorological flows was reported in the work of Deardorff [16]. Since then, many researchers used LES in their studies either for validation against existing experimental data or as a reference model against RANS models. Important reviews of LES and comparison studies showing a very good agreement with experiments can be found in Rodi et al. [66] and Rodi [65].

Validation studies against existing experimental data are reported in the literature, with some of them being conducted by Shah and Ferziger [70], Sedighi and Farhadi [69], Krajnovic and Davidson [46] and He and Song [36]. More precisely, in Shah and Ferziger [70], the flow pattern around a surface mounted cube was calculated at high Reynolds number. It was concluded that, despite some differences regarding the turbulence kinetic energy profiles, the numerical solution seemed to present a reasonable agreement with the experiment conducted by Martinuzzi and Tropea [53]. A similar study investigating the effect of Reynolds number was performed by Sedighi and Farhadi [69]. The results revealed the presence of more than one horseshoe vortex at low Reynolds number, whereas with increasing Reynolds number the vortices merge, forming only one as shown in the study of Martinuzzi and Tropea [53]. It was found that the higher the Reynolds number, the shorter the length of reattachment and the higher the values of turbulent intensities and Reynolds stresses at the core of the vortices and the sideways of the cube.

A range of different visualisation techniques were used by Krajnovic and Davidson [46] in order to illustrate the flow field around an individual cube. Regardless of the visualisation method, the main features of the flow as described in Martinuzzi and Tropea [53] were captured, an outcome that verified LES applicability to complex flows. Finally, in the work of He and Song [36], the performance of LES was tested for three practical test cases involving different building geometries and wind directions.

Flows around arrays of buildings have been simulated with LES as well. A recent validation study of Xie and Castro [87] and Xie and Castro [86] produced a comparison between RANS and LES model. The performance of each model in predicting the flow in arrays of buildings, consisting of elements with uniform or non uniform height, in staggered or aligned configurations, was investigated. The RANS approach was found to be unable to predict the flow in the canopies between the buildings, whereas LES was more accurate in estimating the unsteadiness of the region. Therefore, RANS was deemed as inappropriate for simulating these specific kind of flows. Analogous studies verifying the applicability of LES in building aerodynamics are described in the investigations of Stoesser et al. [74], Kanda et al. [42] and Cheng et al. [13].

Stoesser et al. [74] examined the applicability of LES to flows within clusters of cubes at relatively low Reynolds number. More precisely, aligned and staggered cubical arrays were placed in channels of small and large depth. Good agreement with experimental and DNS data in terms of mean and fluctuating quantities were obtained and an accurate representation of the flow structure was achieved. Kanda et al. [42] investigated the channeling effects between the aligned buildings. Turbulent organised

structures (TOS) and turbulent statistics were considered for predicting the differences between urban canopy and vegetation flows. Simulations showed the resemblance of urban canopy flows to flows within the surface layer. Flows around vegetation were found analogous to those in mixing layers. Numerical data was in good agreement with the experimental data especially for the regions above the canopy. However, the velocity magnitude was underestimated within the building canopy and the velocity profile depends significantly on the area density between the buildings. Finally, a comparison between the Standard $k-\epsilon$ RANS model and LES involving flows around a matrix of cubes at high Reynolds numbers can be found in Cheng et al. [13]. LES was able to predict all the important flow features and quantitative data was in good agreement with experimental data. RANS results, however, showed an overestimation of the length of the recirculation zones in the wake of the cube. Consequently, the mean streamwise velocity profiles were underestimated upstream at the frontal part. Although LES seemed to be the most appropriate approach for simulating the complexity of the flows around bluff bodies it was found approximately 100 times more expensive in CPU time than the Standard $k-\epsilon$ RANS model.

So far, it has been proven that LES is reliable in simulating many engineering applications. However, drawbacks exist associated with the approach's potential in the field of wall bounded flows. With the scales becoming smaller and smaller in the near wall region, two options are available: either to modify the SGS model or to use wall models. However, both options could increase the complexity of the SGS model rapidly and become unaffordable in high Reynolds numbers [27].

Implicit Large Eddy Simulation (ILES)

Based on the idea of Von Neumann and Richtmyer [84] for shock capturing, back in the 50's, a trend of abandoning the conventional LES and use implicit instead of explicit SGS models was first introduced by Boris et al. [8]. The new method was named Implicit Large Eddy Simulation (hereafter ILES). The ILES approach comprised high resolution methods for solving the non linear inviscid part of the equations and finite volume differencing. In Drikakis and Rider [18], it was shown that the specific combination naturally generated a truncation error that not only appeared in the same divergence form as the sub grid scale stress tensor in classical LES but also had similar effects on the solution. In this section the similarities and differences between LES and ILES will be discussed as well as presenting the ILES field of applications.

Since no explicit filter is required, the subgrid scale stress tensor and the commutation error are emitted. Their place is taken by the truncation error, τ, and Equation 1.3.4 is now written as below

$$\frac{\partial \bar{\mathbf{u}}}{\partial t} + \nabla \cdot (\bar{\mathbf{u}} \otimes \bar{\mathbf{u}}) + \frac{1}{\rho}\nabla \bar{p} = -\nabla \cdot \tau. \tag{1.3.13}$$

The over-bars appearing in Equation 1.3.13 correspond to averages obtained from the finite volume formulation (which can be considered as implicit filtering) in contrast

with LES where they denote the filtered grid scales. High order discretisation and fine grid resolution ensure that the leading truncation error remains small and provides adequate dissipation in order to satisfy the SGS properties and produce physical results [21, 28].

In order to demonstrate the similarities between the subgrid stress tensor in LES, τ^{sgs}, and the truncation error term in ILES, τ, Drikakis and Rider [18] focused on investigating the spatial errors in one dimensional equation of the following formulation

$$\mathbf{U}_j^{n+1} = \mathbf{U}_j^n - \frac{\Delta t}{\Delta x}\left[\mathbf{E}_{j+1/2} - \mathbf{E}_{j-1/2}\right] , \tag{1.3.14}$$

where **U** stands for the array of the dependent variables and **E** is the non-linear inviscid flux vector as mentioned above in Section 1.3. The superscript n denotes the current time level and the subscript j represents the position in space. When the flow field is approximated via piecewise constant discretisation, the dependent variables are double valued at the cell interface. To determine the fluxes using the left and right values of the conserved variables a reconstruction step and a Riemann solver are used (a more detailed description of high resolution methods is given in Section 2.3). The transported fluxes at the cell boundary are then given by

$$\mathbf{E}_{j+1/2} = \frac{1}{2}\left[\mathbf{E}_{j+1/2,R} + \mathbf{E}_{j+1/2,L}\right] - \frac{|\mathbf{E}'|}{2}\left[\mathbf{U}_{j+1/2,R} - \mathbf{U}_{j+1/2,L}\right] , \tag{1.3.15}$$

with $\mathbf{E}'$ being equal to $\partial\mathbf{E}/\partial\mathbf{U}$.

As found in Drikakis and Rider [18], the general form of the modified Equation 1.3.14, produced a truncation term at second order of accuracy given by

$$\boldsymbol{\tau} = -c_1\Delta^2\mathbf{E}'\nabla^2\mathbf{U} - c_2\Delta^2\mathbf{E}''\left(\nabla\mathbf{U}\nabla\mathbf{U}\right) , \tag{1.3.16}$$

where c_1 and c_2 are two constants depending on the discretisation scheme and Δ is the cell width. Clearly, the leading term of the truncation error is identical to scale-similarity subgrid model in conventional LES (see Equation 1.3.11). Therefore, the SGS properties are satisfied without the need for an explicit subgrid model thus the ILES approach is proven simpler and more computationally efficient.

A limited number of studies using ILES for simulating incompressible flows around bluff bodies can be found in Fureby et al. [23]. The first study dealt with the flow past a circular cylinder at Reynolds numbers of 3900 and 140000. Results obtained with various models including two variants of LES models, ILES coupled with FTC limiter and a wall model, two RANS models, the Reynolds stress equation model and finally DNS were compared against experimental data. Mean streamwise velocity profiles at cross sections revealed very good agreement with the experimental data and there was no obvious difference in the results when the LES and the ILES models are used. Nevertheless, RANS was the least accurate among all. Comparisons along the centerline showed that the LES models were underpredicting the velocity profile to a small extent, whereas the ILES maintained its accuracy in prediction.

Flow around a surface mounted cube representing a prototype for flows around buildings, was used in order to investigate the performance of ILES [23]. Data produced from this study was compared against the experimental study of Martinuzzi and Tropea [53] and the LES study found in Rodi [65].The simulated flow features were found to show accurate representation of the flow physics apart from the location of the horseshoe vortex which was expected to be closer to the upstream face of the cube and the size of the recirculation zone at the wake. However, the time averaged velocity profiles provide reasonable agreement with the experimental data.

Regarding the limited number of cases dealing with environmental flows, it becomes clear that the field of modelling urban areas using ILES has not been explored yet.

1.4 Aims and Objectives

Many environmental flows are inherently turbulent, but in cases where wall mounted obstacles are interfering, the complexity of the flow field is rapidly increased. The accurate representation of this type of flow is of great interest in many engineering applications involving pedestrian comfort, pollutant dispersion and urban design. Important experimental work has been conducted, providing essential information about the physics of the flows. With the rapid technological progress, Computational Fluid Dynamics became a new analysis tool promising accurate prediction of the flows with reduced expense. However, increased accuracy may result in a complex numerical formulation and unaffordable CPU time requirements. The challenge in CFD is to develop a universal model able to be applied in every turbulent flow with the same degree of accuracy and with the simplest possible formulation.

To date, the most promising approach in simulating turbulent flows is the Large Eddy Simulation. However, the requirements of a subgrid model depending on the flow under investigation and grid resolution places LES in the category of relatively expensive numerical methods. In the same family of approaches, Implicit Large Eddy Simulation is gaining popularity due to its implicit treatment of turbulence. However, in the field of ILES there are still many unexplored regions regarding its mechanisms and its applicability to all turbulent flows.

The aim of this thesis is to evaluate the applicability of Implicit Large Eddy Simulation to flows around model-buildings pertinent to environmental flows in urban areas. The choice of simulating flows within arrays of obstacles lies on the fact that the case specific boundary conditions (fully periodic conditions) remove the need for setting appropriate inlet conditions as it would have been required for flows around a single obstacle. Additionally, the flow pattern within a matrix of models shares some of the key features found around a single isolated model, however, the flow in an obstacle's wake is always affected by the presence of its neighboring ones.

The specific objectives are:

- Evaluate the performance of ILES and analyse the physics involved in flows

around uniform height urban-like roughness elements and validate against available experimental, DNS and LES data,

- Evaluate the flow topology in a more complex case regarding non uniform height elements.

The content of this thesis is outlined as follows:

Chapter 1. Introduction to the basic ideas of atmospheric boundary layer, building aerodynamics and turbulence.

Chapter 2. Description of the governing equations and the numerical framework.

Chapter 3. ILES of flows around arrays of uniform height wall roughness elements in staggered configuration.

Chapter 4. ILES of flows around arrays of non uniform height roughness elements in staggered configuration.

Chapter 5. A summary of this thesis, conclusions extracted and recommendations for future work.

Additional detailed information complementing the main body of the thesis is provided in the appendices.

CHAPTER 2

Numerical Approach

A three dimensional unsteady compressible solver is used for the numerical simulations of this study. Although the flows under investigation are incompressible, it was decided to proceed with the compressible solver based on the fact that initial attempts to simulate high order schemes with an incompressible code at moderate to high Reynolds numbers produced results with less efficiency than the compressible code. Therefore, throughout the description of the numerical framework, the flow will be denoted as compressible with low Mach number features.

A finite volume method is applied by using a curvilinear coordinate system and the fluid's governing equations are solved by employing a number of space and time discretization schemes. More precisely, different approaches are used for the spatial discretisation of the inviscid and viscous fluxes. For the former, a high-resolution Godunov-type method, whereas for the latter a central difference scheme are used. The time integration is obtained by explicit Runge Kutta methods. Finally, the code allows for parallel computing and domain decomposition.

2.1 Governing Equations

The motion of a fluid is described by a set of fundamental equations, the Navier Stokes equations (hereafter N-S), for continuity, momentum and energy. These equations are the mathematical expressions for the three fundamental conservation laws (Mass Conservation, Newton's Second Law, First Law of Thermodynamics) upon which all fluid dynamics is founded [2].

The set of N-S for an unsteady three dimensional compressible viscous fluid flow in conservation form is displayed below:

Continuity Equation

$$\frac{\partial \rho}{\partial t} + \nabla \cdot (\rho \mathbf{u}) = 0 \,, \tag{2.1.1}$$

Momentum Equation

$$\frac{\partial \rho \mathbf{u}}{\partial t} + \nabla \cdot (\rho \mathbf{u} \otimes \mathbf{u}) = +\nabla \cdot \mathbf{S} \,, \tag{2.1.2}$$

Energy Equation

$$\frac{\partial e}{\partial t} + \nabla \cdot (e\mathbf{u}) = +\nabla \cdot (\mathbf{S} \cdot \mathbf{u}) - \nabla \cdot \mathbf{q} \,, \tag{2.1.3}$$

where **u** represents the velocity components along all three directions, ρ the density, e the total energy per unit volume and **q** the heat flux. The stress tensor **S** denotes fluid's stress in terms of thermodynamic pressure p and the viscous stresses [18, 83]. The stress tensor **S** can be written as

$$\mathbf{S} = -p\,\mathbf{I} + \mathbf{T} \,, \tag{2.1.4}$$

where **I** is the unity tensor

$$\mathbf{I} = \begin{pmatrix} 1 & 0 & 0 \\ 0 & 1 & 0 \\ 0 & 0 & 1 \end{pmatrix} , \tag{2.1.5}$$

and **T** is the viscous stress tensor

$$\mathbf{T} = \begin{pmatrix} \tau_{xx} & \tau_{xy} & \tau_{xz} \\ \tau_{yx} & \tau_{yy} & \tau_{yz} \\ \tau_{zx} & \tau_{zy} & \tau_{zz} \end{pmatrix} . \tag{2.1.6}$$

A complete description of **T** is given in Appendix A.

The heat flux **q** expresses the net rates of heat transfer across the boundaries of a volume due to temperature gradients. Their mathematical relation is given by Fourier's heat conduction law

$$\mathbf{q} = -\kappa \nabla T \,, \tag{2.1.7}$$

where κ is the thermal conductivity coefficient and T is the temperature.

When counting the number of equations and unknown variables in the N-S equations as described above, it is noticed that the number of equations is less than the number of variables; five equations whereas six variables. In order to close the set of N-S, the gas is assumed to be a perfect gas (negligible inter molecular forces) and the *thermal equation of state* is used,

$$p = \rho R T \,, \tag{2.1.8}$$

where the gas constant of air is typically $R = 287.05\,\mathrm{Nm/(kg \cdot K)}$.

Based on the above assumption, an unknown T is introduced which leads to a second assumption that the perfect gas is calorically perfect (constant specific heats). Temperature T is then related to internal energy e_i according to the *caloric equation of state*

$$e_i = c_v T \,. \tag{2.1.9}$$

Additional relations specifying the constant specific heats c_v and c_p and the ratio of specific heats γ are given as

$$c_p - c_v = R \,, \quad c_v = \frac{R}{\gamma - 1} \,, \quad c_p = \frac{\gamma R}{\gamma - 1} \,, \quad \gamma = \frac{c_p}{c_v} \,. \tag{2.1.10}$$

The typical value of γ for air is equal to 1.4.

The total energy per unit volume is often defined as the summation of internal energy per unit volume and kinetic energy per unit volume. Thus, the energy equation can be written as

$$e = \frac{p}{\gamma - 1} + \frac{\rho}{2}\left(u^2 + v^2 + w^2\right) . \tag{2.1.11}$$

Complementary equations indicating the fluid's properties should be introduced as well. The relation between the dynamic viscosity coefficient μ and absolute temperature T of an ideal gas is expressed in Sutherland's law

$$\mu = \mu_0 \left(\frac{T}{T_0}\right)^{3/2} \frac{T_0 + 110.4K}{T + 110.4K} , \tag{2.1.12}$$

where T is in Kelvin and the reference viscosity is $\mu_0 = 1.7894 \times 10^{-5}\,\mathrm{kg/(m \cdot s)}$ at the reference temperature $T_0 = 288.16\,\mathrm{K}$.

The last coefficient to be defined is the thermal conductivity coefficient κ. In Anderson [2] it is stated that when the fluid is assumed to be a perfect gas, Prandtl number (Pr) is constant (approximately equal to 0.71) and κ can be obtained by solving:

$$\mathrm{Pr} = \frac{c_p \mu}{\kappa} , \tag{2.1.13}$$

Before closing this section, it should be mentioned that the variables in the N-S are often replaced by their dimensionless counterparts. Non dimensionalisation of the flow field parameters simplifies the physical system by removing the units of the variables, a very useful transformation especially when numerical simulation techniques are applied and validated against experiments.

Non-dimensionalisation is attained by scaling all variables that appear in the N-S with basic reference quantities for the density (ρ_∞), flow velocity (u_∞), dynamic viscosity (μ_∞) and length (l_∞). The scaled dimensionless variables are the following

$$\begin{aligned}
t^* &= \frac{t}{l_\infty / u_\infty} , & x^* &= \frac{x}{l_\infty} , & y^* &= \frac{y}{l_\infty} , & z^* &= \frac{z}{l_\infty} , \\
\rho^* &= \frac{\rho}{\rho_\infty} , & u^* &= \frac{u}{u_\infty} , & v^* &= \frac{v}{u_\infty} , & w^* &= \frac{w}{u_\infty} , \\
e^* &= \frac{e}{\rho_\infty u_\infty^2} , & p^* &= \frac{p}{\rho_\infty u_\infty^2} , & \mu^* &= \frac{\mu}{\mu_\infty} .
\end{aligned} \tag{2.1.14}$$

Specifically, l_∞ corresponds to the reference length scale, ρ_∞ to the free stream density whereas the values of u_∞ and μ_∞ are derived from Equation 2.1.15.The calculation of μ_∞ is determined in such way that the numerical Reynolds number and the reference Reynolds number provided by the experiment are consistent.

$$u_\infty = M\sqrt{\frac{\gamma p}{\rho}}\ , \mu_\infty = \frac{u_\infty}{U_r}\mu_r \tag{2.1.15}$$

where M is the Mach number, p the pressure, ρ the density and finally U_r the free stream velocity.

All variables in the N-S can now be replaced by their dimensionless counterparts and therefore the new set of N-S is written in the following form

$$\frac{\partial \rho^*}{\partial t^*} + \nabla \cdot (\rho^* u_i^*) = 0\ , \tag{2.1.16}$$

$$\frac{\partial \rho^* u_i^*}{\partial t^*} + \nabla \cdot (\rho^* u_i^* \otimes u_i^*) = -\nabla \cdot \mathbf{S}^*\ , \tag{2.1.17}$$

$$\frac{\partial e^*}{\partial t^*} + \nabla \cdot (e^* u_i^*) = -\nabla \cdot (\mathbf{S}^* \cdot u_i^*) - \nabla \cdot \mathbf{q}^*\ , \tag{2.1.18}$$

where u_i^* is the non dimensional velocity vector, q^* is the non dimensional heat flux defined as

$$q^* = \frac{\gamma}{Pr}\nabla T^*\ , \tag{2.1.19}$$

and $\mathbf{S}^*$ is the non-dimensional stress tensor given by

$$\mathbf{S}^* = -p^*\mathbf{I} + \frac{1}{Re}\mathbf{T}^* \tag{2.1.20}$$

where Re is the Reynolds number given by

$$Re = \frac{\rho_\infty u_\infty l_\infty}{\mu_\infty}\ . \tag{2.1.21}$$

Hereafter, all variables will be considered dimensionless and the superscript $*$ will be omitted for clarity.

2.1.1 Cartesian And Curvilinear Equations in Matrix Form

The set of N-S for compressible flows, Equations 2.1.16 to 2.1.18, can be handled as a single equation. The equation consists of vectors representing the unknown variables as well as the inviscid and viscous fluxes. The usefulness of having only one equation lies on the fact that the number of algebraic operations is minimised, thus the complexity of developing CFD codes is reduced. The conservative matrix form of the N-S in Cartesian coordinates is given by:

$$\frac{\partial \mathbf{U}}{\partial t} + \frac{\partial \mathbf{E}}{\partial x} + \frac{\partial \mathbf{F}}{\partial y} + \frac{\partial \mathbf{G}}{\partial z} = \frac{\partial \mathbf{L}}{\partial x} + \frac{\partial \mathbf{M}}{\partial y} + \frac{\partial \mathbf{N}}{\partial z}\,, \tag{2.1.22}$$

where **U** is the unknown solution vector; **E**, **F**, **G** and **L**, **M**, **N** correspond to the inviscid and viscous Cartesian fluxes respectively,

$$\mathbf{U} = \begin{pmatrix} \rho \\ \rho u \\ \rho v \\ \rho w \\ e \end{pmatrix},\ \mathbf{E} = \begin{pmatrix} \rho u \\ \rho u^2 + p \\ \rho v u \\ \rho w u \\ (e+p)u \end{pmatrix},\ \mathbf{F} = \begin{pmatrix} \rho v \\ \rho u v \\ \rho v^2 + p \\ \rho w v \\ (e+p)v \end{pmatrix},\ \mathbf{G} = \begin{pmatrix} \rho w \\ \rho u w \\ \rho v w \\ \rho w^2 + p \\ (e+p)w \end{pmatrix},$$

$$\mathbf{L} = \frac{1}{Re}\begin{pmatrix} 0 \\ \tau_{xx} \\ \tau_{xy} \\ \tau_{xz} \\ u\tau_{xx} + v\tau_{xy} + w\tau_{xz} - q_x \end{pmatrix},\ \mathbf{M} = \frac{1}{Re}\begin{pmatrix} 0 \\ \tau_{yx} \\ \tau_{yy} \\ \tau_{yz} \\ u\tau_{yx} + v\tau_{yy} + w\tau_{yz} - q_y \end{pmatrix},$$

$$\mathbf{N} = \frac{1}{Re}\begin{pmatrix} 0 \\ \tau_{zx} \\ \tau_{zy} \\ \tau_{zz} \\ u\tau_{zx} + v\tau_{zy} + w\tau_{zz} - q_z \end{pmatrix}. \tag{2.1.23}$$

In Equation 2.1.23, $q_{x,y,z}$ represent the net rates of heat transfer along x-, y- and z-direction and τ_{ij} stand for the viscous stress as described in Appendix A.

Most CFD applications do not deal with simple geometries and cannot be represented by Cartesian coordinates. A transformation of the Cartesian coordinates to curvilinear coordinates is required. The transformation is obtained using the Jacobian [18, 31]. Equation 2.1.22 is multiplied with the Jacobian determinant (hereafter J) and the Cartesian (x, y, z) coordinates are replaced with the curvilinear (ξ, η, ζ) counterparts. The Jacobian determinant can be written as

$$J = \left|\frac{\partial(x,y,z)}{\partial(\xi,\eta,\zeta)}\right| = x_\xi\left(y_\eta z_\zeta - y_\zeta z_\eta\right) + y_\xi\left(z_\eta x_\zeta - z_\zeta x_\eta\right) + z_\xi\left(x_\eta y_\zeta - x_\zeta y_\eta\right), \tag{2.1.24}$$

where $\xi = \xi(x, y, z, t)$, $\eta = \eta(x, y, z, t)$, $\zeta = \zeta(x, y, z, t)$ and $\tau = t$

The independent variables appear in the form of derivatives in the equations therefore the derivatives should be transformed from (x, y, z) space to (ξ, η, ζ) space. The derivative transformation will be achieved by following the chain rule of differential calculus

as shown below

$$\begin{aligned}
\frac{\partial}{\partial x} &= \left(\frac{\partial}{\partial \xi}\right)\frac{\partial \xi}{\partial x} + \left(\frac{\partial}{\partial \eta}\right)\frac{\partial \eta}{\partial x} + \left(\frac{\partial}{\partial \zeta}\right)\frac{\partial \zeta}{\partial x}\,, \\
\frac{\partial}{\partial y} &= \left(\frac{\partial}{\partial \xi}\right)\frac{\partial \xi}{\partial y} + \left(\frac{\partial}{\partial \eta}\right)\frac{\partial \eta}{\partial y} + \left(\frac{\partial}{\partial \zeta}\right)\frac{\partial \zeta}{\partial y}\,, \\
\frac{\partial}{\partial z} &= \left(\frac{\partial}{\partial \xi}\right)\frac{\partial \xi}{\partial z} + \left(\frac{\partial}{\partial \eta}\right)\frac{\partial \eta}{\partial z} + \left(\frac{\partial}{\partial \zeta}\right)\frac{\partial \zeta}{\partial z}\,, \\
\frac{\partial}{\partial t} &= \frac{\partial}{\partial \tau}\,.
\end{aligned} \tag{2.1.25}$$

As a result, the fluxes in curvilinear coordinates using the Jacobian matrix are written as

$$Inviscid\,fluxes = \begin{cases} \tilde{\mathbf{E}} &= J(\mathbf{E}\frac{\partial \xi}{\partial x} + \mathbf{F}\frac{\partial \xi}{\partial y} + \mathbf{G}\frac{\partial \xi}{\partial z}\,), \\ \tilde{\mathbf{F}} &= J(\mathbf{E}\frac{\partial \eta}{\partial x} + \mathbf{F}\frac{\partial \eta}{\partial y} + \mathbf{G}\frac{\partial \eta}{\partial z}\,), \\ \tilde{\mathbf{G}} &= J(\mathbf{E}\frac{\partial \zeta}{\partial x} + \mathbf{F}\frac{\partial \zeta}{\partial y} + \mathbf{G}\frac{\partial \zeta}{\partial z}\,). \end{cases} \tag{2.1.26}$$

$$Viscous\,fluxes = \begin{cases} \tilde{\mathbf{L}} &= J(\mathbf{L}\frac{\partial \xi}{\partial x} + \mathbf{M}\frac{\partial \xi}{\partial y} + \mathbf{N}\frac{\partial \xi}{\partial z}\,), \\ \tilde{\mathbf{M}} &= J(\mathbf{L}\frac{\partial \eta}{\partial x} + \mathbf{M}\frac{\partial \eta}{\partial y} + \mathbf{N}\frac{\partial \eta}{\partial z}\,), \\ \tilde{\mathbf{N}} &= J(\mathbf{L}\frac{\partial \zeta}{\partial x} + \mathbf{M}\frac{\partial \zeta}{\partial y} + \mathbf{N}\frac{\partial \zeta}{\partial z}\,), \end{cases} \tag{2.1.27}$$

Finally, the new system of compressible N-S in curvilinear coordinates is given by Equation 2.1.28:

$$\frac{\partial \tilde{\mathbf{U}}}{\partial t} + \frac{\partial \tilde{\mathbf{E}}}{\partial \xi} + \frac{\partial \tilde{\mathbf{F}}}{\partial \eta} + \frac{\partial \tilde{\mathbf{G}}}{\partial \zeta} = \frac{\partial \tilde{\mathbf{L}}}{\partial \xi} + \frac{\partial \tilde{\mathbf{M}}}{\partial \eta} + \frac{\partial \tilde{\mathbf{N}}}{\partial \zeta}\,, \tag{2.1.28}$$

where

$$\tilde{\mathbf{U}} = J\mathbf{U} \tag{2.1.29}$$

In the sections that follow, any reference to the set of N-S will assume Equation 2.1.28.

2.2 The Finite Volume Concept

The governing equations are solved using a Finite Volume method. According to this specific concept the domain under investigation is divided into a number of control volumes (or finite volumes).They can be of any shape therefore this method is suitable for unstructured grids and complex geometries. The derivatives in space are discretised at the centre of the control volume (i, j, k) using the inter-cell flux values across the faces. A schematic representation of the discretisation scheme is given in Figure 2.1.

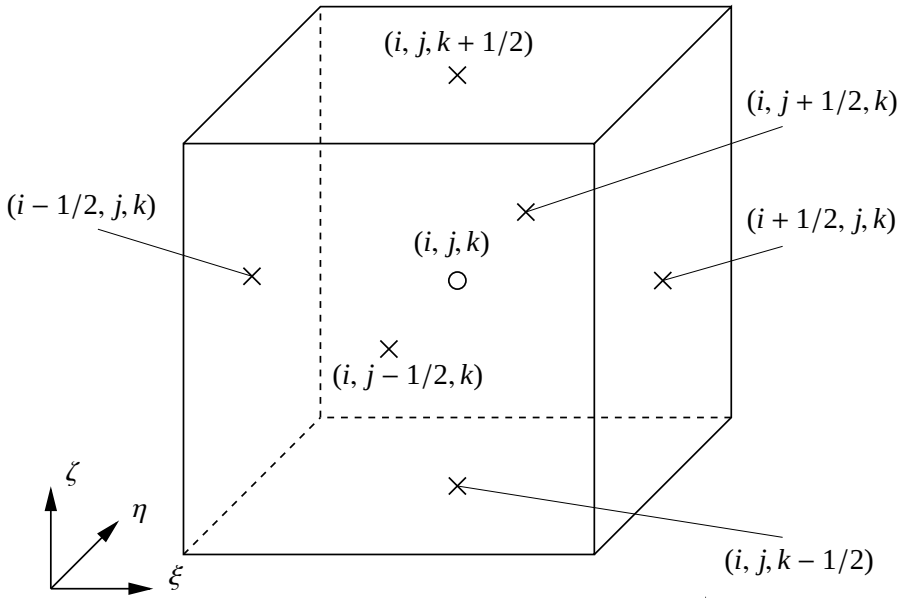

Figure 2.1: Three-dimensional notation for a finite volume [30]

Consequently, for piecewise constant fluxes, Equation 2.1.28 can be written as

$$\begin{aligned}\frac{\partial \mathbf{U}}{\partial t} = &- \frac{\mathbf{E}_{i+1/2,j,k} - \mathbf{E}_{i-1/2,j,k}}{\Delta\xi} - \frac{\mathbf{F}_{i,j+1/2,k} - \mathbf{F}_{i,j-1/2,k}}{\Delta\eta} - \frac{\mathbf{G}_{i,j,k+1/2} - \mathbf{G}_{i,j,k-1/2}}{\Delta\zeta} \\ &+ \frac{\mathbf{L}_{i+1/2,j,k} - \mathbf{L}_{i-1/2,j,k}}{\Delta\xi} + \frac{\mathbf{M}_{i,j+1/2,k} - \mathbf{M}_{i,j-1/2,k}}{\Delta\eta} + \frac{\mathbf{N}_{i,j,k+1/2} - \mathbf{N}_{i,j,k-1/2}}{\Delta\zeta},\end{aligned} \tag{2.2.1}$$

or

$$\frac{\partial \mathbf{U}}{\partial t} = RHS \tag{2.2.2}$$

All the discretised fluxes comprising the right-hand side (RHS) of the equation are calculated independently and once obtained they are added up. The complete system is then integrated in time.

The inviscid fluxes, **E**, **F** and **G**, are non-linear and their spatial discretisation involves a Riemann solver and high resolution reconstruction methods, whereas the linear viscous fluxes **L**, **M** and **N**, are simply given by a central difference scheme.

2.3 High-Resolution Methods

High-resolution methods are non-linear methods even when the equations they approximate are linear. They are designed to eliminate or reduce oscillations in areas where shock waves occur and the variables are discontinuous. They also allow higher than 1^{st} order of accuracy when the solution is smooth. To achieve the above, they introduce non-linear differencing methods where the computational stencil is a function of space and time. The stencil adapts itself depending on the local solution in order to produce

physical results even in areas characterised by high gradients.These are the main differences between high-resolution methods and non-linear adaptive methods (such as the non-linear combination of two 1^{st} order methods) and yet not high-resolution.

According to Harten's definition [34], high-resolution methods have the following properties:

1. Provide at least second order of accuracy in smooth areas of the flow.
2. Produce numerical solutions relatively free from spurious oscillations,
3. In the case of discontinuities, the number of grid points in the transition zone containing the shock wave is smaller in comparison with that of first order monotone methods.

In numerical approaches where the flow field is approximated via piecewise constant discretisation, which represents the volumetric averages of the exact problem, the conserved variables are double valued at cell edges. In order to reduce those discontinuities, high-resolution methods introduce an interpolation step that reconstructs the variables in such way that they are a more accurate representation of the exact solution. With the reconstructed left and right cell values obtained, the next step to be taken is to apply a Riemann solver.

During the last decades, a number of high-resolution schemes were introduced with the most popular being the Monotonic Upwind Scheme for Conservation Laws, the essentially nonoscillatory and the weighted essentially nonoscillatory. Some of the schemes are also utilising the so called *slope limiters*. The limiters are correction mechanisms that ensure that the reconstructed values satisfy at least one of the three properties of high resolution methods (Monotonicity Preserving, Total Variation Diminishing or Monotone) and that the generation of oscillations is avoided near discontinuities.

As part of this thesis, two reconstruction schemes were used for the interpolation step with different orders of accuracy. These are the *Monotonic Upwind Scheme for Scalar Conservation Laws* (MUSCL) by van Leer [82] and the *Weighted Essentially Non-Oscillatory* (WENO) scheme by Liu et al. [51].

2.3.1 MUSCL Schemes

The interpolation formula for calculating the left and right states of the conservative variables using the MUSCL schemes according to Toro [80] is

$$\begin{aligned}
\mathbf{U}_{L,i+1/2} =& \mathbf{U}_i \quad + \frac{1}{4}\left[(1-k)\,\phi\,(r_L)\,(\mathbf{U}_i - \mathbf{U}_{i-1}) + (1+k)\,\phi\left(\frac{1}{r_L}\right)(\mathbf{U}_{i+1} - \mathbf{U}_i)\right], \\
\mathbf{U}_{R,i+1/2} =& \mathbf{U}_{i+1} - \frac{1}{4}\left[(1-k)\,\phi\,(r_R)\,(\mathbf{U}_{i+2} - \mathbf{U}_{i+1}) + (1+k)\,\phi\left(\frac{1}{r_R}\right)(\mathbf{U}_{i+1} - \mathbf{U}_i)\right],
\end{aligned} \tag{2.3.1}$$

where $-1 \leq k \leq 1$ and ϕ is a limiter function based on the slopes of the conserved variables. Different variants of the MUSCL scheme are produced depending on the value of k from fully upwind for $k = -1$, centrered scheme for $k = 0$.

Second-order limiters. The definition of second-order accurate limiter mechanisms is given by the left and the right ratio of the slopes of the cell averaged conserved variables at $(i-1)$, (i), $(i+1)$ and $(i+2)$,

$$\begin{aligned} r_L &= \frac{\mathbf{U}_{i+1} - \mathbf{U}_i}{\mathbf{U}_i - \mathbf{U}_{i-1}} , \\ r_R &= \frac{\mathbf{U}_{i+1} - \mathbf{U}_i}{\mathbf{U}_{i+2} - \mathbf{U}_{i+1}} . \end{aligned} \tag{2.3.2}$$

The most popular second-order limiters, satisfying monotonicity and reducing to a piecewise linear method near local extrema in order to avoid unphysical oscillations, are the MinMod, Van Leer and Van Albada limiters. They can be found in Laney [48], LeVeque [49], Toro [80].

The Van Albada limiter (hereafter VA) is employed in this thesis and it is defined as

$$\phi_{VA} = \begin{cases} 0 & \text{if } r \leq 0 \\ \frac{r(1+r)}{1+r^2} & \text{if } r > 0 \end{cases} , \tag{2.3.3}$$

Fifth-order limiter.

A fifth-order accurate MUSCL scheme proposed by Kim and Kim [43] uses a six-point stencil $(i-2)$, $(i-1)$, (i), $(i+1)$ $(i+2)$ and $(i+3)$. The slope ratios are calculated as

$$\begin{aligned} r_{L,i} &= \frac{\mathbf{U}_{i+1} - \mathbf{U}_i}{\mathbf{U}_i - \mathbf{U}_{i-1}} , \\ r_{R,i} &= \frac{\mathbf{U}_i - \mathbf{U}_{i-1}}{\mathbf{U}_{i+1} - \mathbf{U}_i} , \end{aligned} \tag{2.3.4}$$

and the limiter ϕ is calculated by

$$\begin{aligned} \phi^*_{L,M5} &= \frac{-2/r_{L,i-1} + 11 + 24 r_{L,i} - 3 r_{L,i} r_{L,i+1}}{30} , \\ \phi^*_{R,M5} &= \frac{-2/r_{R,i+2} + 11 + 24 r_{R,i+1} - 3 r_{R,i+1} r_{R,i}}{30} . \end{aligned} \tag{2.3.5}$$

To ensure monotonicity the function ϕ is limited and its final form is given by

$$\phi_{\frac{L}{R},M5} = max(0, min(2, 2 r_{\frac{L}{R},i}, \phi^*_{\frac{L}{R},M5})) \tag{2.3.6}$$

2.3.2 WENO Schemes

WENO schemes were introduced in order to overcome any drawbacks that occurred in ENO schemes while preserving their robustness and high order of accuracy. ENO

schemes were first proposed by Harten et al. [35]. They do not support any limiter function, instead they choose the smoothest candidate stencil that is possible to cover a zone in the computational domain. The stencil adapts to any change of the solution (for example round off perturbations near zeroes of the solution) and even in smooth regions where adaptation is not necessary [41].

As new improved schemes, WENO schemes were introduced by Balsara and Shu [5] and Jiang and Shu [41]. WENO schemes use a convex combination of all the available stencils instead of using only one in order to interpolate an interface value. A weight is assigned to each candidate stencil, indicating the contribution to the final result. The weights are chosen in such a way that smooth regions have higher contributions, whereas regions near discontinuities have no contribution. WENO schemes can obtain an accuracy of $2s-1$, with s being the size of the stencil.

The WENO schemes employed in this thesis are 5^{th} and 9^{th} order accurate. However, only the 5th order WENO scheme will be presented as an example in this section [56, 57].

Any WENO scheme can be defined by the following general formulation

$$\mathbf{U}_{j+1/2} = \sum_{k=1}^{s} \omega_k \mathbf{U}^k_{j+1/2}, \tag{2.3.7}$$

where $\mathbf{U}^k_{j+1/2}$ is the interpolated value for each stencil at the interface $j+1/2$, ω_k is the weight for each stencil and $k = 1...s$. Equation 2.3.7 can be used for either the left or right extrapolated variable.

In Titarev and Toro [79], the weights ω_k are calculated as

$$\omega_k = \frac{\alpha_k}{\sum_{i=1}^{s} \alpha_i}\ , \tag{2.3.8}$$

$$\alpha_k = \frac{\bar{\omega_k}}{(\epsilon + \beta_k)^p}\ , \tag{2.3.9}$$

where $\bar{\omega_k}$ are the optimal weights, ϵ is a small positive number used in order to avoid division by zero in case of smooth flow, β_k are the smoothness indicators for each stencil and p is a free parameter.

For the specific case of the 5_{th} order accurate WENO scheme three stencils are required. The three available stencils for reconstruction are

$$\begin{aligned} S_1 &= (j, j+1, j+2)\ , \\ S_2 &= (j-1, j, j+1)\ , \\ S_3 &= (j-2, j-1, j)\ . \end{aligned} \tag{2.3.10}$$

For $s = 3$, Equation 2.3.7 is written as

$$\mathbf{U}_{j+1/2} = \sum_{k=1}^{3} \omega_k \mathbf{U}^k_{j+1/2} \tag{2.3.11}$$

The smoothness indicators are given by

$$\begin{aligned}\beta_1 =& \frac{13}{12}(\mathbf{U}_j - 2\mathbf{U}_{j+1} + \mathbf{U}_{j+2})^2 + \frac{1}{4}(3\mathbf{U}_j - 4\mathbf{U}_{j+1} + \mathbf{U}_{j+2})^2 \ , \\ \beta_2 =& \frac{13}{12}(\mathbf{U}_{j-1} - 2\mathbf{U}_j + \mathbf{U}_{j+1})^2 + \frac{1}{4}(\mathbf{U}_{j-1} - \mathbf{U}_{j+1})^2 \ , \\ \beta_3 =& \frac{13}{12}(\mathbf{U}_{j-2} - 2\mathbf{U}_{j-1} + \mathbf{U}_j)^2 + \frac{1}{4}(\mathbf{U}_{j-2} - 4\mathbf{U}_{j-1} + 3\mathbf{U}_j)^2\end{aligned} \tag{2.3.12}$$

and the optimal weights for the left reconstructed variable $\mathbf{U}^L_{j+1/2}$ are

$$\bar{\omega_0} = \frac{3}{10} \ , \bar{\omega_1} = \frac{3}{5} \ , \bar{\omega_2} = \frac{1}{10}. \tag{2.3.13}$$

Since the optiomal weights and the smoothness indicators are known, $\mathbf{U}^L_{j+1/2}$ can be calculated using Equation 2.3.7.

In a similar way the right extrapolated variable $\mathbf{U}^R_{j-1/2}$ can be found by using the same smoothness indicators and the following optimal weights obtained by symmetry

$$\bar{\omega_1} = \frac{1}{10} \ , \bar{\omega_2} = \frac{3}{5} \ , \bar{\omega_3} = \frac{3}{10} \tag{2.3.14}$$

However, in the work of Henrick et al. [37] it is mentioned that the above formulation does not attain maximum accuracy around critical points. To overcome the problem and improve the order of accuracy, mapping of the weights has been suggested in Mosedale [57]. The amended weights are:

$$\omega^M_k = \frac{\alpha^*_k}{\sum_{i=1}^3 \alpha^*_i} \ , \tag{2.3.15}$$

$$\alpha^*_k = g_k(\omega_k) \ , \tag{2.3.16}$$

$$g_k(\omega_k) = \frac{\omega_k(\bar{\omega}_k + \bar{\omega}^2_k - 3\bar{\omega}_k\omega_k + \omega^2_k)}{\bar{\omega}^2_k + \omega_k(1 - 2\bar{\omega}_k)} \ . \tag{2.3.17}$$

2.4 Low Mach Number Modification

The Finite Volume (FV) high-resolution schemes have been successful in simulating a variety of applications in the context of compressible flows [77]. However, they exhibit poor performance due to excessive numerical dissipation when simulating low Mach number features. Specifically, Guillard [29] found that when artificial viscosity is added to stabilise the solution in areas with steep discontinuities, the calculated pressure at the cell interface contained an undesirable scaling factor with respect to Mach number which led to one order higher pressure. There was no reported analytical study

in the literature in which the link between the generation of local entropy and kinetic energy dissipation rate had been investigated. An extensive study was performed by Thornber et al. [78] on the specific study. Based on the study's findings, it was stated that the increase of dissipation in Low Mach numbers was a property of the discrete system arising from the interaction between the governing equations and the reconstruction process. Specifically, it was proven that in Finite volume Godunov method, the local increase of entropy was proportional to the $\frac{\Delta u^2}{\alpha}$ where u is the velocity normal to the cell interface and α is the speed of sound. Therefore, the rate of kinetic energy was rapidly decreased with decreasing Mach numbers (irreversible dissipation of kinetic energy under the assumption of low local production of entropy).

In order to improve the scheme so that both compressible and incompressible flows can simulated accurately, a modification was proposed by Thornber et al. [77]. The modified numerical approach locally adapts the reconstructed variable in such way that minimum dissipation is allowed, shock waves are captured and, most importantly, there is no need for modifying the governing equations. The reconstructed left and right interface values combined with the *Low Mach Correction* (hereafter as LM) are defined as

$$\mathbf{U}_L^{LM} = \frac{1}{2}((1 + M_{min})\mathbf{U}_L + (1 - M_{min})\mathbf{U}_R), \tag{2.4.1}$$

$$\mathbf{U}_R^{LM} = \frac{1}{2}((1 + M_{min})\mathbf{U}_R + (1 - M_{min})\mathbf{U}_L) \tag{2.4.2}$$

where $M_{min} = min(1, M)$.

2.5 Riemann Solver

The reconstructed left and right values at the cell faces lead to discontinuities equivalent to the discontinuous states in the shock tube problem. In order to achieve only one flux transported through the cell boundary, local Riemann problems need to be solved.

Due to the cost of this procedure, even under the best of circumstances, and the relatively small practical value of an exact Riemann solution, the exact Riemann solvers have been replaced by approximated Riemann solvers in the vast majority of cases. The approximate Riemann solvers give a direct approximation of the intercell fluxes. A wave configuration (distinguishing the constant states of the solution) is assumed and, given the fact that the wave speeds can be obtained by an algorithm, an approximated expression of the fluxes is produced by applying the integral form of the conservation laws. In this thesis, the HLLC solver was applied for solving the inviscid fluxes as described in Toro [80]. A more detailed description of the solver is given in the following section.

2.5.1 HLLC Riemann solver

As mentioned above, the approximate Riemann solver assumes a wave configuration that separates the constant states of the solution. In the HLL solver, there were two waves (S_L and S_R) distinguishing three constant states (U_L, U_R and the *Star* intermediate region), whereas in the HLLC solver there are three waves and four regions. The third wave in the HLLC solver represents the missing contact wave. The *Star Region* is now split into two regions by the third additional wave.

Once the wave speeds are obtained, they are combined with the constant states of the variables in order to calculate the fluxes.

According to Toro [80], the fluxes are calculated in the following sequence:

1. Calculate the left and right states of the primitive variables using high-resolution reconstruction as described in Section 2.3.

2. Estimate the pressure in the star region using the left and right states of the primitive variables

$$p_* = \frac{1}{2}(p_L + p_R) - \frac{1}{2}(u_R - u_L)(\overline{\rho a}) \,,$$

   where $\bar{\rho}$ and $\bar{a}$ are the averaged density and speed of sound respectively

$$\bar{\rho} = \frac{1}{2}(\rho_L + \rho_R), \tag{2.5.1}$$

$$\bar{a} = \frac{1}{2}(a_L + a_R). \tag{2.5.2}$$

3. Proceed with the calculation of the S_L and S_R speeds using

$$S_L = u_L - a_L q_L \,, \quad S_R = u_R - a_R q_R \,,$$

   with

$$q_K = \begin{cases} 1 & \text{if} \quad p_* \le p_K \\ [1 + \frac{\gamma+1}{2\gamma}(p_*/p_K - 1)]^{\frac{1}{2}} & \text{if} \quad p_* > p_K \end{cases} \,,$$

   where K indicates the left or right states.

4. Determine the star wave speed

$$S_* = \frac{p_R - p_L + \rho_L u_L(S_L - u_L) - \rho_R u_R(S_R - u_R)}{\rho_L(S_L - u_L) - \rho_R(S_R - u_R)} \,.$$

5. Calculate the U_{*L} and U_{*R} states given by

$$\mathbf{U}_{*K} = \rho_K \left(\frac{S_K - u_K}{S_K - S_*}\right) \begin{pmatrix} 1 \\ S_* \\ v_K \\ w_K \\ \frac{E_K}{\rho_K} + (S_* - u_K)\left[S_* + \frac{p_K}{\rho_K(S_K - u_K)}\right] \end{pmatrix} .$$

6. Obtain the flux by applying the Rankine-Hugoniot conditions

$$\mathbf{F}_{i+1/2}^{HLLC} = \begin{cases} \mathbf{F}_L & if \quad 0 \leq S_L \\ \mathbf{F}_L + S_L(\mathbf{U}_{*L} - \mathbf{U}_L) & if \quad S_L \leq 0 \leq S_* \\ \mathbf{F}_R + S_R(\mathbf{U}_{*R} - \mathbf{U}_R) & if \quad S_* \leq 0 \leq S_R \\ \mathbf{F}_R & if \quad 0 \geq S_R \end{cases} .$$

2.6 Time Marching

The time derivatives appearing in the N-S described in the previous sections indicate unsteady problems whose solution can be obtained by time marching methods. According to the explicit time marching concept, the dependent variable under investigation is calculated at all grid points at time n+1 from all the known values at time n. In this fashion, the solution is progressively obtained by marching in steps of time.

The time integration approach that will be used in this thesis is the explicit Runge-Kutta method. The Runge-Kutta approaches are directly constructed from a Taylor series expansions. One of the key advantages is their simplicity when dealing with time step changes. That can be explained based on the fact that they are self-contained methods within a time step and they do not require storage across more than one time step [17, 18]. Higher accuracy is achieved when the number of stages (intermediate steps on which the current solution will be based on) is increased.

When rearranging Equation 2.1.28, the time derivative can be defined as a summation of the spatial derivatives

$$\frac{\partial \mathbf{U}}{\partial t} = -\frac{\partial \mathbf{E}}{\partial \xi} - \frac{\partial \mathbf{F}}{\partial \eta} - \frac{\partial \mathbf{G}}{\partial \zeta} + \frac{\partial \mathbf{L}}{\partial \xi} + \frac{\partial \mathbf{M}}{\partial \eta} + \frac{\partial \mathbf{N}}{\partial \zeta} = f(\mathbf{U}) , \tag{2.6.1}$$

In this thesis, only a 3^{rd} order Runge-Kutta was used as time integration method. For the sake of completeness, however, the simplest form of the method (1^{st} order Runge-Kutta) will be described as well.

2.6.1 First-Order Runge-Kutta

This is the most basic formulation of the Runge-Kutta methods. Only one previous time step is required in order to obtain the solution for the next time step according to

$$\frac{\mathbf{U}^{n+1} - \mathbf{U}^n}{\Delta t} = f(\mathbf{U}^n) , \tag{2.6.2}$$

with Δt being the time step, $\mathbf{U}^{n+1} = \mathbf{U}(t + \Delta t)$ and $\mathbf{U}^n = \mathbf{U}(t)$. The method is first order accurate in time. The 1^{st} order Runge-Kutta algorithm is also known as *the forward Euler method*.

2.6.2 Third-Order Runge Kutta

There are several Runge-Kutta algorithms of 3^{rd} order accuracy.

The standard 3^{rd} accurate Runge-Kutta method is a modification of the 1^{st} Runge-Kutta algorithm and it is given by

$$\begin{aligned} \frac{\mathbf{U}^1 - \mathbf{U}^n}{\Delta t} &= \frac{1}{3} f(\mathbf{U}^n) \,, \\ \frac{\mathbf{U}^2 - \mathbf{U}^n}{\Delta t} &= \frac{2}{3} f(\mathbf{U}^1) \,, \\ \frac{\mathbf{U}^{n+1} - \mathbf{U}^n}{\Delta t} &= \frac{1}{4}\left[f(\mathbf{U}^n) + 3 f(\mathbf{U}^2) \right] \,. \end{aligned} \tag{2.6.3}$$

The 3^{rd} TVD Runge-Kutta is being commonly used and its formulation, as given in Drikakis and Rider [18], consists of the following sequence

$$\begin{aligned} \frac{\mathbf{U}^1 - \mathbf{U}^n}{\Delta t} &= f(\mathbf{U}^n) \,, \\ \frac{\mathbf{U}^2 - \mathbf{U}^n}{\Delta t} &= \frac{1}{4}\left[f(\mathbf{U}^n) + f(\mathbf{U}^1) \right] \,, \\ \frac{\mathbf{U}^{n+1} - \mathbf{U}^n}{\Delta t} &= \frac{1}{6}\left[f(\mathbf{U}^n) + 4 f(\mathbf{U}^2) + f(\mathbf{U}^1) \right] \,. \end{aligned} \tag{2.6.4}$$

2.6.3 CFL Condition

When hyperbolic PDEs are solved numerically using explicit time integration schemes, the Courant-Friedrichs-Lewy number (hereafter CFL) is used as stability condition. The CFL number ensures that the global computational time step must be less or equal than the time it takes for the fastest acoustic wave to travel to the adjacent grid point. Hence, CFL is defined as

$$\Delta t = min\left(J \frac{CFL}{\lambda_{max}} \right) \,, \tag{2.6.5}$$

where J represents the local cell Jacobian determinant and λ are the associated local eigenvalues related to the inviscid fluxes **E**, **F**, **G**.

Depending on the time integration scheme, the value of CFL changes in order to reach a stable solution in time.

2.7 Parallel Computing

Simulating three dimensional turbulent flows demands high memory storage and high computational time. The solution to these problems is given via parallel computing. The physical domain is split into a number of individual blocks which are then assigned to a number of processors. The governing equations are solved in each one of these blocks separately, thus, instead of solving one global problem that would have high requirements in time, several smaller local problems are solved and run in parallel. A decomposition of a two dimensional grid into four equally sized blocks which are assigned to four processes is presented in Figure 2.2.

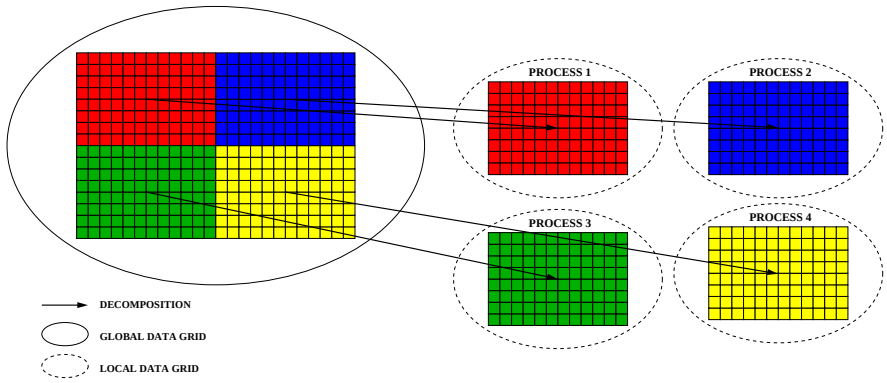

Figure 2.2: Decomposition of a two-dimensional global data domain over four processes [30].

For each process to be able to produce a solution to the local block requires communication and exchange of information among all the adjacent blocks.This communication is achieved by the MPI-1 standard. Further details on how the MPI procedure operates can be found in MacDonald et al. [52], Pacheco [61].

2.8 Case Specific Methodology

Two cases investigating the applicability of a number of high resolution schemes in the context of Implicit Large Eddy Simulation in flows within arrays of roughness elements will be presented in this thesis. The first case deals with flows within an array of four cubical elements in staggered configuration, whereas the second one simulates a more realistic representation of urban areas regarding flows around sixteen buildings of five different heights in the same alignment as in the first case.

The cases under investigation were simulated using the Compressible Navier Stokes Solver (hereafter CNS3D), a three dimensional compressible solver implemented in Fortran 77. The origins of the specific computational code are found in the works of Drikakis and Tsangaris [20], Drikakis and S. Tsangaris [19] and Zoltak and Drikakis

[90]. All geometries were meshed in the commercial software GridgenV15 using multi-block configurations.

The numerical studies had similar set up. To allow direct comparisons with the experimental data specific pre- and post- process procedures needed to be implemented in the CNS3D solver. The pre- processing procedure comprised of the addition of a constant pressure gradient term in the set of N-S equations right after the reconstruction step discussed in Section 2.3. Depending on the case under investigation a different value of the pressure gradient was added. The post- processing procedures involved the averaging of the numerical flow field ad hoc and also the collection of mean flow statistics (velocity and turbulent statistics) at a priori specified locations within each one of the two geometries under investigation.

2.8.1 Numerical Settings

The flows under consideration were simulated in near incompressible condition at Mach number of 0.2 using a compressible solver. The specific value of M=0.2 was based on recommendations found in Kokkinakis [44] where the effect of the choice of the Mach number for a channel flow was investigated. From the results, it was noticed that the flow at M=0.2 preserved a steady mean value and the variations of density were below the acceptable maximum incompressible limit of 4%. Therefore, the above acted as an indication that the solution remained physically sensible when a compressible solver is used to simulate incompressible flows. In the same extend, the density variations were also checked for all of the cases under investigation in this thesis. It was found that they remained at approximately 3% for all cases verifying the right choice of Mach number.

Fully periodic boundary conditions were imposed along the streamwise and the spanwise directions simulating infinite building arrays whilst the upper boundary was set to symmetry. Symmetry condition is an artificial condition that differs from the flow in the boundary layer. However, this has no effect on the results since the main area of interest in this thesis is the vicinity of the roughness elements and it was shown in previous studies [87] that flow above the elements remains almost undisturbed. The lower boundary of the domain was considered wall, as well as the faces of the roughness elements, thus the no slip condition was chosen. When fully periodic boundary conditions are imposed to the N-S, a constant pressure gradient or mass flux has to be added as a forcing term. In Xie and Castro [87], it was concluded that both methods provide nearly identical results hence choosing a fixed pressure gradient as a driving force was considered a valid method. The derivation of the constant pressure gradient was obtained by

$$\frac{\partial p}{\partial x} = \frac{\rho u_\tau^2}{L_y} \,, \tag{2.8.1}$$

where L_y is the height of the computational domain and u_τ is the total wall friction

velocity extracted from the definition of roughness Reynolds number

$$Re_\tau = \frac{u_\tau h}{\nu} \,, \tag{2.8.2}$$

where h is the height of the cube and ν is the kinematic viscosity of the fluid.

Non-dimensionalisation of the pressure gradient was essential in order to be implemented in CNS3D. Although M does not correspond to the experimental free stream conditions, the solver preserves the same flow conditions (CNS3D simulates the same Reynolds number as in the experiment) by adapting the viscosity through Sutherland's Law. Therefore, the non dimensional experimental pressure gradient should be equal to the non dimensional numerical one. Non-dimensionalisation of the pressure gradient using the reference values of the wind tunnel experiment yields

$$\frac{\partial p^*}{\partial x^*} = \frac{h}{\rho u^2}\frac{\partial p}{\partial x} \,, \tag{2.8.3}$$

where $\frac{\partial p^*}{\partial x^*}$ denotes the non-dimensional pressure gradient, ρ is the density, h is the height of the cube and finally u is the free stream velocity.

All flow parameters and dimensions presented from onwards are non-dimensionalised unless it is stated differently.

2.8.2 Flow Statistics

In order to be able to quantify the flow dynamics a number of flow indicators were calculated in conjuction with the main flow variables.

Mean Velocities and Turbulence Stresses

Mean profiles of all velocity components were obtained at specific locations indicated in the experiments. These locations refer to constant streamwise and lateral coordinates and the profiles were extracted from all the available grid points along the vertical dimension. Additional flow characteristics such as fluctuating velocities and Reynolds stresses were calculated at the specific locations as well. A more detailed description of the averaging procedure is given for the streamwise velocity component U. The rest of the velocity components are calculated in a similar way. All the mean flow and turbulent statistics are non-dimensional.

Before proceeding, it is important to specify the time window in which the mean statistics were collected. The starting point was specified by identifying the end of the transitional state, using the instantaneous velocity time signal at the locations of interest. A representative example of the signal of the streamwise velocity in the cavity between two cubes is given in Figure 2.3. As seen, the numerical solution starts to develop at

$t_{cur} = 120$; where t_{cur} is the current non-dimensional computational time. Thus, the averaging procedure begins at $t_{start} = t_{cur}$ and all data up to that point is discarded.

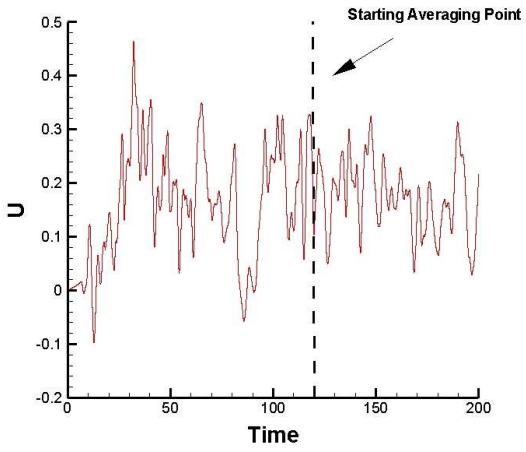

Figure 2.3: Computational starting point.

Mean flow statistics are gathered at every time step along the y dimension at given constant x- and z-coordinates. The averaged velocity profile at the specific location is then extracted from all the available grid points along a line. More precisely, assume a line that consists of n number of grid points so each grid point can be denoted as $p = 1, ..., n$. On each grid point the primitive variables are calculated. In order to proceed with time averaging, variables keeping the summation of the instantaneous values at each grid point for every time step need to be defined. The accumulated variable U is calculated as

$$U_p^{sum} = U_p^{sum-1} + U_p \, \Delta t \tag{2.8.4}$$

where U_p is the instantaneous U velocity at each grid point along the line at each time step, U_p^{sum} is the summation of all instantaneous U velocities at each grid point p over time and finally Δt is the current time step.

The mean velocity over a time window T is defined as

$$u_p = \frac{U_p^{sum}}{T}, \tag{2.8.5}$$

where $T = t_{real} - t_{start}$ and t_{real} is the computational time since the beginning of the simulation.

The fluctuating velocities can now be obtained by

$$u'_p = u_p - U_p. \tag{2.8.6}$$

Finally, the Reynolds stresses are calculated based on the same concept

$$(u'_p)^2_{sum} = (u'_p)^2_{sum-1} + (u'_p)^2 \, \Delta t \tag{2.8.7}$$

$$\overline{u^2}_p = \frac{(u_p')^2_{sum}}{T} \tag{2.8.8}$$

To ensure solution convergence, the velocity profiles were checked at regular time windows. The solution was considered converged when the changes in the magnitude of the profiles were small relative to the increase in computational time. A representative example of a converged solution is given in Figure 2.4. As shown, the difference between the velocity profiles is significantly reduced as the simulation progressed in time and finally reaches the point where the profiles almost collide.

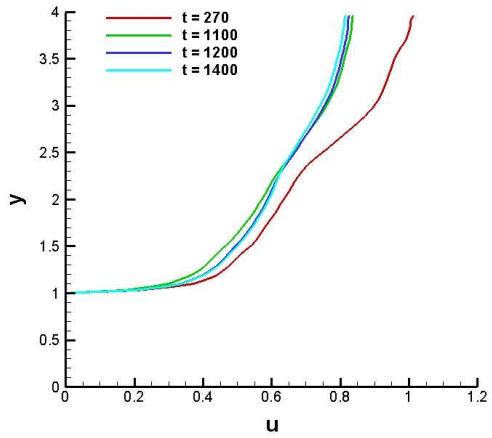

Figure 2.4: Effect of the computational time window.

Kinetic Energy Spectrum

Important information for the existence of fully developed turbulence can be derived from the evolution of eddies in time and space. However, due to the irregular character of turbulence it is not always possible to obtain information from a large area at any time instant. Even individual spatial snapshots can be difficult and expensive.

The solution to the problem was given by the Taylor's hypothesis of frozen turbulence. According to his hypothesis, under certain conditions where the turbulence is assumed stationary and homogeneous, the required time for an eddy to go past a fixed point in space is so small that its change in size is not noticeable. Thus, the turbulence is considered frozen. Therefore, it is expected that the energy spectrum in time will exhibit the same behaviour as the energy spectrum in space. In the sections that follow the distribution of turbulent kinetic energy will be obtained by using the time signal of instantaneous fluctuating velocity components at fixed points is space.

The fluctuating velocity profiles are decomposed using Fourier analysis, where the energy spectrum analysis is based on the wavenumber (k) and the decomposed velocity component. The Fast Fourier Transform (hereafter FFT) used in this thesis is obtained

by splitting the discrete Fourier transform of N points into two discrete Fourier transforms of N/2 points. One is formed from the even-numbered points and the second formed from the odd numbered points. The FFT is described by the following equation

$$F_k = \sum_{j=0}^{\frac{N}{2}-1} e^{\frac{2\pi i k j}{\frac{N}{2}}} f_{2j} + W^k \sum_{j=0}^{\frac{N}{2}-1} e^{\frac{2\pi i k j}{\frac{N}{2}}} f_{2j+1} = F_k^e + W^k F_k^o, \tag{2.8.9}$$

where N is the number of points, $k = 1...N$, F_k^o and F_k^e stand for the k_{th} component of the Fourier transform of N/2 points formed from the odd- and even-numbered points. Finally, W is defined as the complex number

$$W = e^{\frac{2\pi i}{N}}. \tag{2.8.10}$$

Once the Fourier transformation is complete, the turbulent kinetic energy is calculated by multiplying the decomposed velocity with its complex conjugate;

$$E(k) = U(k)U^*(k), \tag{2.8.11}$$

where k is the frequency in the range of $k_{min} = \frac{1}{T}$ and $k_{max} = \frac{1}{2\Delta t}$, T is the sampling time and Δt the sampling interval. Here, $U(k)$ is the decomposed velocity component and $U^*(k)$ is the complex conjugate.

The Q-criterion

Visualisation of the flow topology can be obtained by using the Q-criterion, the second invariant of the velocity gradient, as given by Jeong and Hussain [40].

$$Q = \frac{1}{2}(||\mathbf{\Omega}||^2 - ||\mathbf{S}||^2)\ . \tag{2.8.12}$$

The shear strain rate and vorticity magnitude are defined as

$$||\mathbf{S}||^2 = tr(\mathbf{S}\mathbf{S}^T)\ , \quad and \quad ||\mathbf{\Omega}||^2 = tr(\mathbf{\Omega}\mathbf{\Omega}^T)\ , respectively \tag{2.8.13}$$

where $\mathbf{S}$ is the symmetric component of ∇u defined as

$$S_{i,j} = \frac{1}{2}(\frac{\partial u_i}{\partial x_j} + \frac{\partial u_j}{\partial x_i}) \tag{2.8.14}$$

and $\mathbf{\Omega}$ is the anti-symmetric component of ∇u defined as

$$\Omega_{i,j} = \frac{1}{2}(\frac{\partial u_i}{\partial x_j} - \frac{\partial u_j}{\partial x_i})\ . \tag{2.8.15}$$

This specific method enables the comparison between the numerical schemes in terms of accurate prediction of the smallest possible length scales.

CHAPTER 3

Uniform Height Building Array

IN this chapter, the performance of four high-resolution schemes in the context of Implicit Large Eddy Simulation and their sensitivity to low Mach number features is assessed for flow in an array of four uniform height cubical elements in staggered configuration. The systematic evaluation of the schemes involves direct validation against wind tunnel data available in Cheng and Castro [12], and comparisons with DNS and LES studies conducted by Coceal et al. [14] and Xie and Castro [87], respectively. To facilitate direct comparisons, the numerical grid and settings were based on information extracted from both the experimental and the numerical studies.

3.1 Numerical Details and Settings

Real urban environment is characterised by randomness of building height, shape, alignment and area density. Therefore, it is rather impossible for a wind tunnel model to combine and investigate such a large number of characteristic variables. In Cheng and Castro [12], only the effects of building height and alignment were investigated, whereas the rest of the parameters remained constant. Consequently, the size of a repeating unit was determined in order to permit variability of building height while preventing significant flow development at the same time.

Two cases described in Cheng and Castro [12] were chosen as part of this thesis. The first case deals with flow within a matrix of four uniform height cubical elements in staggered alignment whereas the second case concerns with a more complex case of flow around sixteen buildings of non-uniform heights in a similar arrangement. The latter will be the subject of Chapter 4.

Domain Decomposition

The three dimensional computational domain consists of four repeating units arranged in regular staggered manner. Each unit consists of a one cube with a 25% covering area as shown in Figure 3.1(a).

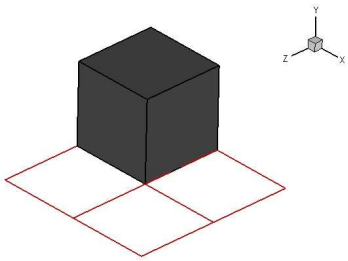

(a) One cube repeating unit.

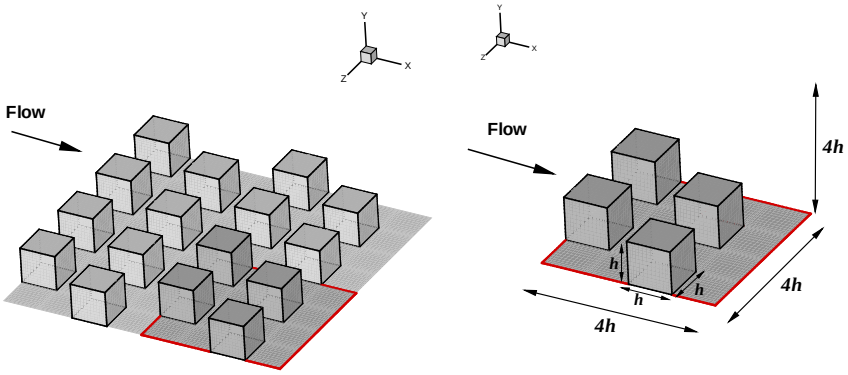

(b) Infinite cube matrix. (c) Computational domain.

Figure 3.1: Three dimensional illustration of the domain.

The size of the domain is L_x x L_y x L_z = 4h x 4h x 4h, where $h = 0.02m$ is the cube height as described in the LES study of Xie and Castro [87]. A representation of the computational domain is given in Figure 3.1(c). The domain appears relative small to be able to capture all the scales of turbulence. However, in the DNS study of Coceal et al. [14], it is stated that the mean velocity and turbulence statistics almost identical to those obtained with larger size domains, apart from the area near the top boundary.

Grid Resolution

The computational domain was meshed using structured multiblock grids of three different resolutions. The first computational mesh consists of approximately 0.2 million cells with 16 x 16 x 16 grid points per cube height (ILES16, coarse grid). The second grid comprises approximately 0.6 million cells with 24 x 24 x 24 grid points per cube height (ILES24, medium grid) whereas the third grid is considerably finer with approximately 1 million cells and 32 x 32 x 32 grid points per cube (ILES32, fine grid), see Figure 3.2. All grids are clustered around the faces of the cubes in order to increase the accuracy in the near wall region. The coarse and fine grids were constructed in reference to the work of Xie and Castro [87], while the medium grid was constructed as an intermediate resolution between the two meshes. A summary of the

grid characteristics is provided in Table 3.1.

Grid	$L_x \times L_y \times L_z$	Grid points per h	y^+
ILES16	$4 \times 4 \times 4$	$16 \times 16 \times 16$	≈ 23
ILES24	$4 \times 4 \times 4$	$24 \times 24 \times 24$	≈ 19
ILES32	$4 \times 4 \times 4$	$32 \times 32 \times 32$	≈ 10

Table 3.1: Summary of ILES grid characteristics.

In Table 3.1, y^+ stands for the distance in wall units of the centre of the first cell from the wall and it is determined using Equation 3.1.1 and 3.1.2

$$y^+ = \frac{u_\tau y}{\nu}, \tag{3.1.1}$$

$$u_\tau = \sqrt{\frac{(\frac{\partial u}{\partial y})}{\nu}}, \tag{3.1.2}$$

where u_τ is the local friction velocity, y is the distance of the first cell from the wall and ν is the kinematic viscosity.

Results obtained using all three grids will be compared against other numerical studies available in the literature using grid resolutions as shown in Table 3.2. By comparing the two tables, two remarks can be made; the coarser grid in ILES has the same grid resolution as the medium grid in LES and the values of y^+ are not similar in both numerical methods. To increase the grid resolution in areas of interest, standard wall models were used in LES whereas, despite the high values of y^+, no turbulent wall model was included in ILES. The decision was based on a previous study conducted by Thornber [76] in which the flow within an open cavity was simulated using the 5th order MUSCL scheme combined with the Low Mach Correction Treatment. The values of y^+ were ranging between 20 and 55 and no wall model was used either. Although the boundary layer was considered greatly under resolved, the mean and turbulent statistics were in very good agreement with the experimental data and all the important flow physics were accurately predicted.

Grid	$L_x \times L_y \times L_z$	Grid points per h	y^+
LES8	$4 \times 4 \times 4$	$8 \times 8 \times 8$	≈ 12
LES16	$4 \times 4 \times 4$	$16 \times 16 \times 16$	≈ 9
LES32	$4 \times 4 \times 4$	$32 \times 32 \times 32$	≈ 6
DNS64	$4 \times 4 \times 4$	$64 \times 64 \times 64$	

Table 3.2: Summary of the grid resolutions of referenced numerical studies [87], [14].

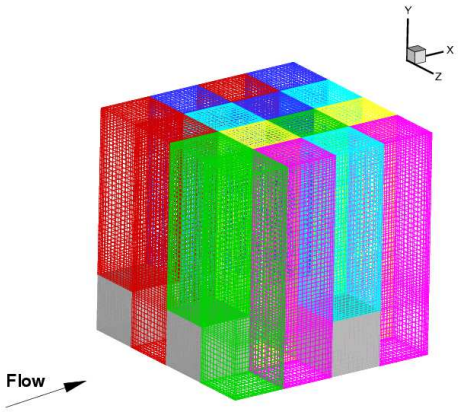

(a) Block structured grid.

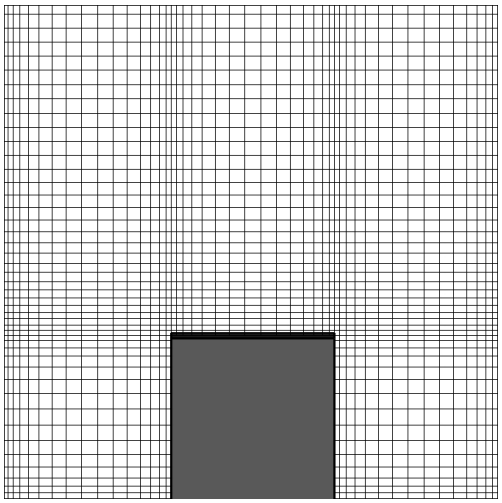

(b) Coarse grid.

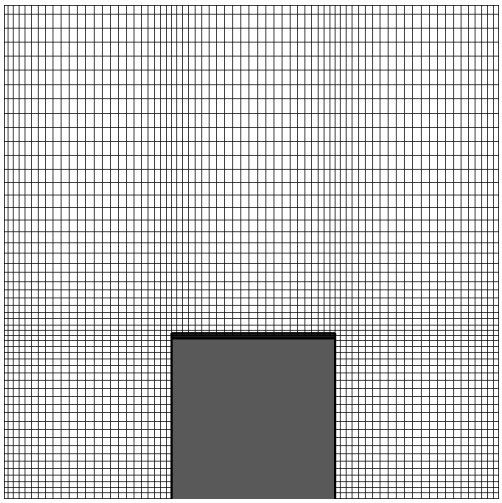

(c) Medium grid.

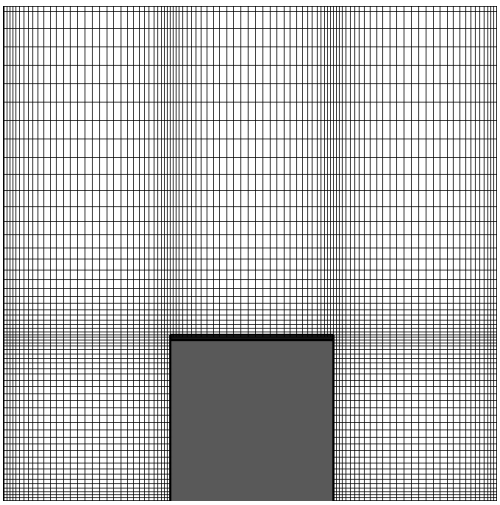

(d) Fine grid.

Figure 3.2: Computational grids.

Numerical Settings

As mentioned in Chapter 2, fully periodic boundary conditions were imposed along the x- and the z- direction for simulating an infinite cubical array as in Figure 3.1(b). The top boundary (along the y- direction) was set to symmetry. The lower boundary of the domain was considered as wall, as well as the faces of the cubes, thus the no-slip condition was chosen. A constant pressure gradient of -1.59 Pam^{-1} was imposed as described in 2.8.1.

The case is simulated at a Reynold number of Re=5000 based on free stream velocity and cube height.

As part of this thesis, the second-order MUSCL scheme combined with the Van Albada limiter, the fifth-order MUSCL scheme, the fifth- and the ninth-order WENO scheme have been employed. In the following sections, the above schemes will be referred to as 2ndVA, 5thM, 5thWN and 9thWN, respectively. During the simulations, the schemes were used either in their original form or including the Low Mach Correction Treatment.

Finally, time integration was performed by the third-order TVD Runge-Kutta scheme. The value of CFL was set to 0.5 in all simulations apart from the cases investigating effects of the computational time step where its value was 0.3.

3.2 Flow topology

A three dimensional impression of the flow field is given in Figure 3.3. Volume lines coloured with velocity magnitude were used for the flow visualisation with the particle lines starting from XY planes attached to the faces of the cubes. When the flow enters the computational domain, it gets redirected by the presence of the buildings. As a result, strong vortical structures are created at the side faces of the cubes, revealing the turbulent character of the flow in the cavity between the buildings. The presence of vortices close to the end of the computational domain, indicates a near wall region ahead which verifies the periodic boundary conditions imposed along the spanwise direction.

Information regarding the structure of the flow field was also derived by means of velocity contours and vectors at constant z and y positions as shown in Figure 3.4 and Figure 3.5, respectively. The results presented here were obtained using the 5thM scheme on the ILES16 computational mesh.

In Figure 3.4(a), the flow field is illustrated using velocity contours. As expected, the near wall region is dominated by low velocities or zero on the wall, whereas the velocity magnitude increases as the flow approaches the top boundary. By using velocity vectors in all planes, the vortical structures become visible in the vicinity of the cubes whilst above the obstacles the flow seems to be nearly undistorted. A typical flow pattern around an isolated obstacle [53] consists of the front recirculation region, side

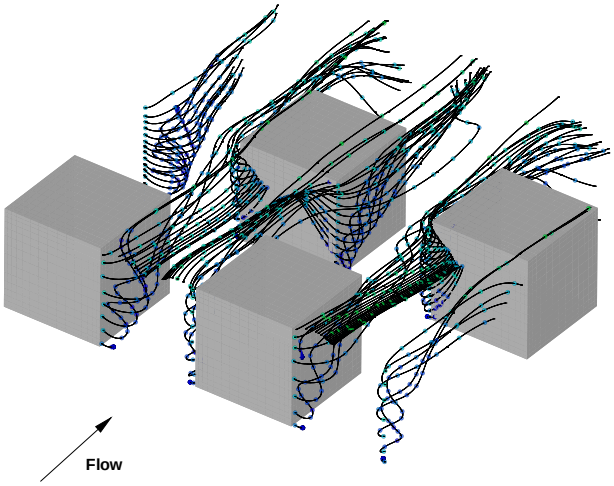

(a) Side view

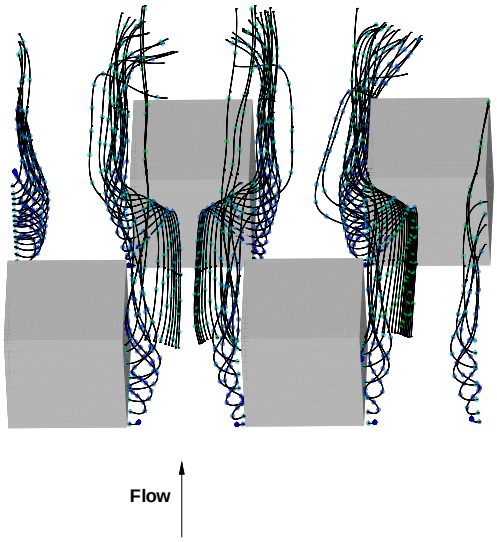

(b) View from the front of the domain

Figure 3.3: Three dimensional impression of the flow.

recirculation zones, detached wake and a separation and reattachment on the top of the building leading to a vortical structure above the roof. As seen in Figures 3.4(b) - 3.4(e), as soon as the oncoming flow strikes the windward edge, it separates and moves over the obstacle resulting into a small circulation area very close to the leading edge. Another important flow structure is the formulation of an upstream vortex at the vicinity of the frontal face of each cube.

Similarly, the recirculation areas at the sides and the wake of the cubes have been identified in Figure 3.5 in terms of velocity contours and vectors. Due to flow separation

at the upstream face of the cube, a complex vortical structure is formulated around the sides and wake. The flow is redirected along the left and right walls and wraps around each cube until it starts weakening further downstream. Finally, the presence of two vortices in very close proximity to the leeward face of the cube indicates the existence of legs of the arc-type vortex.

As described in 2.8.2, the Q-criterion of Jeong and Hussain [40] can be used as an additional means of flow visualisation. Instantaneous turbulent scales, predicted with the four numerical schemes on identical grids, can be seen in Figure 3.6 and Figure 3.7. Depending on the scheme's order of accuracy, different range of length scales was captured. More precisely, differences in the range of scales are seen between schemes of the same family. The fifth-order MUSCL (5thM) resolves smaller scales than the second-order MUSCL (2ndVA), whilst in the same manner the ninth-order WENO (9thWN) scheme predicts a wider range of scales than fifth-order WENO (5thWN). The clearest distinction is shown when comparing the 2ndVA and the 9thWN scheme.

Based on the above observations regarding the flow field within the cube array, it can be stated that the flow characteristics resemble those seen in the fundamental case of flow around a single cube in Martinuzzi and Tropea [53]; a promising indication of the capabilities of ILES in accurately predicting environmental flows.

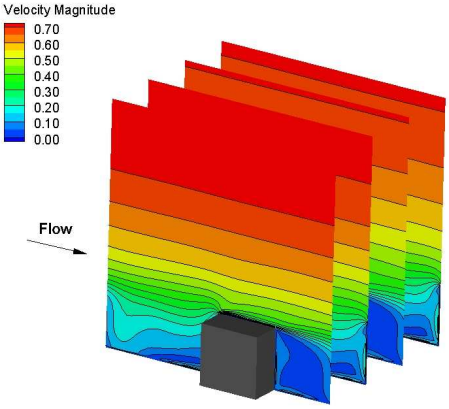

(a) Location of the XY slices

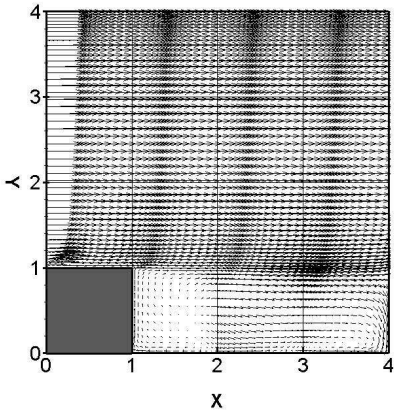

(b) Slice at z=0.5

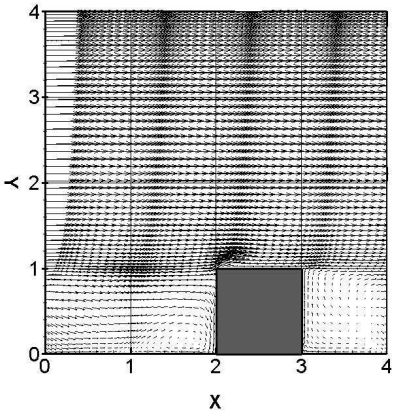

(c) Slice at z=1.5

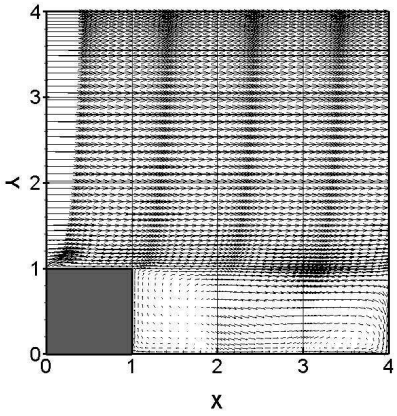

(d) Slice at z=2.5

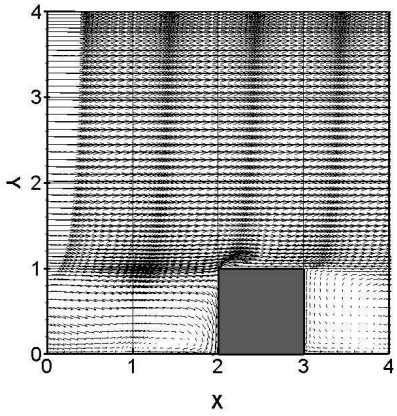

(e) Slice at z=3.5

Figure 3.4: Time averaged velocity contours and vectors in XY planes.

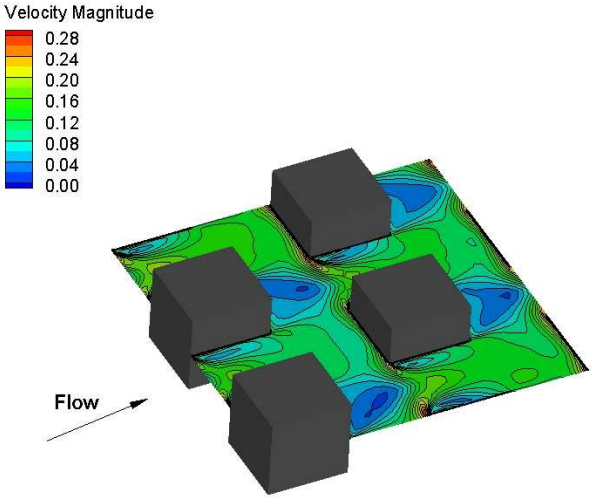

(a) Location of the XZ slice

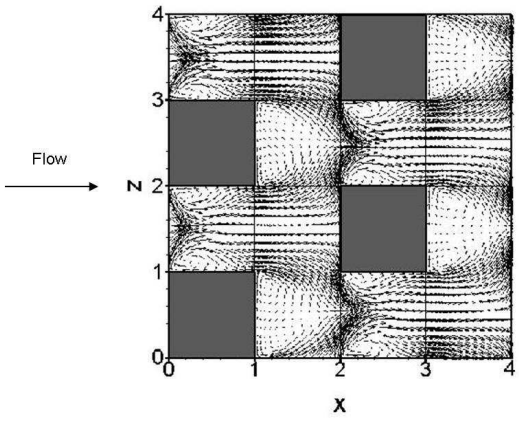

(b) Slice at y=0.5

Figure 3.5: Time averaged velocity contours and vectors at y=0.5.

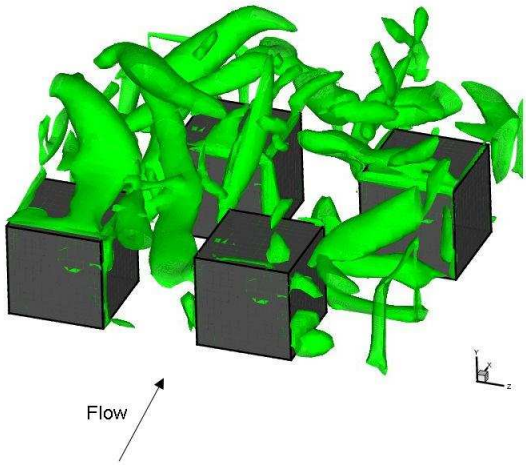

(a) 2nd Order MUSCL with Van Albada limiter

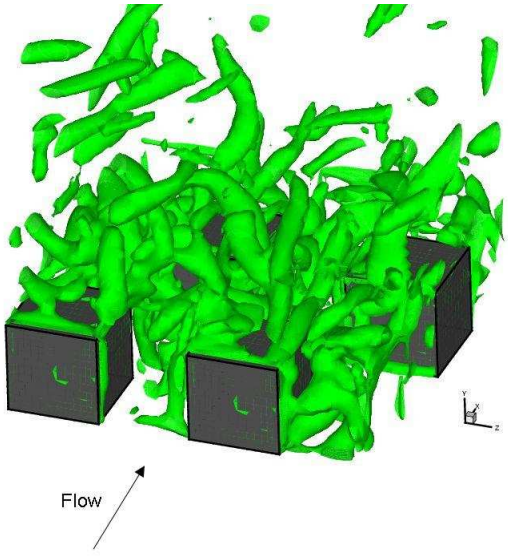

(b) 5th Order MUSCL

Figure 3.6: Q-criterion in MUSCL schemes - Isosurfaces of instantaneous Q=0.3.

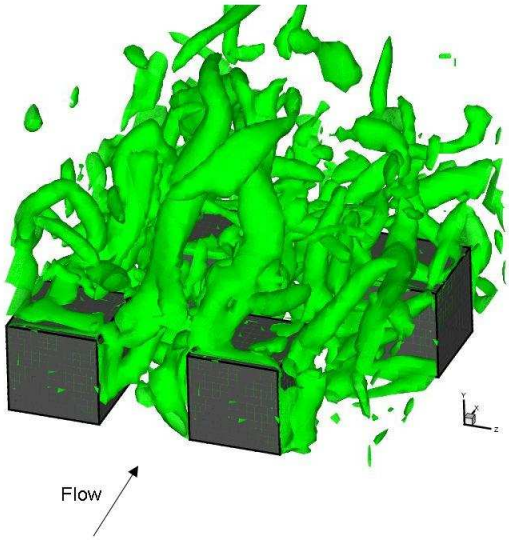

(a) 5th Order WENO

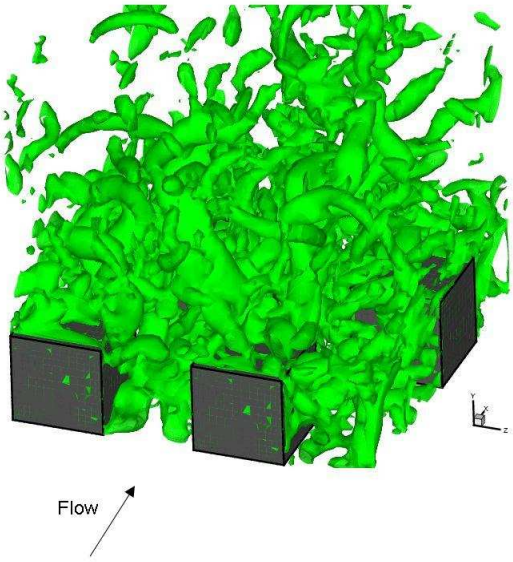

(b) 9th Order WENO

Figure 3.7: Q-criterion in WENO schemes - Isosurfaces of instantaneous Q=0.3.

3.3 Results

In order to evaluate the performance and applicability of ILES in flows characterised by complex turbulent features, the results are validated against available experimental data [12]. Additional comparisons with existing numerical studies will also be included. The effects of the choice of grid resolution, numerical scheme, Low Mach Correction Treatment and computational time step on the numerical solution will be the main focus of this investigation.

All quantities presented hereafter are non dimensionalised with the reference variables described in Chapter 2, unless it is stated differently. The statistics of the flow field have been averaged over a sufficient time window for the larger scales to converge.

3.3.1 Grid Resolution Dependency

The sensitivity of the results on the spatial discretisation was assessed by comparing results obtained on the three grids (as described in 3.1) against experimental data. The comparisons in terms of vertical profiles of mean streamwise velocity and turbulent intensities were made at four distinct locations above and within the cube cavity as shown in Figure 3.8. In Castro et al. [11], it is stated that despite the fact that the four locations were originally chosen to represent the different regions of the flow, purely based on intuition, it has been proven that they are indeed representative of the specific type of the geometry. In the comparisons that follow, results were obtained using the 5thM scheme coupled with the Low Mach Correction Treatment.

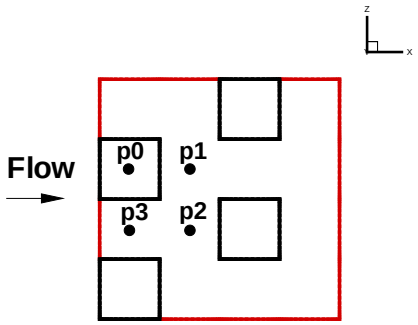

Figure 3.8: Highlighted locations of comparison.

Figure 3.9 shows comparisons between the ILES data obtained with three different grid resolutions and experimental data. From the results, it is evident that solutions obtained on either the ILES16 or ILES24 grid exhibit a very good agreement with the experiment for most of the locations. However, a clear difference in magnitude is noticeable when the solution is obtained on the finest grid. The extracted vertical

velocity profiles indicate that the numerical simulation leads to an overpredicted free stream velocity. This observation was verified further by calculating the mass flow rate on the coarse and the finest grid by integrating over the same plane of the domain. As expected, the mass flow rate on the finest grid was overestimated, with the discrepancy reaching $\approx$ 16%. Although all three cases have been set up in the same manner, it seems that different flow conditions are developing when the finest grid is used. One possible reason could be that the combination of increased grid resolution and high order spatial discretisation scheme, coupled with Low Mach Correction Treatment, does not produce adequate numerical dissipation [44].

The picture changes in Figure 3.10. Comparisons in terms of stresses show that the peaks of the shear layer are well captured with all three meshes. However, the best agreement with the LDA data is seen with the finest grid in the wake and in front of the cube. The ILES16 and ILES24 results seem to predict the correct shape of the stresses but they lack in magnitude independent of the location. The stresses appear overpredicted in the cavity between the two cubes when the ILES32 is used. This specific behaviour can be explained in the same way as stated immediately above. When the solution is lacking dissipation, then the turbulent scales are over resolved. The effect of the imposed symmetry condition at the top boundary is also illustrated in Figure 3.10. As discussed in Section 2.8.1, the symmetry condition is an artificial condition that does not correspond to the real urban environment where there is no wall as an upper boundary. This explains, the sudden decrease of the normal stress (V_{rms} stress) as the flow approaches the top boundary. Finally, it is believed that the poor grid resolution near the upper boundary of the computational domain (the grid has been clustered only around the faces of the cubes) is responsible for the kinked U and U_{rms} profiles at the specific area.

Based on the above remarks, it can be stated that when high-order schemes are coupled with Low Mach Correction Treatment, it could be possible to obtain a more accurate flow estimation on a coarser grid. Therefore, it was decided to present comparisons on the ILES16 computational mesh in order to investigate whether indeed Low Mach Correction treatment leads to accurate results while reducing the numerical requirements at the same time.

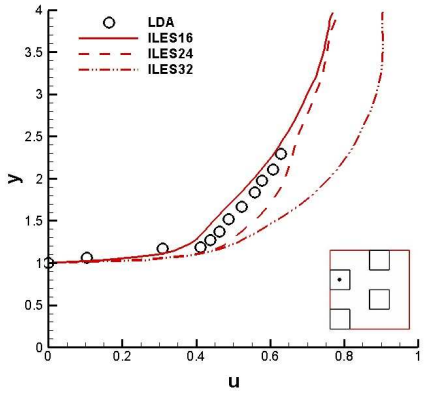

(a) LDA vs 5thM scheme at location p0

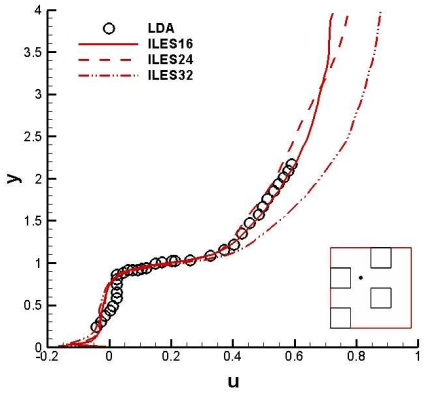

(b) LDA vs 5thM scheme at location p1

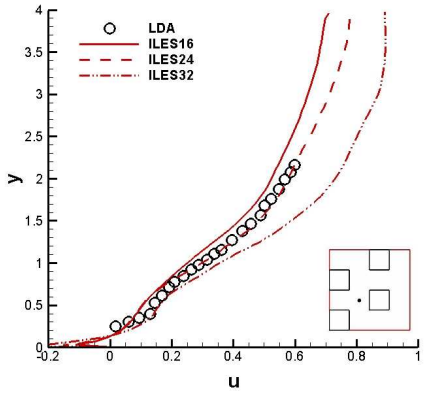

(c) LDA vs 5thM scheme at location p2

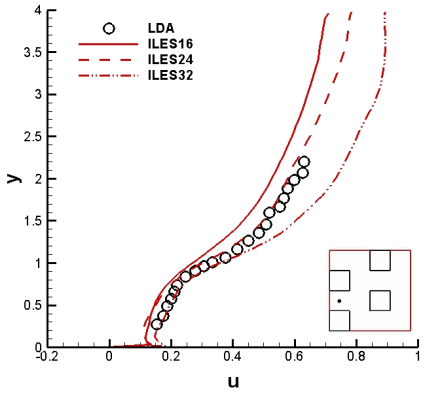

(d) LDA vs 5thM scheme at location p3

Figure 3.9: Grid resolution dependency of mean velocity profiles.

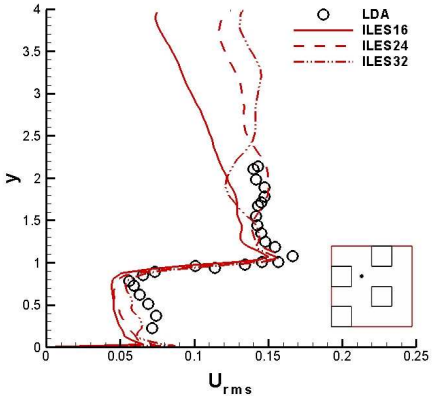

(a) U_{rms} at location p1

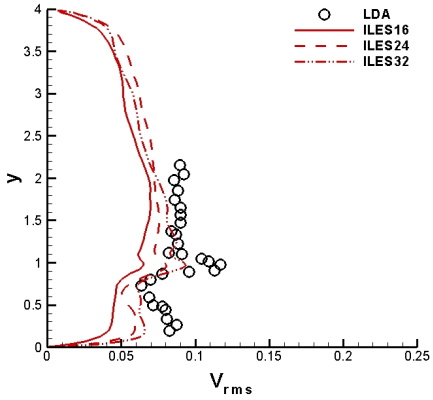

(b) V_{rms} at location p1

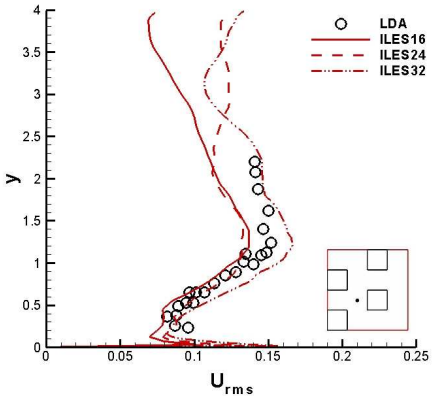

(c) U_{rms} at location p2

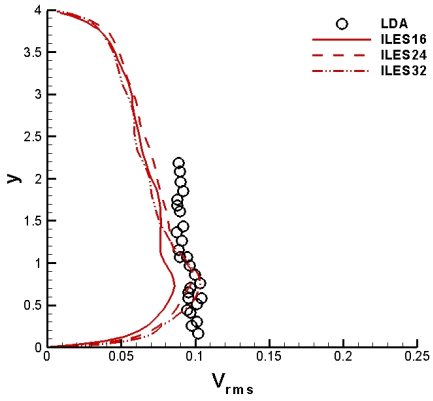

(d) V_{rms} at location p2

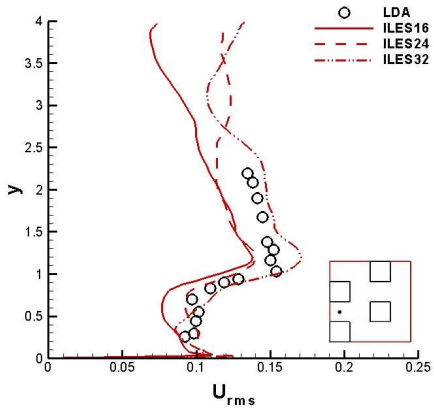

(e) U_{rms} at location p3

Figure 3.10: Grid resolution dependency of mean stress profiles.

3.3.2 Numerical Scheme Dependency

The effects of the numerical schemes on the solution will be presented in this part of the thesis. The four schemes in their original form will be compared against experimental and numerical data using vertical profiles of mean statistics at the same four locations as described in the Section 3.3.1. For simplicity, the Laser Doppler Anemometry experimental data will be referred to as LDA data in the comparisons that follow.

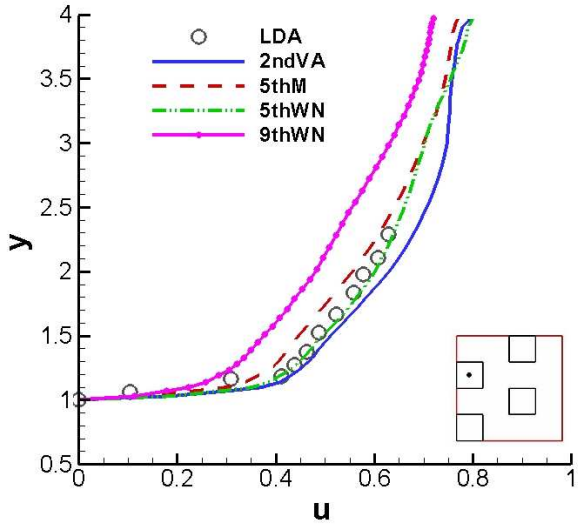

(a) Location p0

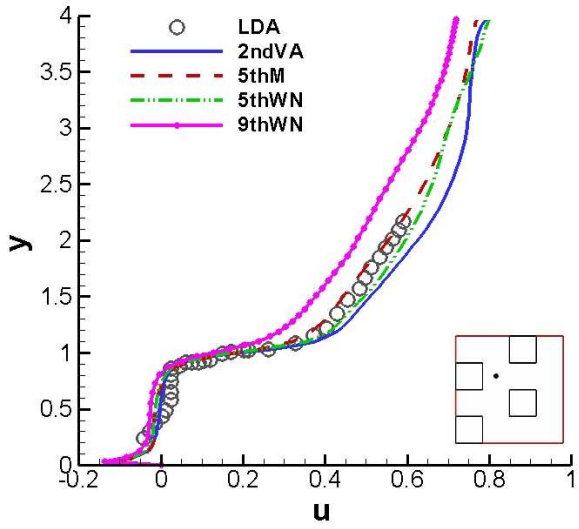

(b) Location p1

Figure 3.11: Scheme dependency investigation at locations p0 and p1.

Comparisons above the height of the cube are given in Figure 3.11(a). The 5thM and

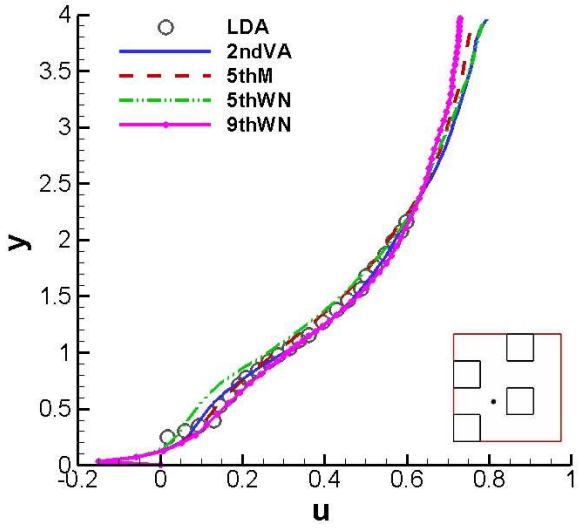

(a) Location p2

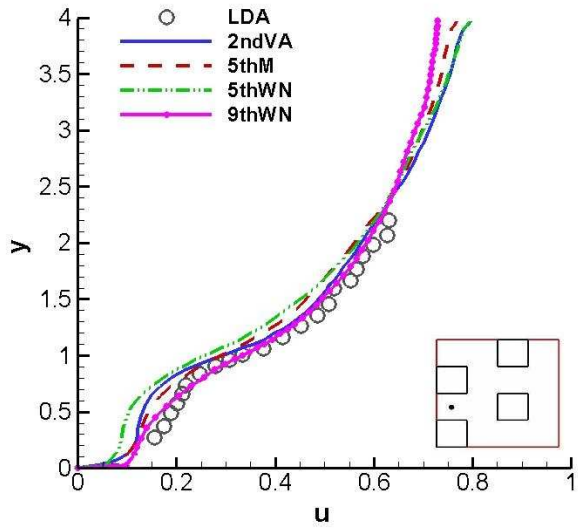

(b) Location p3

Figure 3.12: Scheme dependency investigation at locations p2 and p3.

the 5thWN scheme show very good agreement with the LDA data, although slight undeprediction and overprediction are noticed, respectively. The two schemes seem to share approximately the same value at the top boundary. The 2ndVA scheme appears to be less accurate but still close to the experiment whereas the 9thWN is able to predict the shape of the velocity profile. However, it shows a clear difference in magnitude.

Comparisons in the wake of the cube are illustrated in Figure 3.11(b). All schemes exhibit a similar behaviour below the height of the cube where the density of the grid is increased. However, the picture changes above the cube, with the schemes acting the

same way as in Figure 3.11(a). The LDA data continues to lie between the 5thM and 5thWN scheme. The 2ndVA overpredicts the velocity magnitude up to 3.5h (where h is the height of the cube), whereas after that point, the velocity profile is in between the profiles of 5thM and 5thWN scheme. The 9thWN scheme continues to be lacking in magnitude.

Velocity profiles in the cavity between the two cubes are given in Figure 3.12(b). Since the 5thWN scheme appears to possess slightly more negative values than the 5thM in Figure 3.11(b), as the flow develops, the 5thM velocity profile should be higher than the 5thWN. This is verified in Figure 3.12(b). Also, the 2ndVA scheme gives a higher velocity profile than the the 5thWN. Regarding the 9thWN, it can be said that this specific scheme develops smoother than the rest of the schemes because of the smaller velocity difference in the shear layer, shown in Figure 3.11(a) and Figure 3.11(b).

Finally, all profiles have smoothed out as the flow develops and reaches location p3 in Figure 3.12(a). The specific location can be considered to be the end of the domain since periodic boundary conditions are imposed. By summing up all the observations from all the previous locations, it can be stated that indeed that 9thWN had a quicker transition to a smoother velocity profile. Despite the fact that, among all schemes, the 2ndVA had to overcome a higher velocity gradient, it managed to produce results with very good agreement with the LDA data. The difference between the 5thM and 5thWN in location p3 seem to be bridged, with the profiles being now almost identical above the height of the cube.

Based on the comparisons presented, it can be concluded that the behaviour of the schemes depends on the location. At location p0 where the flow starts to develop within the computational domain, the difference among the schemes is more obvious. However, as the flow develops and moves towards the end of the domain, the profiles seem to converge and only small differences in magnitude are seen. Depending on the velocity gradient that has to be overcome at the shear layer, the schemes reach the smooth velocity profile in a different manner. Nonetheless, the ILES results are comparable to the LDA data at all four locations.

3.3.3 Low Mach Correction Treatment Dependency

The aim of this section is to establish whether there is any effect on the solution when the Low Mach Correction Treatment is chosen as means of minimising any excessive dissipation. A same procedure will be followed as in the previous section, with the schemes incorporating the Low Mach Correction Treatment being now compared against the original schemes and LDA data. In the comparisons that follow, the suffix 'LM' will be added to the schemes names when the Low Mach Correction Treatment is used.

Comparisons over the top of the cube are presented in Figure 3.13. Very good agreement with the LDA data is seen when the mean velocity profile is produced using the 2ndVA scheme combined with the Low Mach Correction Treatment. Same shape of velocity profile is predicted with the 2ndVA scheme in its original form, but the velocity magnitude is higher. However, both cases seem to converge to the same mean velocity at the top boundary. Regarding the 5thM scheme, different shapes of profiles are seen between the original form of the scheme and its modified counterpart. Specifically, although the two profiles are almost identical near the roof of the cube, they start to diverge slightly until they cross each other and finally obtain dissimilar values at the upper boundary. No effect is seen in the case of the 5thWN scheme until the flow reaches the height of approximately 2.5 times the height of the cube. In a same way as in the case of 5thM, crossing velocity profiles are seen, but they tend to a common value at the end of the domain. Finally, a clear divergence in the velocity profiles is shown in the case of the 9thWN. Among all profiles, the 9thWN seems the most strongly affected when coupled with the Low Mach Correction Treatment. As an overall conclusion, regarding position p0, it can be said that three out of the four schemes appear to produce better results when using the Low Mach Correction Treatment.

Mean velocity profiles in the wake of the cube are given in Figure 3.14. Below the height of the cube where the computational grid is clustered for increased accuracy, all schemes even the 9thWN scheme demonstrate similar results to their counterparts. The best comparison with the experimental data is the 2ndVA scheme in both forms. As the flow develops further, the velocity profiles exhibit similar behaviour to the one in Figure 3.13. The gap remains between the two profiles in the case of the 9thWN. However, it is slightly reduced.

Comparisons at location p2 are illustrated in Figure 3.15. As the profiles approach a smoother shape, even the slightest differences between the 2ndVA and 5thWN with their counterparts are eliminated, whereas the 5thWN and 9thWN schemes seem to predict the streamwise velocity accurately without the need of Low Mach Correction Treatment. On one hand, the Low Mach Correction Treatment leads to an underpredicted velocity profile when applied to the 5thM scheme. On the other hand, the velocity gets overpredicted when the 9thWN scheme is used.

Comparisons in the cavity between the two cubes are illustrated in Figure 3.16. The effect of the Low Mach Correction seems reduced for the 2ndVA scheme in comparison to the profiles at locations p0 and p1. Better results are obtained with the 2ndVA

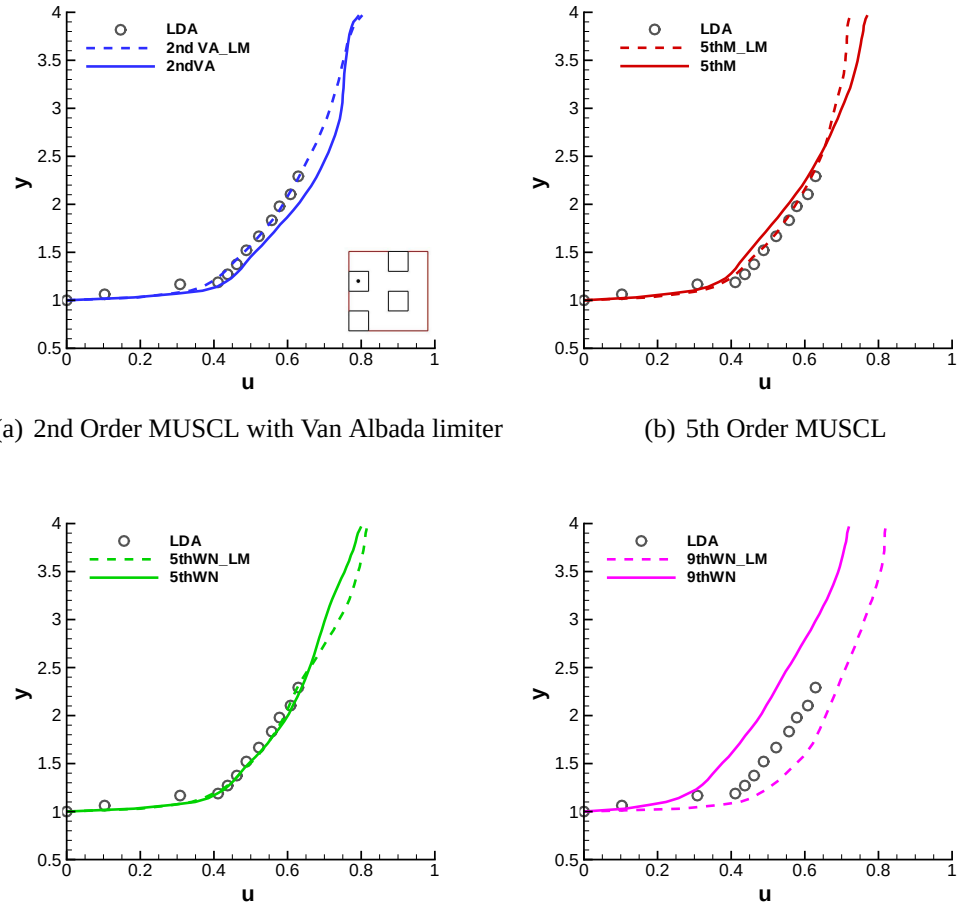

(a) 2nd Order MUSCL with Van Albada limiter

(b) 5th Order MUSCL

(c) 5th Order WENO

(d) 9th Order WENO

Figure 3.13: Low Mach Correction effect at location p0.

when the treatment is used. Nonetheless, the differences in the velocity magnitudes can be considered negligible. Unlike locations p0 and p1, same shapes of the velocity profiles are seen at location p3 when the 5thM scheme is used. The original formulation of the scheme provides a higher velocity magnitude that compares better with the experimental data. The 5thWN scheme remains less affected with almost identical velocity profiles. Finally, the 9thWN profiles have come closer than at locations p0 and p1. However, the profiles do not share the same shape since they cross each other at approximately 1.5 times the height of the cube.

Figure 3.17 shows comparisons of Reynolds stresses behind the cube. All schemes in their original formulation seem to capture the peaks of the stresses in the shear layer with reasonable accuracy. As the order of the scheme increases, the turbulent statistics become more comparable with the LDA data. Hence, the 9thWN scheme produces a more accurate prediction of the Reynolds stresses than the 2ndVA. Although the mean velocity profiles, calculated with 5thWN and 2ndVA, appear unaffected by the Low Mach Correction Treatment, a dependency is noticed here with the stresses being

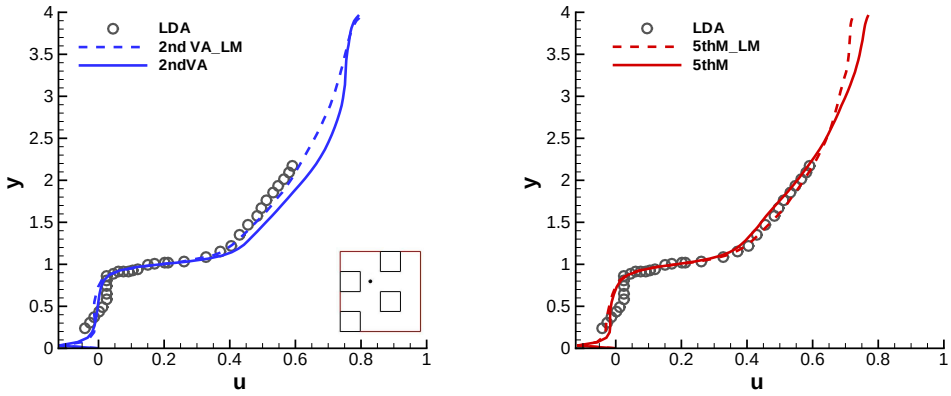

(a) 2nd Order MUSCL with Van Albada limiter

(b) 5th Order MUSCL

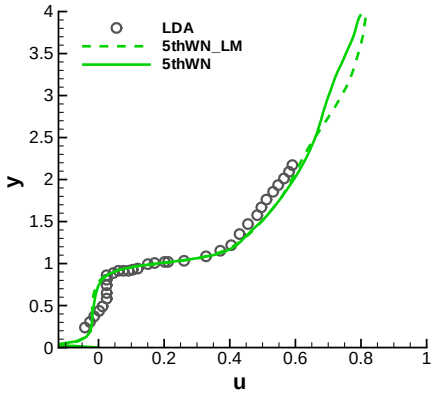

(c) 5th Order WENO

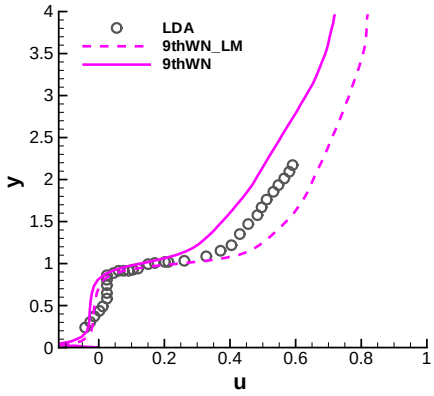

(d) 9th Order WENO

Figure 3.14: Low Mach Correction effect at location p1.

underpredicted above the height of the cube.

Reynolds stresses in front of a cube are presented in Figure 3.18. As at location p1, the 9thWN scheme seems to follow the shape of the streamwise Reynolds stresses closely. The 5thWN scheme, in both forms, appears comparable to the LDA results as well. However, the stresses are underpredicted above the height of the cube. Finally, the 2ndVA scheme produces better turbulent statistics than its counterpart. As at location p1, the Reynolds stresses calculated with the 5thM are lacking in magnitude above the height of the cube.

Finally, comparisons in terms of turbulent statistics are given in Figure 3.19. The 5thM scheme continues to produce less accurate results in terms of Reynolds stresses. The effect of the Low Mach Correction Treatment is more evident in the cases of the 2ndVA and 9thWN, especially above the cube. Nonetheless, both schemes in their original form provide better prediction of the stresses. However, below the cube, the 9thWN_LM resembles the 2ndVA profile and vice versa. Regarding the 5thWN

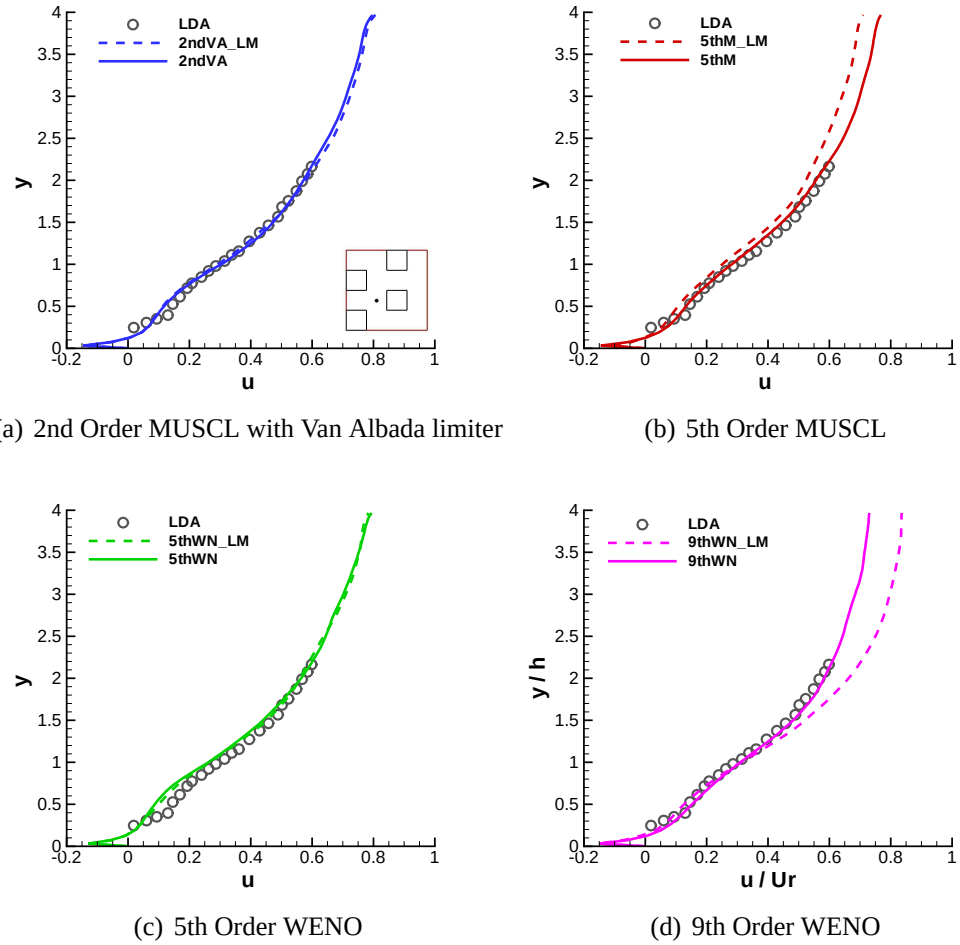

(a) 2nd Order MUSCL with Van Albada limiter

(b) 5th Order MUSCL

(c) 5th Order WENO

(d) 9th Order WENO

Figure 3.15: Low Mach Correction effect at location p2.

scheme, the stress profiles are alike up to middle of the computational domain and in good agreement with the experiment. Further comparisons of Reynolds stresses regarding the above locations in terms of V_{rms} and W_{rms} can be found in Appendix B.

By taking into account all the comparisons presented so far, some initial conclusions can be drawn regarding the effect of the Low Mach Correction Treatment. Almost all schemes appear to be able to predict the shape of the vertical velocity profiles and the Reynolds stresses of all locations with or without the Low Mach Correction Treatment being employed. Furthermore, the least affected scheme, exhibiting very good agreement between experimental and numerical data, is the 5thWN followed by the 2ndVA. The 5thM scheme seems able to predict to a reasonable extent the mean flow and turbulent statistics, but its performance is affected mainly by the location of the comparison point. The most affected scheme is the 9thWN scheme whose performance is actually reduced when the Low Mach Correction Treatment is chosen.

The reason behind the overprediction of the velocity profile lies in the fact that the 9thWN scheme (using a five node computational stencil) reduces the numerical dissi-

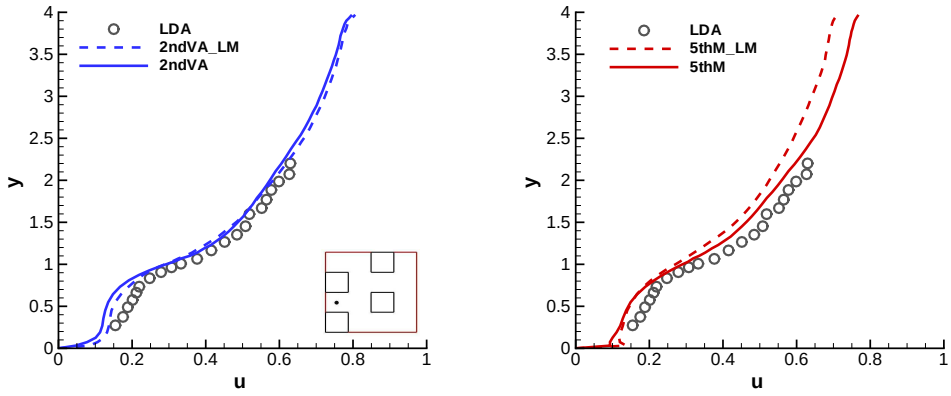

(a) 2nd Order MUSCL with Van Albada limiter

(b) 5th Order MUSCL

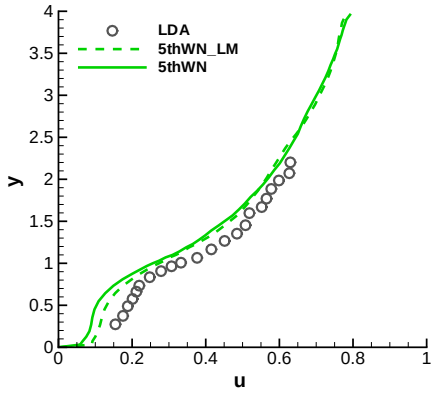

(c) 5th Order WENO

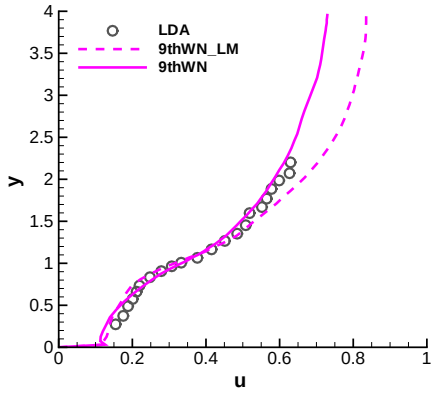

(d) 9th Order WENO

Figure 3.16: Low Mach Correction effect at location p3.

pation via higher order of spatial discretisation. Hence, in conjunction with the Low Mach Correction Treatment, the scheme becomes unable to produce adequate dissipation and eventually results into an overwhelmed solution with unphysical behaviour as also seen in the work of Kokkinakis [44]. It should be noted that the Low Mach Correction Treatment was mainly proposed for the 5thM scheme [78]. However, the turbulent statistics overall appear sensitive to the choice of Low Mach Correction Treatment with the 9thWN scheme providing the best comparison with LDA data.

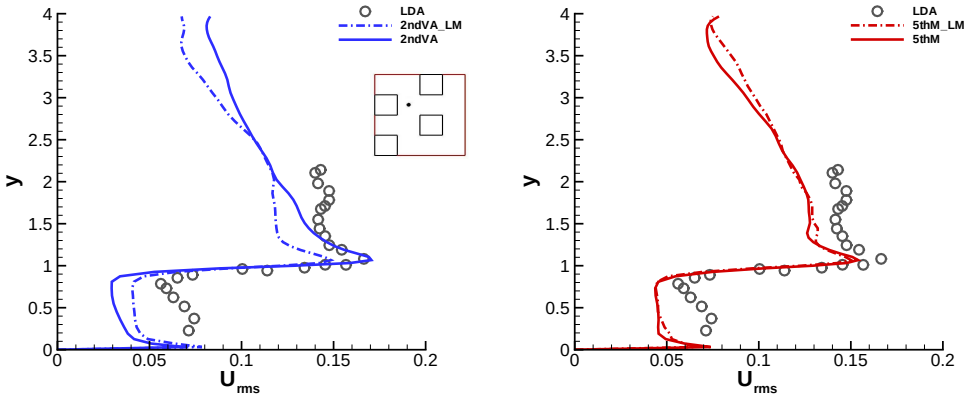

(a) 2nd Order MUSCL with Van Albada limiter (b) 5th Order MUSCL

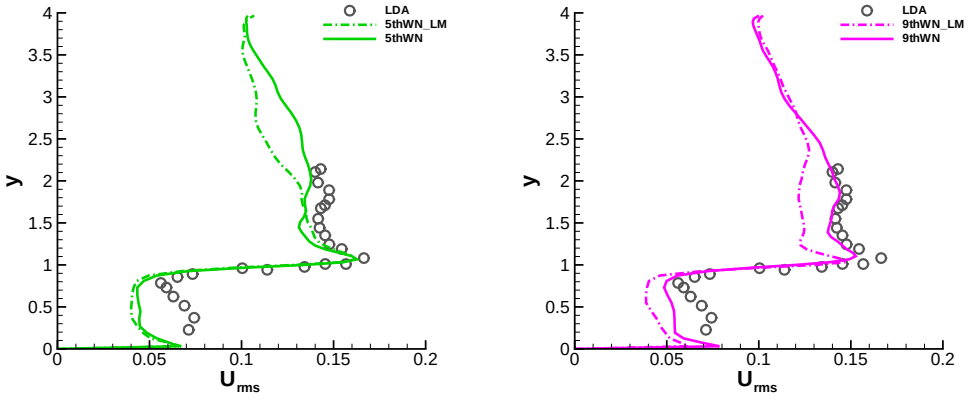

(c) 5th Order WENO (d) 9th Order WENO

Figure 3.17: Reynolds stresses at location p1.

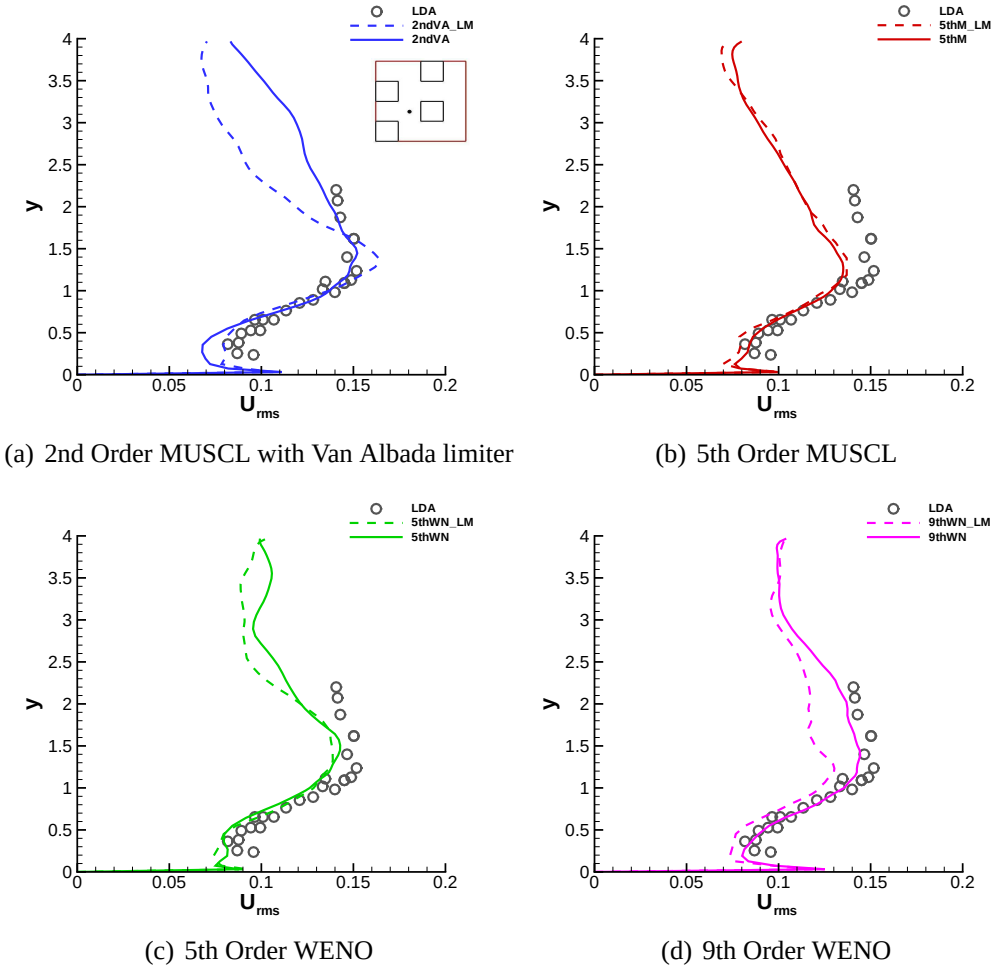

(a) 2nd Order MUSCL with Van Albada limiter

(b) 5th Order MUSCL

(c) 5th Order WENO

(d) 9th Order WENO

Figure 3.18: Reynolds stresses at location p2.

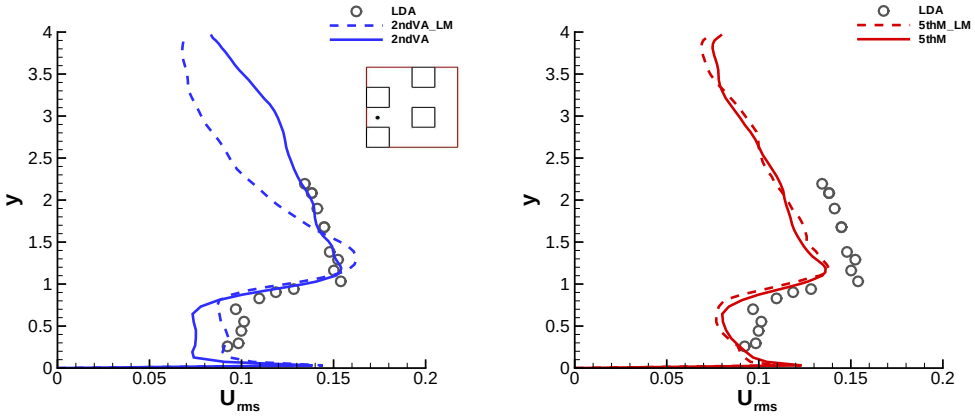

(a) 2nd Order MUSCL with Van Albada limiter (b) 5th Order MUSCL

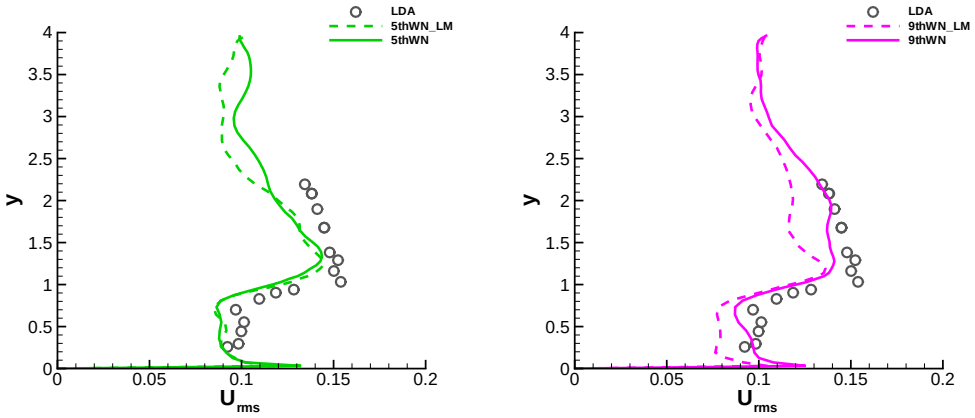

(c) 5th Order WENO (d) 9th Order WENO

Figure 3.19: Reynolds stresses at location p3.

Comparison with DNS data

Comparisons between the available DNS study of Coceal et al. [14] and the ILES simulations (with and without the Low Mach Correction Treatment) will be presented in this section of the thesis. The size of the computational domain and the arrangement of the cubes are identical for both numerical approaches. However, the DNS results were produced on a much finer computational grid (64x64x64 grid points per cube height) than the ILES simulations (16x16x16 grid points per cube height), see Table 3.1 and Table 3.2. Comparisons in terms of mean velocity profiles between DNS and ILES16 will follow.

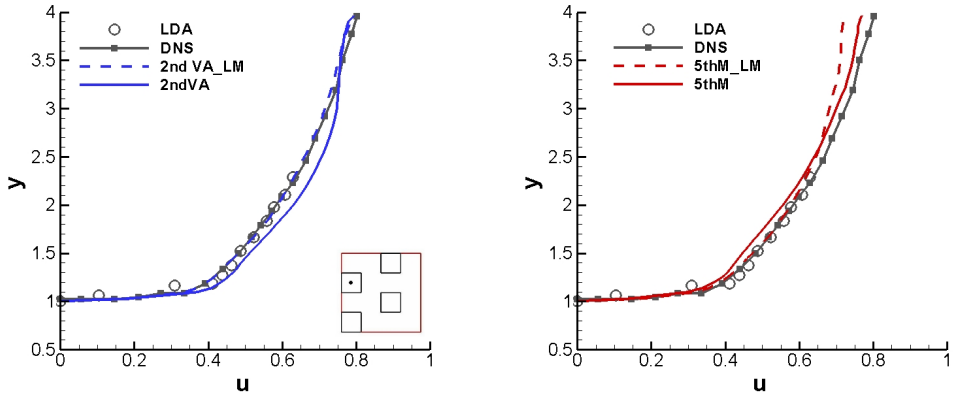

(a) 2nd Order MUSCL with Van Albada limiter

(b) 5th Order MUSCL

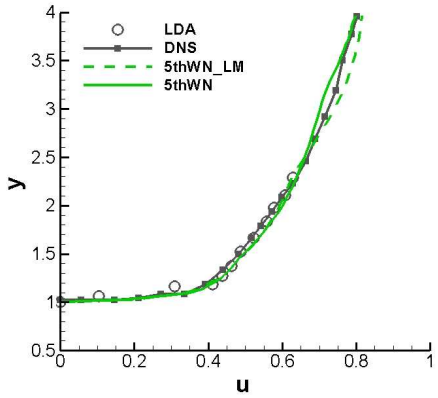

(c) 5th Order WENO

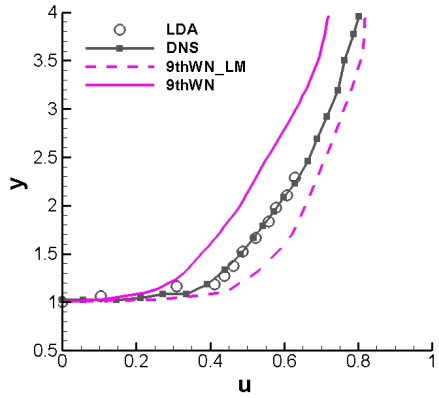

(d) 9th Order WENO

Figure 3.20: ILES against DNS data at location p0.

At location p0, the best agreement between DNS and ILES data is seen when the 5thWN scheme is used, see Figure 3.20. Both formulations of the scheme are very close to DNS until the flow reaches a height of 2.5h where the profiles separate. After that point the DNS lies between the two 5thWN profiles. Low Mach Correction seems to have a positive effect on the 2ndVA and 5thM schemes, where the results are in

very good agreement with the DNS, especially in case of 2ndVA_LM. However, as the flow approaches the upper boundary, the 5thM profiles are crossing each other and as a result the 5thM profile becomes now closer to DNS. Finally, DNS is placed between the 9thWN profiles.

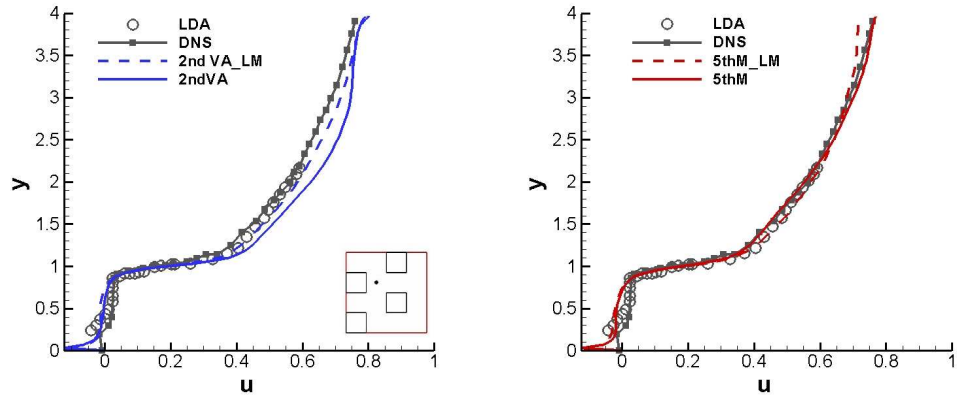

(a) 2nd Order MUSCL with Van Albada limiter

(b) 5th Order MUSCL

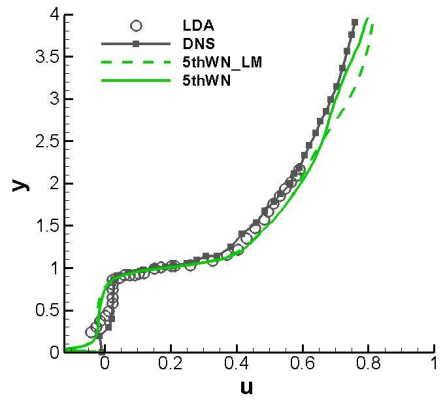

(c) 5th Order WENO

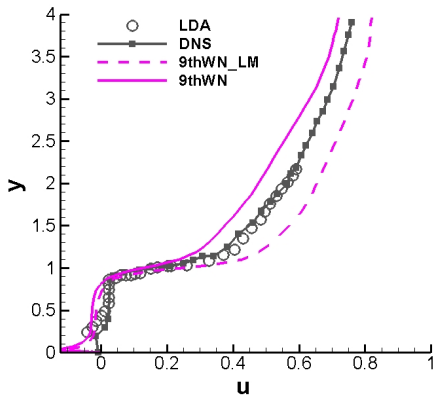

(d) 9th Order WENO

Figure 3.21: ILES against DNS data at location p1.

Comparisons in the wake of the cube are illustrated in Figure 3.21. The 2ndVA_LM profile continues to be in very good agreement with the DNS data, whereas the 5thM performs better now. Both forms of 5thWN overpredict to a small extent the velocity profile in comparison with DNS. Since the DNS and LDA data have been in very good agreement so far, it was expected that the DNS would be found between the 9thWN results.

Regarding location p2, the best agreement between the two numerical methods is seen in Figure 3.22(c). Both forms of 5thWN and DNS produce the same velocity profile which is slightly underpredicted when compared to the LDA data. The 5thM_LM seems to resemble the DNS profile up to three times the height of the cube. However, the 5thM profile starts to diverge from the DNS results at an earlier location. An almost

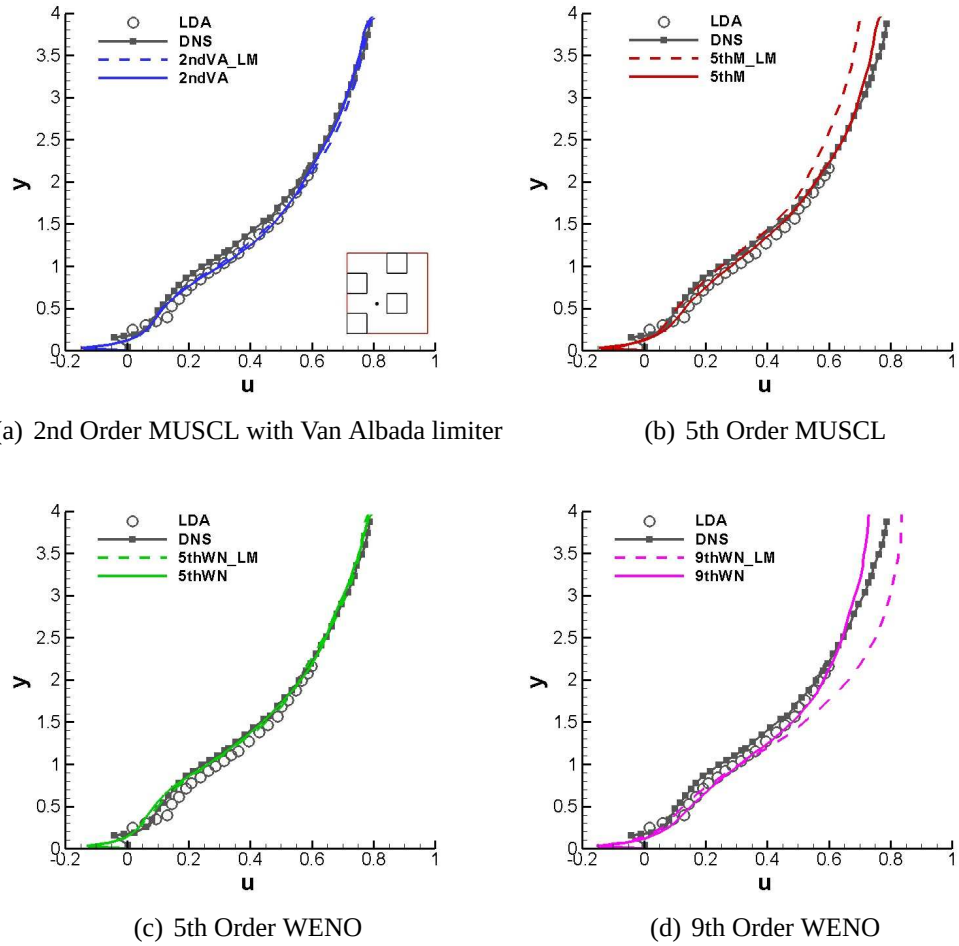

(a) 2nd Order MUSCL with Van Albada limiter

(b) 5th Order MUSCL

(c) 5th Order WENO

(d) 9th Order WENO

Figure 3.22: ILES against DNS data at location p2.

negligible overprediction is seen between the 2ndVA profiles and DNS up to 2.5 times the height of the cube. As the flow develops, the profiles converged as if they almost collide. Finally, the LDA data lies between the DNS and 9thWN profile. After the point where there is no available experimental data, DNS crosses 9thWN.

Comparisons at the last location are given in Figure 3.23. An underprediction is seen between the ILES results and the DNS data when the 2ndVA scheme is used. However, the ILES exhibits better comparison with the LDA data than the DNS. Below and above the cube, the 5thM scheme produces very good agreement with the LDA data. The best comparison, though, is seen when the 5thWN is compared against DNS above the cube height. Comparisons between the 9thWN scheme and DNS show that 9thWN is now closer to the LDA than the DNS, although it was originally diverging from both DNS and LDA profiles at locations p0 and p1.

By summing up all the above remarks, the results reveal the same trend is seen as in the comparisons with LDA data with most of the schemes exhibiting an similar behaviour to the DNS simulations. Results obtained with ILES16 achieved very good agreement

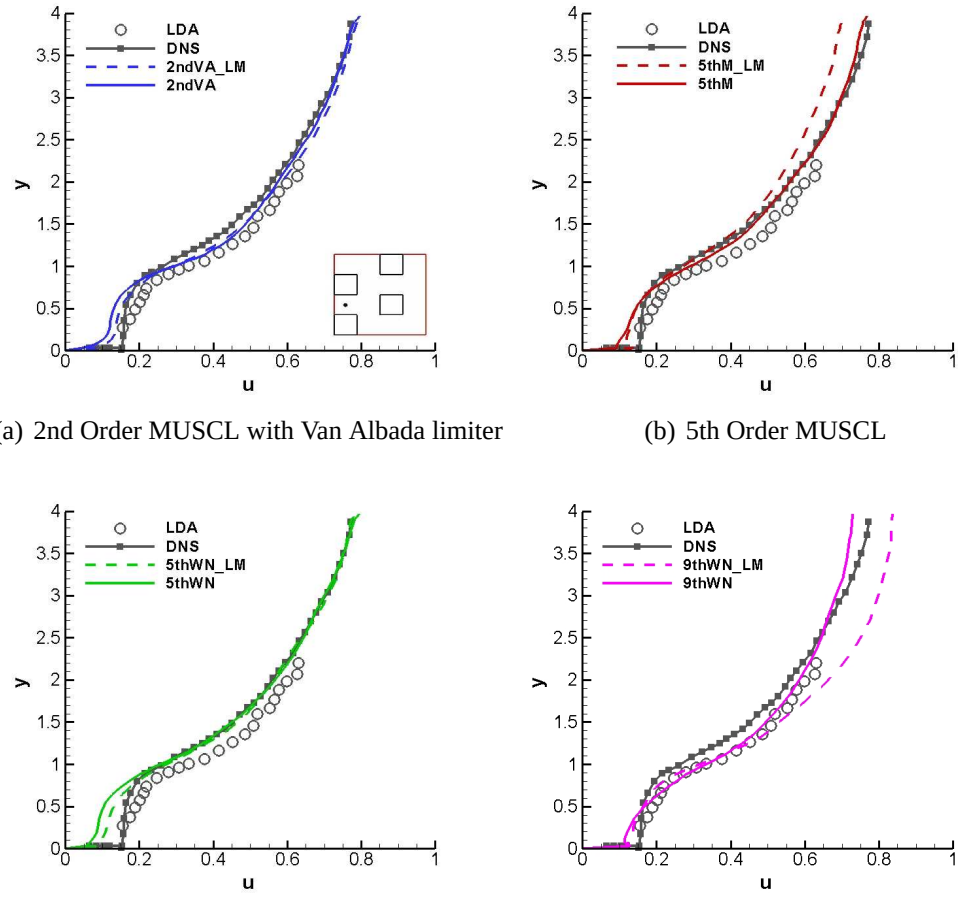

(a) 2nd Order MUSCL with Van Albada limiter

(b) 5th Order MUSCL

(c) 5th Order WENO

(d) 9th Order WENO

Figure 3.23: ILES against DNS data at location p3.

with DNS and even better comparison with the LDA data at some locations. The ability of ILES to produce DNS-like characteristics on a relatively coarse grid, which consequently means reduced CPU requirements, is a very encouraging indication for the applicability of ILES.

Comparison with LES data

Further assessment of ILES involved comparisons between ILES16 and LES data. The LES data presented in this section was obtained using three different grid resolutions, see Table 3.2. For simplicity, the LES results will be referred as LES8, LES16 and LES32, each one representing the number of grid points per cube height.

Comparisons between ILES16 and LES at location p0 are shown in Figure 3.24. The 2ndVA coupled with the Low Mach Correction Treatment gives results directly comparable with LES8 whereas the 2ndVA lies between LES16 and LES32. However, the velocity values at the top of the boundary are closer to the values obtained with LES8.

Regarding the 5thM, LES8 is in good agreement with the 5thM_LM until the flow reaches 3 times the height of the cube. A similar picture presents itself for 5thWN. Comparisons indicate agreement of the 5th_LM with the LES8, whereas 5thM gives results between the LES16 and LES32. Discrepancies in the velocity magnitude are seen with the 9thWN.

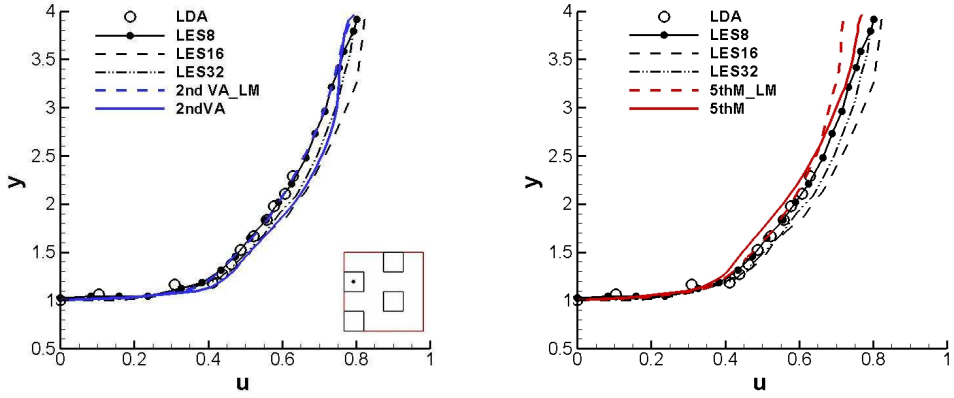

(a) 2ndVA scheme

(b) 5thM scheme

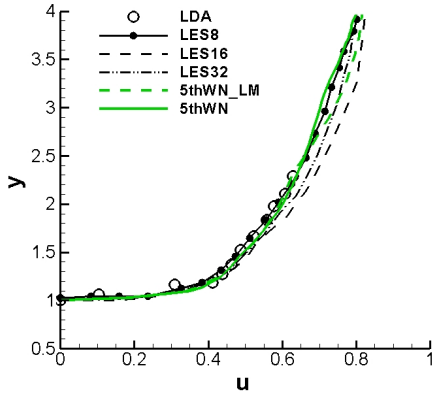

(c) 5thWN scheme

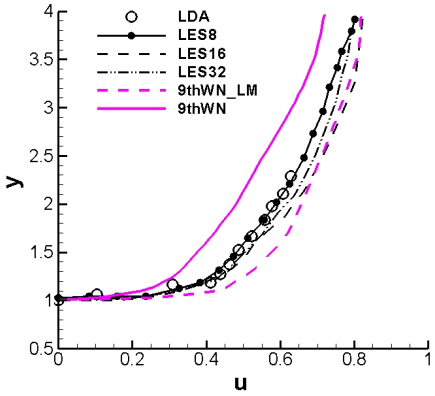

(d) 9thWN scheme

Figure 3.24: ILES against LES data at location p0.

Comparisons at location p1 can be found in Figure 3.25. The 2ndVA scheme produced results comparable to LES16 which was obtained using the same grid resolution. However, when the Low Mach Correction Treatment was implemented, the results appeared closer to LES32. Regarding the 5thM scheme, it seems to be in good agreement with the LES8. The 5thWN scheme (either blended or not with Low Mach Correction Treatment) gives results that resemble those of LES32. For the first time the 9thWN_LM appears to be comparable with other numerical data at location p1. Specifically, 9thWN_LM slightly underpredicts the velocity profile in comparison with LES on the same grid size.

Regarding location p2, shown in Figure 3.26, the LES profiles show a general tendency

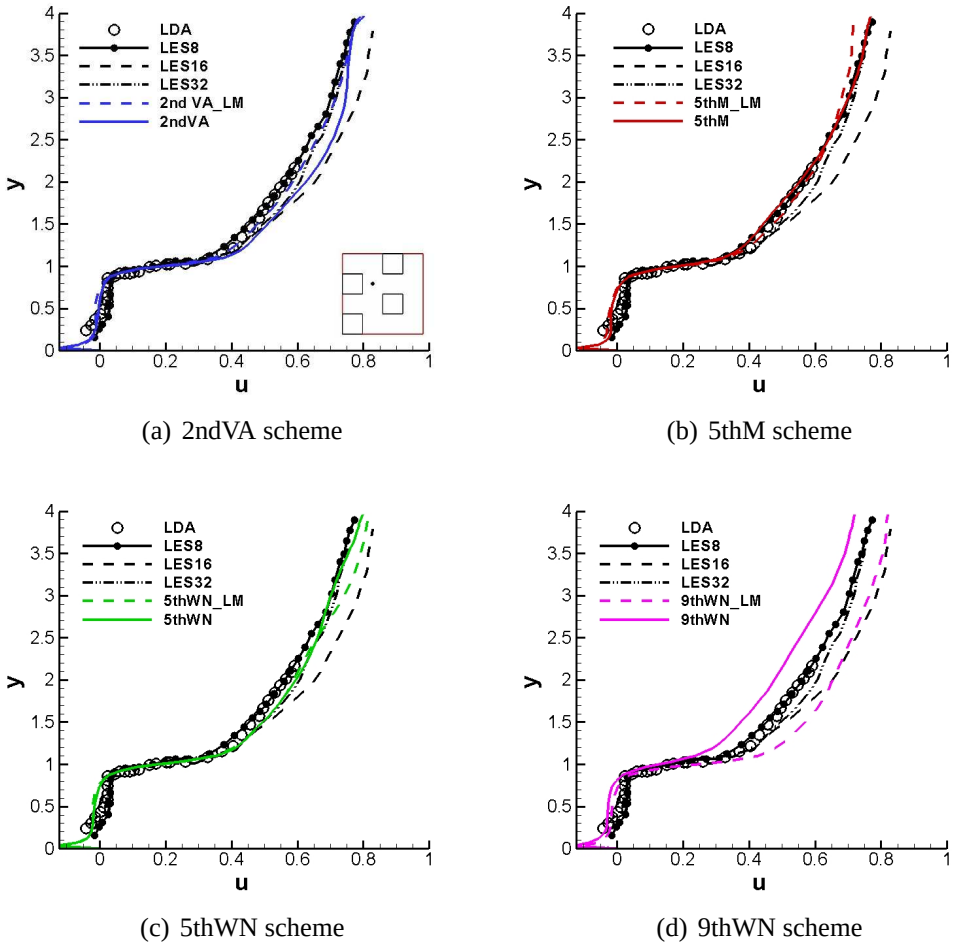

(a) 2ndVA scheme (b) 5thM scheme

(c) 5thWN scheme (d) 9thWN scheme

Figure 3.25: ILES against LES data at location p1.

of diverting from the ILES profiles when the two numerical approaches are compared at the same grid resolution. Almost all high-resolution schemes, either in their original form or coupled with Low Mach Correction Treatment, appear close to LES8. Only the 9thWN_LM scheme seems to overpredict the velocity magnitude.

Finally, comparisons at location p3 are seen in Figure 3.27. The numerical methods follow the same behaviour as in Figure 3.26 over the top boundary of the cube, whereas below the height of the obstacle ILES seems to be closer to the LDA data. The most accurate results among all ILES and LES data are given by the 9thWN scheme.

Summing up, it can be said that although increased grid resolution would be expected to result into higher accuracy on the contrary LES8 provided the best comparison with the LDA data. It should also be noted that the same behaviour was seen in the ILES results when obtained on the three different grids as shown in Section 3.3.1.

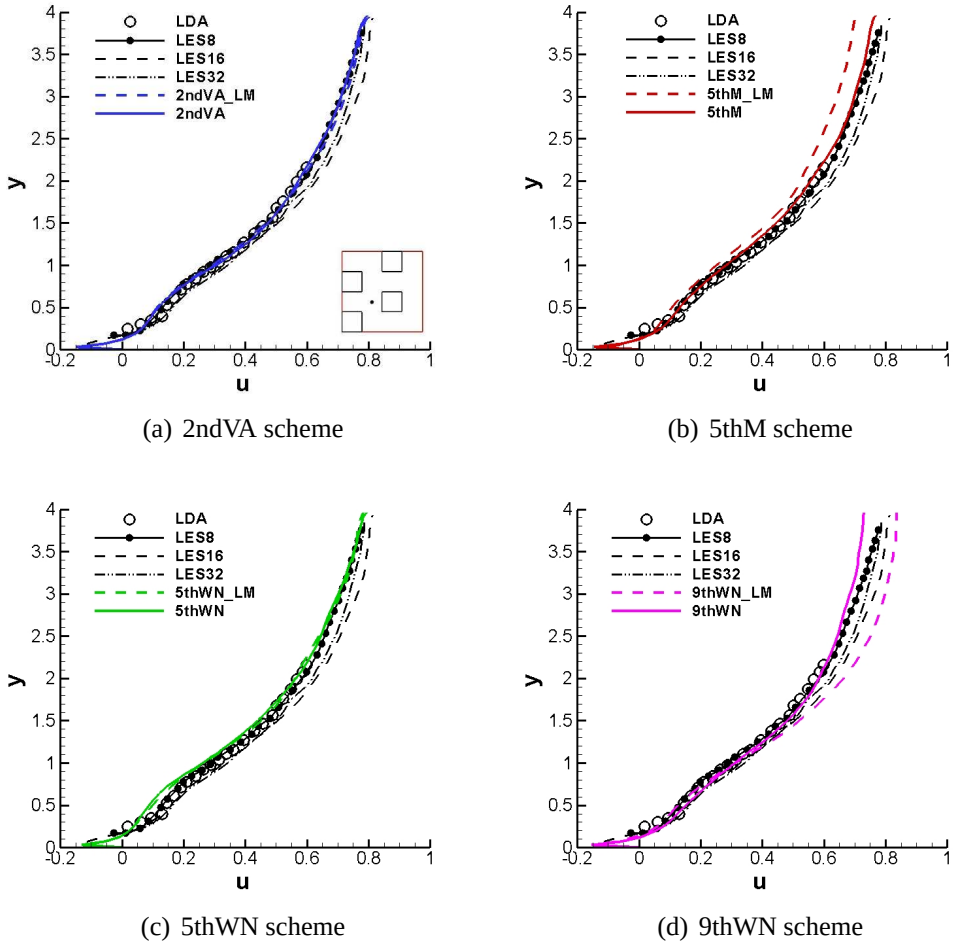

(a) 2ndVA scheme (b) 5thM scheme

(c) 5thWN scheme (d) 9thWN scheme

Figure 3.26: ILES against LES data at location p2.

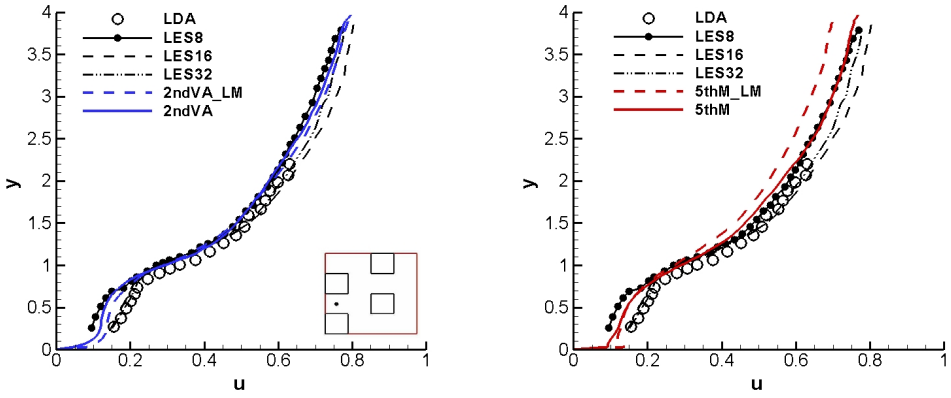

(a) 2ndVA scheme

(b) 5thM scheme

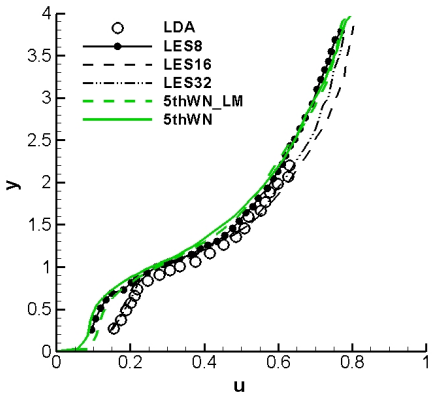

(c) 5thWN scheme

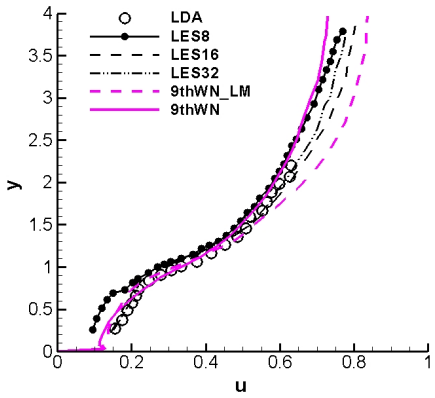

(d) 9thWN scheme

Figure 3.27: ILES against LES data at location p3.

3.3.4 Spatial Averaged Velocity Profile

Under neutral conditions, the vertical wind variation within the inertial sublayer can be described by the logarithmic law given in Equation 1.1.1. In Cheng and Castro [12], it is stated that, in order to obtain a representative wind profile, spatial averaging of the mean velocity data over a sufficient number of individual locations is required. An area of 40 x 40 mm containing one cube was chosen as the area under consideration, see Figure 3.28. Initially, 25 measurement points (represented by the black dots in Figure 3.28) were identified within the specific area. For each point the mean vertical velocity profiles were gathered and they were averaged at each fixed height giving a 25-point spatial averaged velocity profile. The spatial averaged mean velocities were calculated according to

$$u_{sa} = \frac{1}{n}\sum_{i=1}^{n} u_i, \tag{3.3.1}$$

where n is the number of individual measurement points within the repeating unit and u_{sa} is the spatial mean velocity. Considering the method as relatively time-consuming for an experiment, it was decided to investigated whether a much smaller number of locations would be sufficient to represent the logarithmic wind profile [12]. Consequently, the same procedure was followed using data gathered from only four locations illustrated by the red squares in Figure 3.3.1. Finally, data obtained using each method separately was fitted within a logarithmic curve and the two methods were compared against each other. Comparisons showed that both methods give very similar results, a fact that simplifies the calculation procedure significantly. However, it should be noted that such a simplification may not be appropriate for more complex cases.

In Equation 1.1.1, the friction velocity u_* is used as the slope fit in the logarithmic law profile. Therefore, its value needs to be calculated in contrast with the zero plane displacement (d) and surface roughness parameter (z_0) which can be obtained through the fitting of velocity data into a logarithmic curve. When the viscous contribution is assumed negligible, u_* can be determined by calculating the drag force from the pressure distribution on the front and back faces on the cubes. As shown in Equations 3.3.2 to 3.3.4, the friction velocity can then be determined from the wall shear stress which is obtained from the drag force.

$$D = \int (p_f - p_b) dA, \tag{3.3.2}$$

$$\tau_p = \frac{D}{A_c}, \tag{3.3.3}$$

$$u_*(p) = \sqrt{\frac{\tau_p}{\rho}}, \tag{3.3.4}$$

where p_f and p_b are the pressures over the front and back face of the cubes respectively, D is the drag force, τ_p stands for the shear stress due to the drag, A_c is the plan area equal to $4h^2$, ρ is the density of the fluid and finally, $u_*(p)$ is the friction velocity.

Nonetheless, there are cases where a direct measurement of the drag force is not possible, so the u_* is deduced from turbulence shear stress measurements in the region above the roughness surfaces [12]. Depending on whether the information is obtained from the inertial, roughness or even both sublayers combined, u_* is defined as $u_*(IS)$, $u_*(RS)$ and $u_*(IS\&RS)$, respectively. Different values of zero-plane displacement (d) and roughness length (z_0) were found when the logarithmic law was fitted using various u_*. A summary of the surface characteristics of the staggered cubical array extracted from the four locations only, is shown in Table 3.3 as presented in the work of Cheng and Castro [12].

Roughness Parameters	$u_*(p)$	$u_*(IS\&RS)$	$u_*(RS)$	$u_*(IS)$
u_*/U_r	0.0724	0.0635	0.0631	0.0639
d	0.725	0.835	0.975	0.74
z_0	0.0665	0.0405	0.0475	0.0345

Table 3.3: LDA surface characteristics [12].

As part of the numerical scheme dependency investigation, mean velocity profiles have been obtained with all schemes (either in their original form or modified) at specific locations consistent with the methodology presented in Cheng and Castro [12]. The profiles were then spatially averaged and fitted into the logarithmic Equation 1.1.1 using linear regression analysis along with least square fitting. Given the fact that the wind logarithmic profile contains three unknowns, u_*, d and z_0, two curve fitting procedures were followed each one involving a different degree of freedom. Specifically, the first one considered the third constant, the roughness parameter z_0, as a known variable whereas the remaining two variables were obtained. The z_0 was chosen on the basis that the computational array is identical to the one described in the experimental study of Cheng and Castro [12] hence the two arrays have the same roughness. The experimental surface parameters which were obtained based on information gathered from both the inertial and roughness sublayer, provided a better fit, thus the value of z_0 was set to 0.0405 accordingly. In the second procedure, all three variables u_*, z_0 and d, which introduce three degrees of freedom, were attained from the curve fitting. For simplicity, the surface characteristics obtained with the two and three-parameter fit will be referred as ILES_UH2 and ILES_UH3 respectively.

Results obtained with the two parameters fitting procedure using information gathered from the 25 and 4 points are given in Table 3.4 and Table 3.5, respectively. The ILES surface parameters exhibit very good agreement with the experiment parameters using the value $u_*(IS\&RS)$ as slope fit. All numerical velocity profiles seem to follow the logarithmic profile. Very small differences are seen in the surface parameters between the schemes however all values look reasonable. More precisely, the 2ndVA_LM and the 5thM_LM gave very close results to the LDA data. Despite the fact that the 9thWN

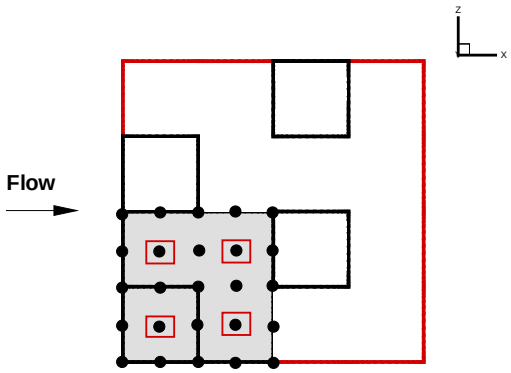

Figure 3.28: Highlighted locations of spatial averaging.

seemed to diverge in magnitude when predicting the mean velocity profiles, it was proven that it is capable for providing results that follow the logarithmic profile. It is also verified that the 25-point and the 4-point spatial averaged profiles show very small differences in magnitude. Therefore, spatial averaging using only four locations it is indeed a valid method for the specific case.

Table 3.6 presents results found using the three parameter fit when the velocity profiles are spatially averaged among the four locations. By comparing Table 3.6 and Table 3.5, the three parameter fit shows discrepancies with the LDA data, in six out of the eight schemes used in this thesis, due to the highly overpredicted value of the roughness factor,z_0. However, the 2ndVA_LM and the 5thM_LM maintain their good agreement with the experimental data. Specifically, the percentage difference in terms of z_0 ranges between 3% – 4% as given in Table 3.7.

Roughness Parameters	2ndVA_LM	2ndVA	5thM_LM	5thM	5thWN_LM	5thWN	9thWN_LM	9thWN
u_*/U_r	0.0657	0.0719	0.0657	0.0701	0.0712	0.0719	0.0774	0.0690
d	0.8280	0.8746	0.8280	0.9174	0.8545	0.9099	0.8868	0.7805

Table 3.4: ILES surface parameters using the 2-parameter fit over 25 points.

Roughness Parameters	2ndVA_LM	2ndVA	5thM_LM	5thM	5thWN_LM	5thWN	9thWN_LM	9thWN
u_*/U_r	0.0650	0.0715	0.0652	0.0702	0.0705	0.0718	0.0776	0.0692
d	0.8011	0.8612	0.8203	0.9065	0.8275	0.9000	0.8841	0.6976

Table 3.5: ILES surface parameters using the 3-parameter fit over 4 points.

In addition to the tables presented so far, the logarithmic velocity profiles using LDA roughness parameters within the IS&RS regions and ILES using the 5thM_LM were plotted against each other. The LDA data is compared against the unfitted spatially averaged ILES profile and against the profiles obtained with the two fitting procedures.

Roughness Parameters	2ndVA_LM	2ndVA	5thM_LM	5thM	5thWN_LM	5thWN	9thWN_LM	9thWN
u_*/U_r	0.0655	0.1028	0.0655	0.0924	0.0921	0.1000	0.0892	0.0542
d	0.7944	0.5110	0.7946	0.6919	0.5694	0.6221	0.7816	0.9007
z_0	0.0420	0.1570	0.0419	0.1144	0.1147	0.1386	0.0704	0.0121

Table 3.6: ILES surface parameters using the 3-parameter fit.

Roughness Parameters	2ndVA_LM	5thM_LM	9thWN
u_*/U_r	3.1%	3.1%	14.6%
d	4.8%	4.8%	8%
z_0	3.7%	3.4%	70%

Table 3.7: Percentage difference between ILES and LDA surface parameters using 3-parameter curve fitting.

Although the roughness parameters were directly determined from the mean velocity profiles using statistical methods, Figure 3.29 clearly shows that ILES data is comparable to LDA data.

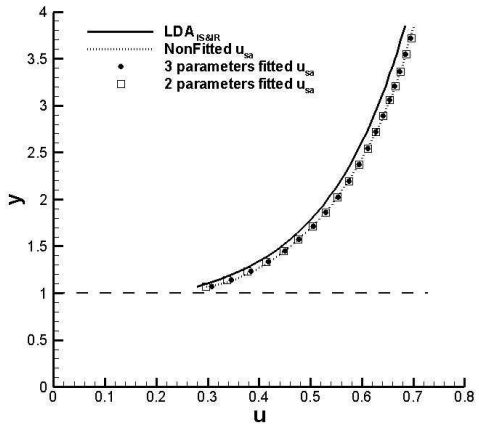

Figure 3.29: LDA against ILES in terms of spatial averaged velocity profiles.

3.3.5 Computational Time Step Dependency

According to the CFL definition, a smaller computational step should result in more accurate prediction. However, high order spatial discretisation schemes allow accurate results to be computed for higher values of CFL. Therefore, it was decided to investigate the computational time step dependency by reducing the CFL number when the ninth-order accurate WENO scheme is used for spatial discretisation. It should be noted that the current CFL value already produced results comparable to experimental data.

Roughness Parameters	CFL=0.5	CFL=0.3
u_*/U_r	0.0875	0.087
d	0.7979	0.7978
z_0	0.0663	0.066

Table 3.8: Surface parameters obtained from 25 points for evaluating the CFL condition.

Roughness Parameters	CFL=0.5	CFL=0.3
u_*/U_r	0.0892	0.089
d	0.7816	0.7817
z_0	0.0704	0.07

Table 3.9: Surface parameters obtained from 4 points for evaluating the CFL condition.

Comparisons between two CFL numbers are presented in terms of roughness element parameters in Table 3.8 and Table 3.9 using the 25 points and 4 points spatial averaging procedure, respectively. The results show very small discrepancies, verifying that higher order discretisation scheme are capable of using higher values of CFL without affecting their accuracy.

3.3.6 Energy Spectral Analysis

In order to obtain information about the characteristics of the flow topology, the three dimensional energy spectra was employed using the time signal of the instantaneous streamwise velocity. The existence of fully developed turbulence can be proven based on Kolmogorov's theory that the energy spectra for homogeneous and isotropic turbulence is proportional to the $k^{-5/3}$ where k is the wavenumber. To assess the performance of ILES, the energy spectra (using a Fourier series transformation as described in Chapter 2) was calculated for the five distinctive points shown in Figure 3.30. Each location refers to a recirculation area around one cube: in the front, at the sides and in the wake of the cube.

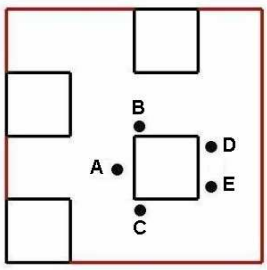

Figure 3.30: Highlighted locations for calculating the energy spectrum.

Schemes	Position A	Position B	Position C	Position D	Position E
2ndVA	−1.78	−1.79	−1.76	−1.76	−1.79
5thM	−1.67	−1.67	−1.76	−1.76	−1.79
5thWN	−1.75	−1.77	−1.77	−1.79	−1.76
9thWN	−1.78	−1.79	−1.79	−1.76	−1.79

Table 3.10: Energy spectra slopes for schemes in their original form.

Schemes	Position A	Position B	Position C	Position D	Position E
2ndVA	−1.78	−1.79	−1.76	−1.76	−1.78
5thM	−1.81	−1.79	−1.81	−1.77	−1.81
5thWN	−1.78	−1.80	−1.79	−1.77	−1.81
9thWN	−1.78	−1.74	−1.75	−1.76	−1.74

Table 3.11: Energy spectra slopes for schemes using Low Mach Correction Treatment.

In Figure 3.31, the energy spectra obtained at all locations using the 5thM_LM scheme is given as an example. The results were compared against Kolmogorov's theory of $k^{-5/3}$ and the slopes of energy spectra were calculated by fitting a power law curve, see Table 3.10 and Table 3.11. From the results, it can be stated that Kolmogorov's theory is approached in the wake of the cube and specifically at location D. It should be noted that the fitted curve slopes were compared against the reference slope of $-5/3 \approx -1.67$. The peaks at k=10 is just noise.

Based on the results, it can be said that the energy spectral slopes are similar for all schemes however small differences are present. Thus, when the schemes are used in their original form, Kolmogorov's theory is reached earlier with the 5^{th} MUSCL scheme almost in all locations. However, the 9thWN scheme approaches the slope $k^{-5/3}$ when the schemes are modified using the Low Mach Correction Treatment.

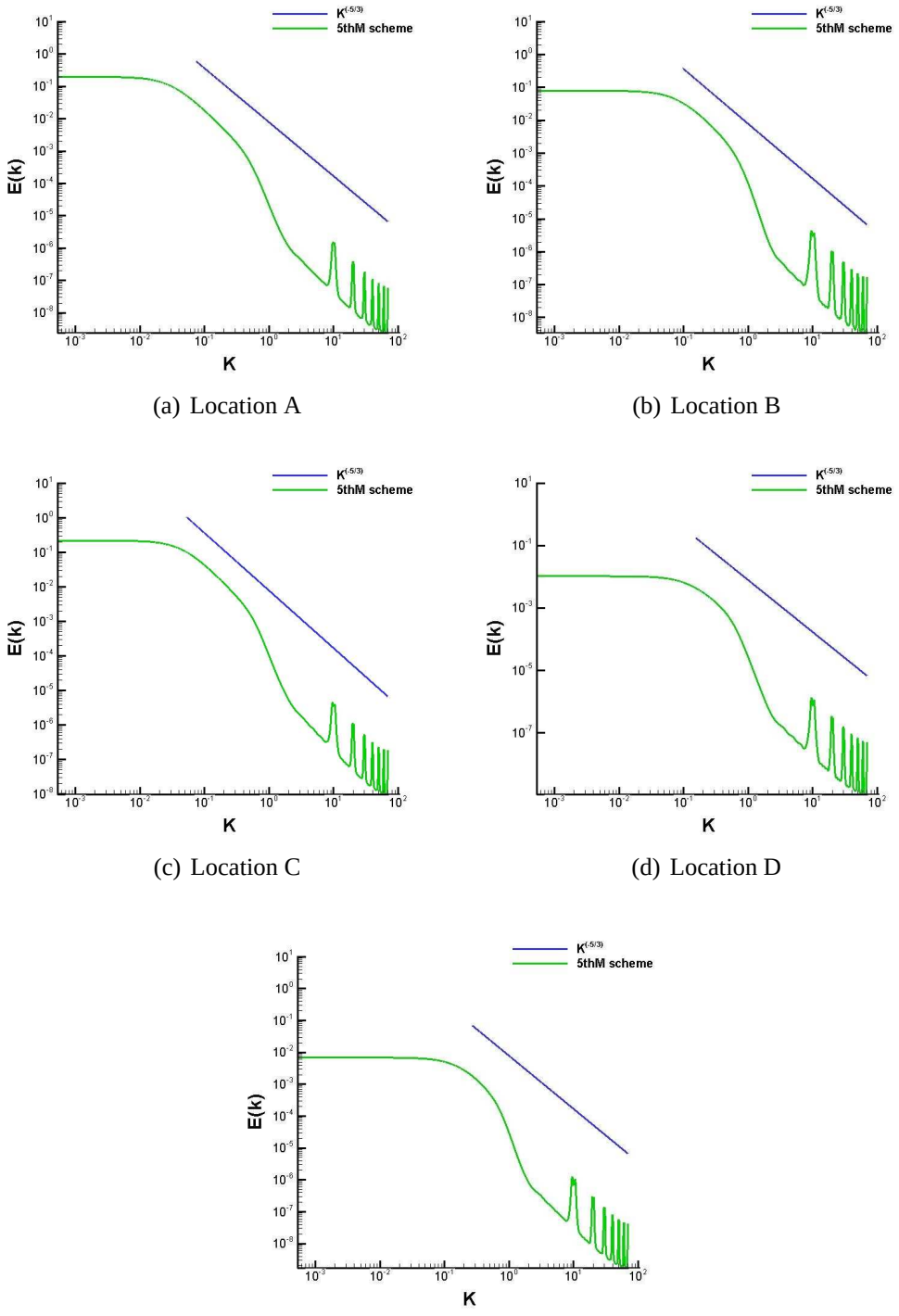

(a) Location A

(b) Location B

(c) Location C

(d) Location D

(e) Location E

Figure 3.31: Energy spectra.

3.4 Summary

Implicit Large Eddy Simulation using high-resolution methods was applied to flows around a staggered array of four cubical elements representing buildings. Real urban environment involving separation and reattachment areas due to wind's interaction with buildings or other roughness elements, provides an excellent test case for assessing the accuracy of ILES in predicting such highly complex flows. The investigation was performed in stages focusing on the effects of numerical parameters on the solution. Three computational grids referring to different resolution depending on the number of grid points per cube height were used in the simulations. Therefore ILES16, ILES24 and ILES32 correspond to 16, 24 and 32 grid points, respectively.

Initially, the effects of grid resolution were assessed using results obtained on the three different computational grids. The results were then compared against experimental data in terms of mean and turbulent statistics at four distinct locations within the domain. It was concluded that, in cases where the ILES16 or ILES24 grid was used, the comparisons between the numerical and experimental data were in very good agreement. Surprisingly however, the numerical solution deteriorated when the grid resolution was increased. More precisely, a higher mass flow rate was detected in the ILES32 case, indicating that the value of the imposed constant forcing term does not preserve a constant mass flow throughout the domain.

The dependency on the numerical scheme was examined by applying four high resolution schemes in their original form on the ILES16 grid. The schemes were the 2^{nd} order accurate MUSCL scheme coupled with the Van Albada limiter, the 5^{th} order accurate MUSCL scheme, the 5^{th} order accurate WENO scheme and finally the 9^{th} order accurate WENO scheme. As a second stage of investigating the numerical scheme dependency, all the above schemes were combined with the Low Mach Correction Treatment in order to further examine the sensitivity on the same computational mesh. From the results obtained, it is clear that almost all schemes, with exception of the 9thWN scheme, exhibit similar behaviour and reasonable agreement with the LDA data. For the specific case of the 9thWN scheme, a dependency upon the location of the comparison point is observed. Here, the best performance is achieved when predicting the streamwise velocity profile within the cube cavity and in front of a cube. In a similar manner, the 9thWN scheme seems to be strongly affected when combined with the Low Mach Correction Treatment.

By comparing the velocity profiles obtained with the 9thWN scheme and the grid refinement procedure, it could have been said that the results seemed to be in the opposite direction. However, this observation is not valid due to the fact that an asymptotic behaviour would have been observed only if the results in Section 3.3.1 have indicated a fully grid converged solution.

As an additional measure of the schemes performance, the logarithmic wind profile above the cube height was fitted to the spatially averaged mean velocity data using the least squares method. According to the calculated roughness parameters, the best

agreement with the experimental data is given by the 5thM_LM and the 2ndVA_LM scheme followed by the 9thWN scheme. Combining all the statements made during the first two stages, it can be said that the most accurate prediction of the mean flow and turbulent statistics is shown when the 5thM_LM and 9thWN scheme are used with low grid resolution.

Based on the conclusions drawn from all the previous stages, the best performing schemes were chosen in order to proceed with the computational time step dependency. The value of CFL was reduced by 60% of its original value in order to investigate the computational time step effect. As expected, for high-order spatial discretisation schemes such as 9^{th} WENO scheme, it is possible to obtain accurate results in higher CFL numbers.

As part of this chapter, the energy spectra was calculated at five distinct locations around the cube, each referring to an identified recirculation area. The 9thWN scheme was compared against Kolmogorov's theory of $k^{-5/3}$ and it was found that the slope of $-5/3$ is approached when the scheme was coupled with the Low Mach Correction Treatment. However, based on comparisons among the schemes in their original formulation, the 5thM scheme was able to approach the $k^{-5/3}$ in the most accurate way.

In this chapter, an extensive investigation of the performance of the numerical schemes was presented in terms of mean and turbulent statistics. However, before closing this part of the thesis, a comparison in terms of CPU requirements for each scheme is provided for simulations performed on the computational mesh of approximately 0.2 million cells with 16 x 16 x 16 grid points per cube height. CPU requirements are given in Table 3.12 and correspond to the equivalent of a single processing time. The simulations were performed using 16 processors (Intel EM64T Xeon 51xx (Woodcrest) 3000 MHz (12 GFlops)) at the same CFL =0.5. All the comparisons given below refer to the same number of iterations (200000). As seen, the higher the scheme's order of accuracy, the longer the time window that ensures the convergence of the solution. Nonetheless, it can be stated that the requirements in CPU increase in a reasonable manner without becoming unaffordable. However, an inconsistency is noticed between the CPU hours for the 2ndVA scheme. Although, cases incorporating the Low Mach Correction treatment would have been expected to require additional CPU time, the exact opposite case is seen. One potential reason could be the overloading of the system.

Schemes	Original formulation	With Low Mach Correction Treatment
2ndVA	964.8	958.4
5thM	1006.4	1009.6
5thWN	1408	1419.2
9thWN	1432	1652.8

Table 3.12: CPU requirements in hours.

CHAPTER 4

Random Height Building Array

FLOWS over a more realistic representation of urban areas is the subject of this chapter. More precisely, high resolution schemes in the context of ILES will be assessed for simulating flows around sixteen buildings of five different heights in a staggered alignment. The aim of this chapter is to investigate the performance of high resolution schemes in a more complex geometry and to enhance the knowledge of the flow structure. The results were obtained by applying the 5^{th} order accurate MUSCL scheme coupled with the Low Mach Correction Treatment. Comparisons with experimental data provided in Cheng and Castro [12] and numerical data found in Xie and Castro [87] will be presented in terms of mean statistics.

4.1 Numerical Details and Settings

In a similar way as for the case of four cubes discussed in Chapter 3, the numerical set up of the case under investigation was based upon information found in the wind tunnel experiment of Cheng and Castro [12] and the LES study of Xie and Castro [87]. More details will be given in the section that follows.

Domain Decomposition

The computational domain consists of sixteen rough elements representing buildings. Each three dimensional element has a square footprint of $h_{mean} \times h_{mean}$, with h_{mean} being the mean building height equal to 0.01 m. The height of the buildings is ranging from 0.0028 m to 0.0172 m based on a normal distribution with a mean deviation of 0.01 m and a standard deviation of 0.003 m. The size of the domain is L_x x L_y x L_z = $8h_{mean}$ x $10h_{mean}$ x $8h_{mean}$. The width of the passage between the buildings is 0.01 m, whereas the density of the area remains 25%. An illustration of the computational domain is given in Figure 4.1.

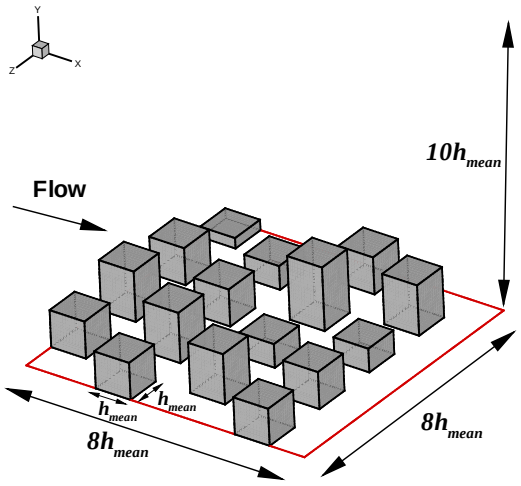

Figure 4.1: Computational domain.

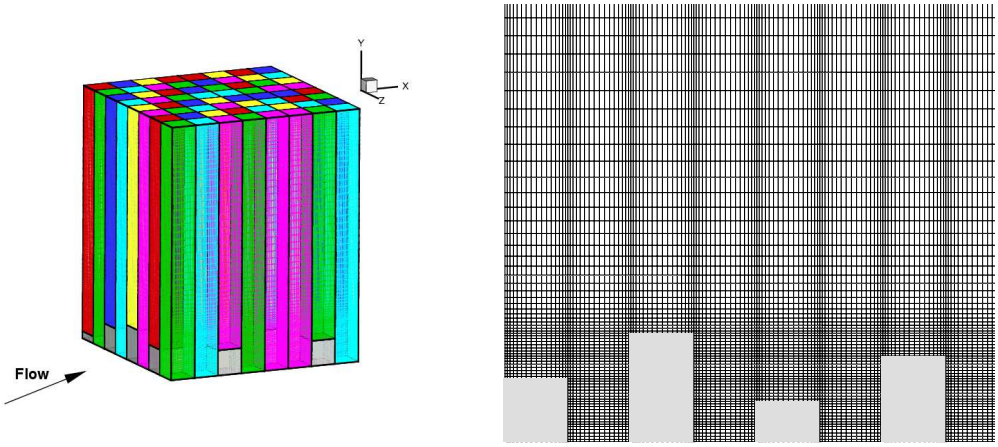

(a) Computational domain (b) Grid resolution along plane x=4.5

Figure 4.2: Computational grid.

Grid Resolution

The computational grid is blocked structured with the complete domain being split into 64 individual blocks as shown in Figure 4.2(a). Only one grid resolution was used for this case consisted of approximately 2 million cells with 16 x 16 grid points per $h_{mean} \times h_{mean}$. Figure 4.2(b) shows the grid resolution along a YZ plane. The highest element along the specific slice is also the highest obstacle in the domain. As seen, the grid density is increased near the wall region for better accuracy.

Numerical Settings

The exact same boundary conditions were imposed as in the four cubes case. Fully periodic conditions along the streamwise and spanwise direction, symmetry at the top

boundary, whereas the lower boundary and the faces of the buildings were considered as walls thus the non slip condition was chosen. In order to investigate the effect of the source term (pressure gradient), two different constant pressure gradients of $\frac{\partial p_1}{\partial x} = -1.59 Pam^{-1}$ and $\frac{\partial p_2}{\partial x} = -5.14 Pam^{-1}$ were simulated at the same Reynolds number of 6100. In the same extent, the physical dependency of the solution on the choice of the Reynolds number was examined using two different Reynolds numbers of 5000 and 6100 at a constant pressure gradient. The set up of the cases was based on the experimental studies of Cheng and Castro [12]. Both Reynolds numbers were based on the free stream velocity and mean height of the building [12]. Finally, the 5^{th} order accurate MUSCL scheme with the Low Mach Correction Treatment was used for the spatial discretisation whereas, the time integration was performed with the third order TVD Runge-Kutta scheme. The value of CFL was set to 0.5 in all simulations.

All dimensions, flow parameters and comparisons of mean statistics are presented in their non-dimensional form.

4.2 Flow Topology

As part of this thesis, a description the flow within the non uniform height building array will be attempted. Visualisation of the flow field will be made in terms of mean and instantaneous flow parameters. The flow structure is expected to maintain some of the basic flow characteristics as described in the case of the isolated cube [53] and the four cube array [12]. To facilitate the flow description, a plan view of the array is given in Figure 4.3(a) showing the element height and the orientation of the faces as front (F), back (B), left (L) and right (R). Additionally, the buildings were numbered as shown in Figure 4.3(b) and hereafter they will be referenced by their number.

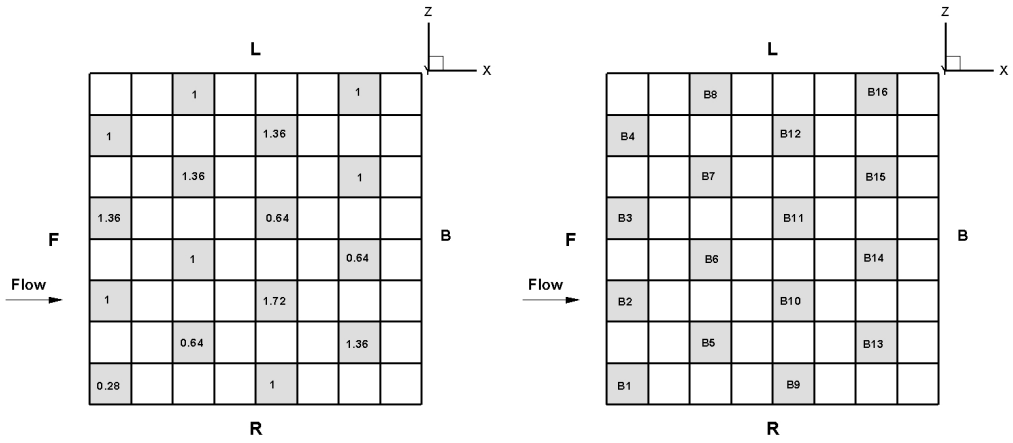

(a) Orientation of the flow and indications of the element height

(b) Numbering of the elements

Figure 4.3: Plan view of the building array.

A three dimensional impression of the flow field within the array is given in Figure 4.4.

The flow is visualised using volume ribbons coloured with velocity magnitude. The flow appears highly complex and irregular with intense turbulent structure at the sides of the buildings.

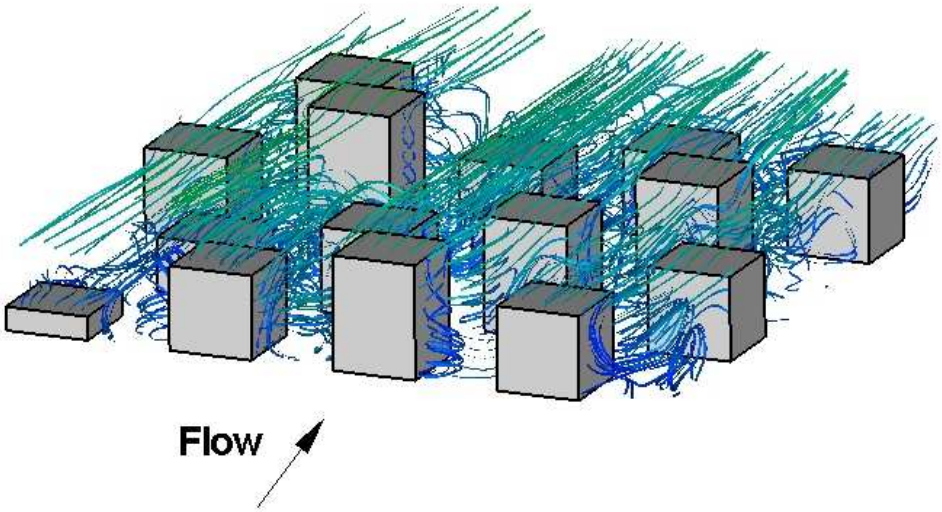

Figure 4.4: Flow structure within the domain.

In order to be more descriptive and obtain a clearer view of the flow structure, the computational domain was split into four areas. Each unit contains four elements of which at least two have different heights. Since the blocks have the same arrangement as in the case of four cubes the intention here is to investigate whether the flow pattern changes with ranging building height. The flow was visualised using velocity vectors at XZ planes. Specifically, two planes were extracted of which plane y=0.14 was used for describing the flow structure in unit A and y=0.5 for all remaining units.

Scenario A consists of blocks B1 (h = 0.28), B2 (h = 1.0), B5 (h = 0.64) and B6(h = 1.0) as shown in Figure 4.5(a). The incoming flow, through B1 and B2, gets redirected towards their wakes but also towards B5; see Figure 4.5(b). Since, B1 is the shortest block in the whole array, its blockage effect seems to be very small with the flow appearing to be mostly affected by the presence of B2. Thus, the side vortices of B1 look weak whereas a relatively big vortex is formulated at the neighbouring face of B2. The flow that gets through the gaps of the buildings, returns back to B1, due to the presence of B5, and takes part into the formulation of a very small vortex at the left back side of B1. Although, vortices should have been seen at the sides of B5 and B6, one big vortex is created instead. The vortex covers almost the whole area between B5 and B6 and seems to be closer to B6. Unfortunately, the wake vortices are not visible

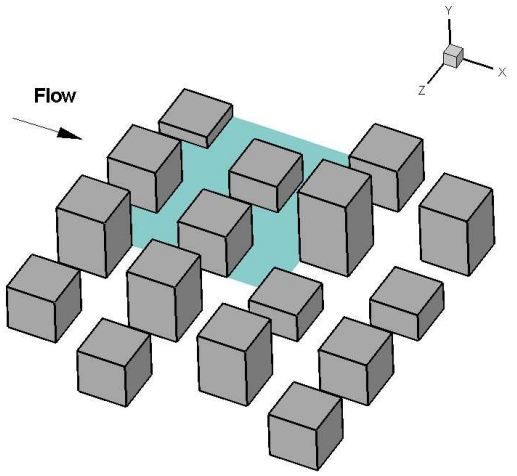

(a) Domain of unit A

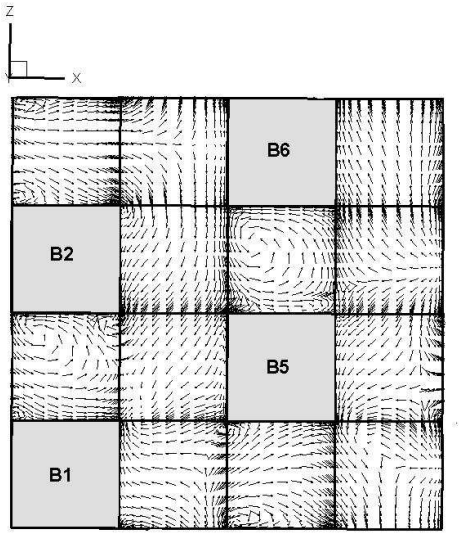

(b) Time-averaged velocity vectors in unit A

Figure 4.5: Flow structure in Unit A (y=0.14).

for all four elements, possibly due to the chosen XZ plane which is very close to the ground.

In both rows of Unit B, the highest block ($h = 1.36$) is followed by a shorter block ($h = 1.0$), see Figure 4.6(a). In Figure 4.6, the velocity vectors (extracted in plane y=0.5) show that whenever blocks of different height are adjacent, the side vortices between the neighboring faces tend to be shifted towards the face of the tallest block. The same behaviour was seen between B5 and B6 in Unit A. The redirected flow between B3 and B4 moves towards the wakes of the blocks until it gets stopped by B7. The only clear formulation of wake vortices can be seen behind B4.

In Unit C, all blocks are of different height as shown in Figure 4.7. A clear view of all side and wake vortices can be seen around B10 and B13, the highest buildings of the

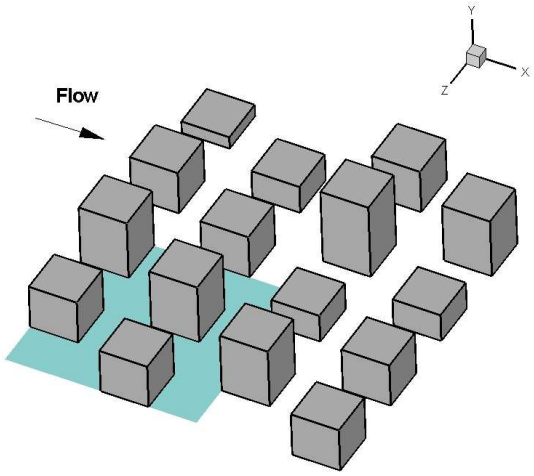

(a) Domain of unit B

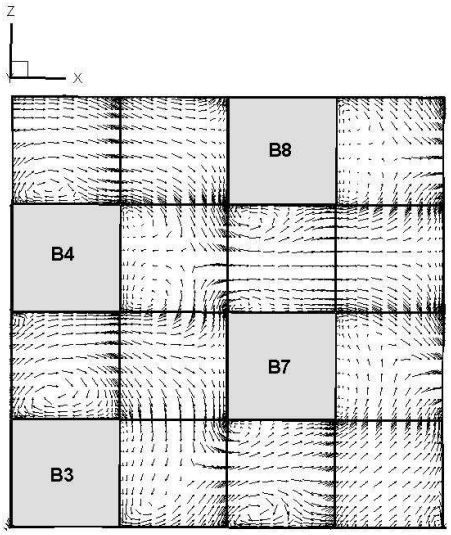

(b) Time-averaged velocity vectors in unit B

Figure 4.6: Flow structure in Unit B (y=0.5).

unit, whereas the flow topology around the shortest element B14 ($h = 0.64$) is barely visible; Figure 4.7(b). Finally, regarding Unit D, the interesting flow characteristic,is noticed in the wake of B12, see Figure 4.8(b). Although two vortices should have been present, there is only one and yet it is diagonal with its core found almost at the center of the wake. Before closing, it should be noted that the recirculation areas at the side and in the wake of the buildings are visible depending on the chosen plane, indicating that the location of the vortices vary with ranging height.

Visualisation of the flow structures around the buildings is given in Figure 4.9 using iso surfaces of the Q-criterion. The instantaneous flow field is clearly turbulent, exhibiting more intense vorticity around the buildings. As expected, based on the typical flow around an isolated obstacle, the vortical structures are visible in front, at the sides and

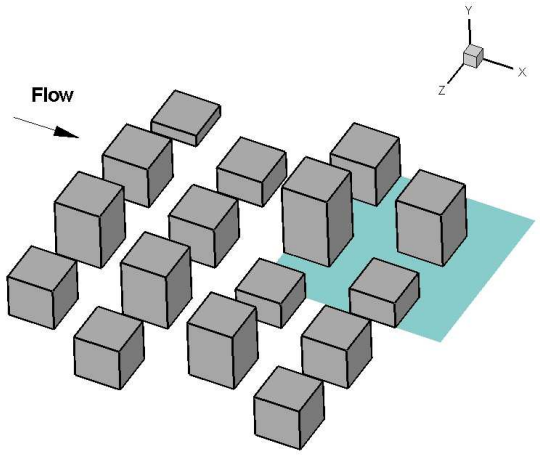

(a) Domain of unit C

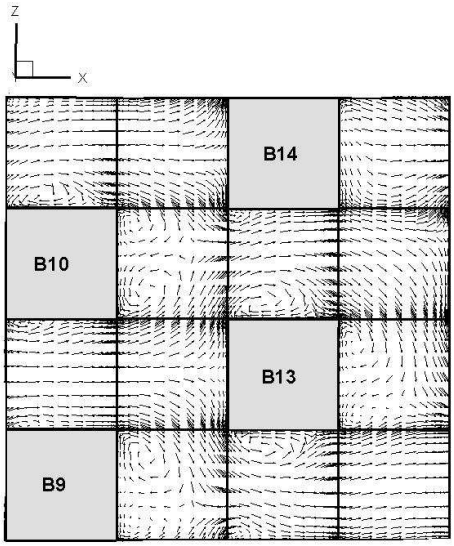

(b) Time-averaged velocity vectors in unit C

Figure 4.7: Flow structure in Unit C (y=0.5).

in the wake of the element. It must be noted that larger turbulent structures are seen in the vicinity of the highest building (element coloured in red).

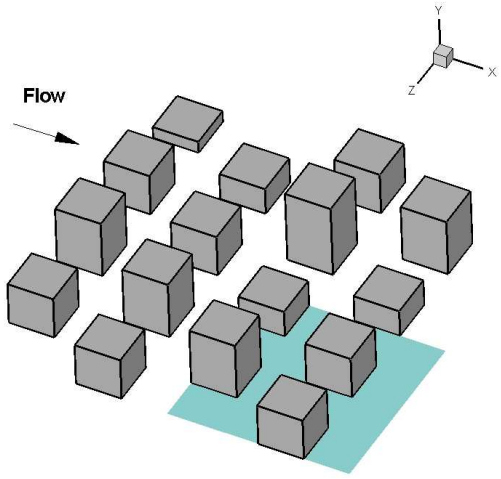

(a) Domain of unit D

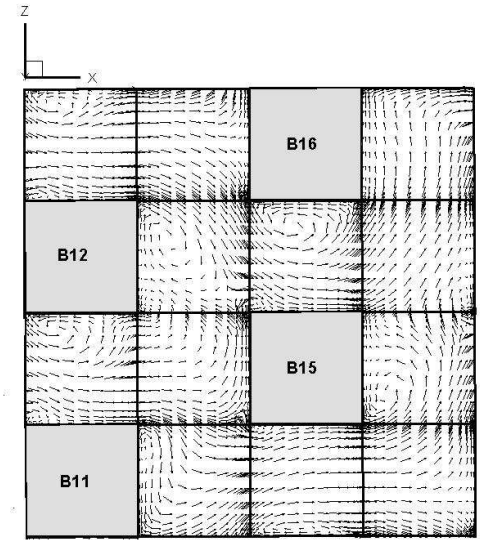

(b) Time-averaged velocity vectors in unit D

Figure 4.8: Flow structure in Unit D (y=0.5).

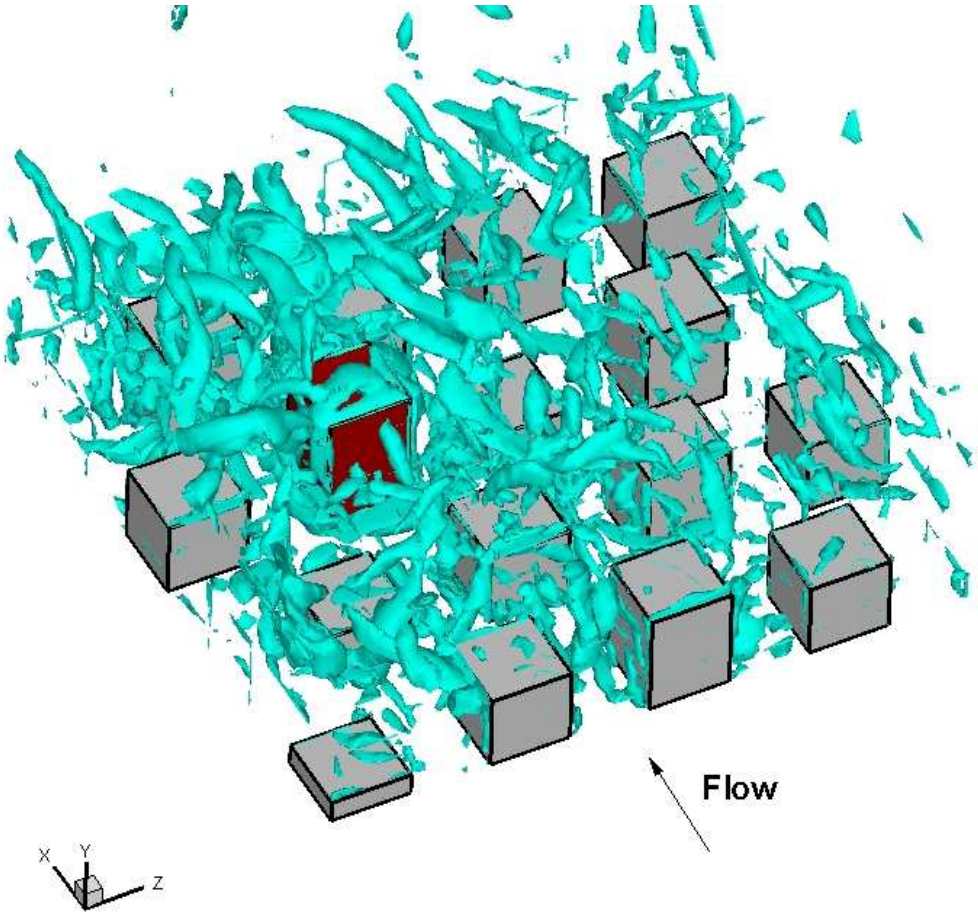

Figure 4.9: Instantaneous flow field visualisation using the Q-criterion - Isosurfaces of Q=0.2.

4.3 Results

The applicability of high-resolution methods in flows around rough elements has been discussed extensively in Chapter 3. In the sections that follow, the dependency of the solution on the Reynolds number and the validity of imposing a constant pressure gradient as a driving force under periodic conditions will be investigated in flows over a non uniform height building array. Additionally, comparisons between similar locations in the uniform and non uniform building matrix will be presented in order to investigate any significant differences in the flow features.

Six comparison points were identified as shown in Figure 4.10. Four out of the six locations around and above B6 ($H_{B6} = 1.0$, corresponding to the mean building height), were chosen in the same way as in the case of four cubes. As seen in Figure 4.10(b), vertical velocity profiles were extracted at positions (4,3), (4,4), (3,3) and (3,4) representing locations above B6, in the wake, in the cavity and in front of B10, respectively. The last two locations in the wake of B2 and B9 ($H_{B2} = H_{B9} = H_{B6} = 1.0$) were chosen in order to investigate whether similar positions exhibit altered velocity profiles due to the presence of non uniform height neighbouring obstacles.

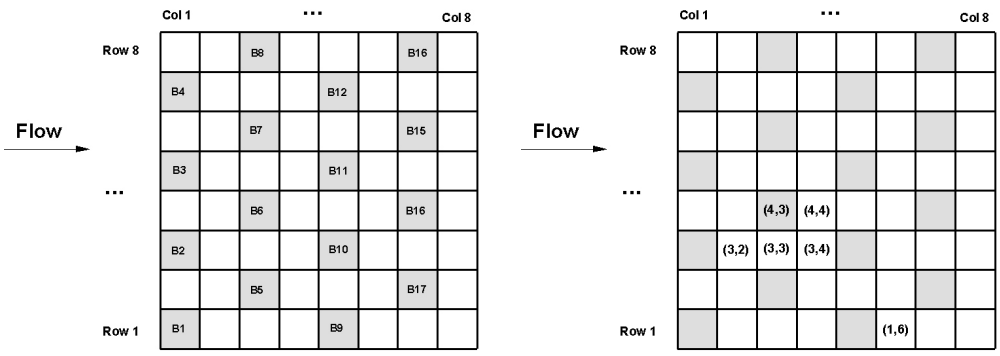

(a) Plan view indicating the block configuration (b) Comparison points

Figure 4.10: Highlighted locations of comparisons.

The ILES results were compared against Hot Wire Anemometer data (HWA hereafter) [12] and available LES studies [87, 88] in terms of mean vertical velocity profiles. Additionally, a number of mean velocity profiles was gathered and, after being spatially averaged, they were fitted into a logarithmic curve. The deduced surface parameters were compared with HWA data, but also with the parameters found in the case of four cubes.

As mentioned before, all mean and turbulent statistics are presented in their non dimensional form and have been averaged over a sufficient time window (approximately 140 flow-through-times) to ensure convergence of the large scales as shown in Section 2.8.2.

4.3.1 Constant Pressure Gradient Dependency

In Xie and Castro [87], it was stated that the choice of imposing a constant pressure gradient as a driving force for fully periodic boundary conditions was a valid method. However, in Chapter 3 of this thesis discrepancies in the velocity profiles were seen when the same value of pressure gradient was used with different grid resolutions. To assess the dependency of the results on the choice of the constant pressure gradient, two simulations referring to a different value of $\frac{\partial p}{\partial x}$ were performed. The first pressure gradient was equal to the one used in the four cubes case $\frac{\partial p}{\partial x} = -1.59 Pam^{-1}$ whereas the second one was set to $-5.14 Pam^{-1}$ in accordance to the LES study of Xie et al. [88] of flows in a similar non uniform height array. In the comparison that follows, the different values of $\frac{\partial p}{\partial x}$ will be referred as P_{grad1} and P_{grad2}. The flow conditions within the element array corresponded to a Reynolds number of Re=6100 based on mean building height and free-stream velocity [12].

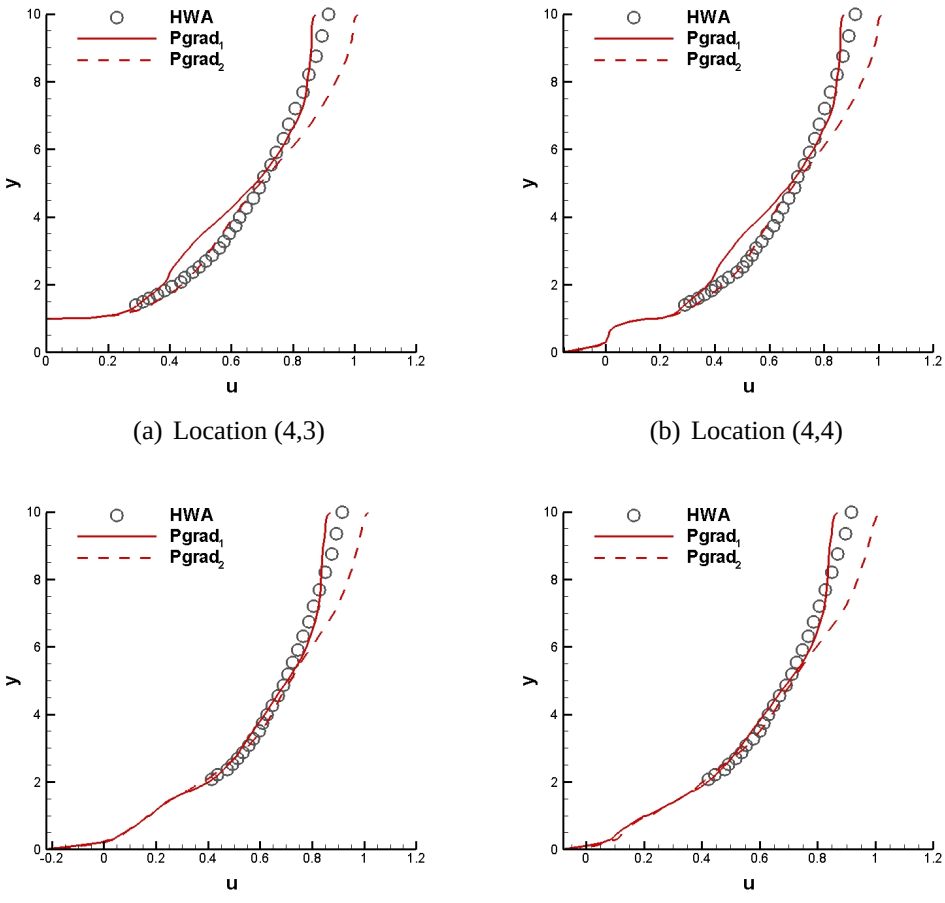

(a) Location (4,3)

(b) Location (4,4)

(c) Location (3,4)

(d) Location (3,3)

Figure 4.11: Pressure gradient dependency in terms of mean statistics.

Figure 4.11 illustrates results obtained at the four locations around B6. Specifically,

at locations (4,3) and (4,4), the profiles attained with the two pressure gradients seem identical at the region below $h_{mean} = 1.0$. However, above B6 their slopes change and as a consequence they cross each other at approximately five times the h_{mean}. Results calculated with P_{grad2} are in very good agreement with the HWA data up to the crossing point where the behaviour changes and the experimental data is now closer to the ILES using P_{grad1}. The mean velocity profiles at positions (3,4) and (3,3), in Figure 4.11(c) and Figure 4.11(d) respectively, are smoother than the previous two locations. They still develop in a different way but they both compare better with the HWA data until they diverge at a higher point of approximately six times h_{mean}. After that point, the velocity magnitude is overpredicted in comparison to the HWA when P_{grad2} is used. Nonetheless, results using P_{grad1} seem to follow the HWA profile in a better way and to reach a slightly underpredicted velocity value at the upper boundary.

Regardless of the position, it is evident that there is a degree of dependency on the choice of the pressure gradient. Based on the fact that increasing the absolute value of $\frac{\partial p}{\partial x}$ led to an overpredicted velocity magnitude at the top boundary, it was decided that further investigations will be conducted using only $\frac{\partial p}{\partial x} = -1.59 Pam^{-1}$.

4.3.2 Reynolds Number Dependency

In the LES study of Xie and Castro [87], it was stated that the Reynolds number dependency is very weak when flows over uniform and non uniform height obstacle arrays are simulated within the range of $Re = 5000$ and $Re = 50000$. The conclusion was based on the fact that the surface drag was mainly pressure drag and that the dominant turbulent scales were comparable to the roughness element scales. Thus, when the flow within the variable height array was simulated at Reynolds numbers of 5000 and 6100 (in the LES study Xie et al. [88] and experimental study of Cheng and Castro [12] respectively), the results were in very good agreement. In order to investigate whether the specific remark could apply to the ILES study, it was decided to proceed with two simulations each one corresponding to the Reynolds numbers mentioned above at a constant pressure gradient $\frac{\partial p}{\partial x} = -1.59 Pam^{-1}$.

Vertical velocity profiles were extracted at locations (4,3), (4,4), (3,3) and (3,4) and compared against HWA data. As shown in Figures 4.12(a) and 4.12(b), both simulations underpredict the velocity profile apart from the area close to the top boundary. At the specific location, the velocity magnitude seems to be predicted well in both cases. However, the simulation performed at Re=5000 gave better results. Slightly different picture can be seen in Figures 4.12(d) and 4.12(c) where the velocity shape and magnitude are predicted accurately when the flow conditions correspond to Re=6100. Nonetheless, at the top boundary, the flow recovers values closer to the ones obtained at Re=5000.

By using information from both sections examining the effects of constant pressure gradient and Reynolds number, it can be concluded that flow within the non uniform height obstacles should be simulated with an imposed pressure gradient of $-1.59 Pam^{-1}$

at Re=6100.

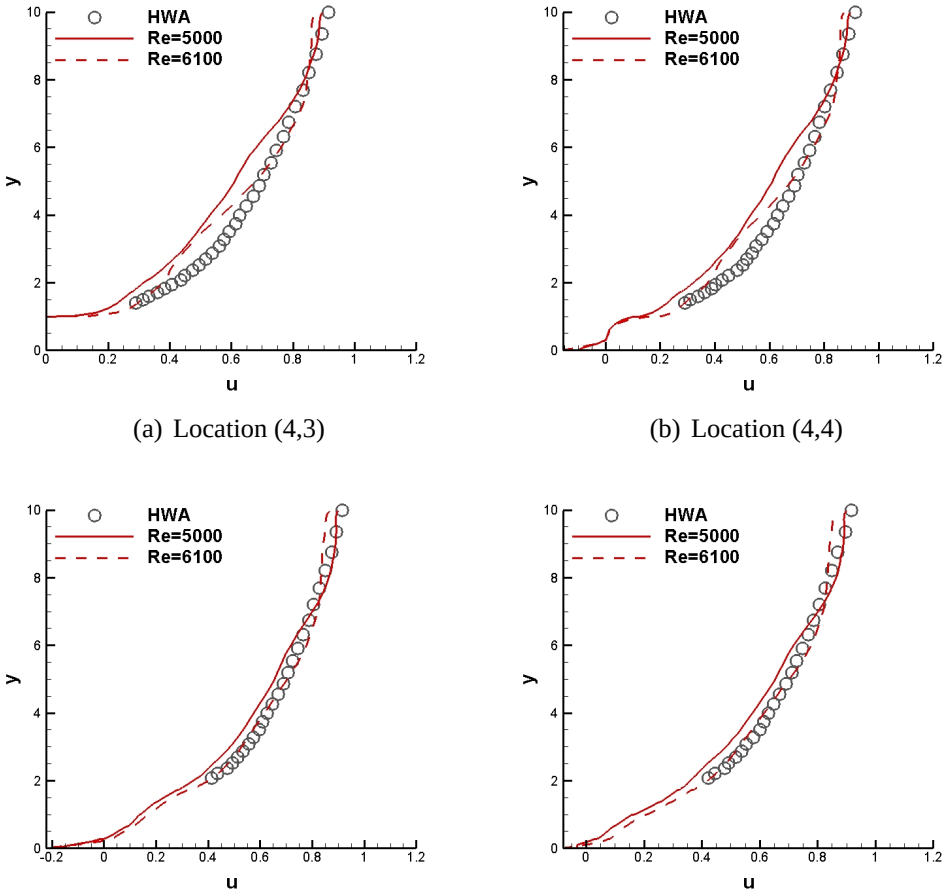

(a) Location (4,3) (b) Location (4,4)

(c) Location (3,4) (d) Location (3,3)

Figure 4.12: Reynolds number dependency in terms of mean statistics.

4.3.3 Obstacle Configuration Dependency

In this section, the effect of the randomness in obstacle height will be presented in terms of mean and spatial averaged velocity profiles. Specifically, mean vertical velocity profiles were extracted in the wake of two buildings of $h_{mean} = 1.0$. The obtained results were compared against HWA and LES data at the same locations and also against the mean velocity profile found in the wake of a cube as described in Chapter 3. Additionally, the spatial mean averaged profile was fitted in the logarithmic law curve and it was plotted against the fitted logarithmic profile found in the four cubes array.

Mean Velocity Profile

Locations (3,2) and (1,6) can be found in Figure 4.10(b). Based on the fact that periodic boundary conditions are imposed along the streamwise and spanwise directions, obstacle B2 ($h = 1$) is considered to be placed in the wake of obstacles B13 ($h = 1.36$) and B14 ($h = 0.64$) and in front of B5 ($h = 0.64$) and B6 ($h = 1.36$). Furthermore, its adjacent obstacles are B1 ($h = 0.28$) and B3 ($h = 1.36$). Element B2 also seems to be surrounded by obstacles of different height ranging between of $B2 \pm 0.36$, with the only exception of B1 which is the lowest obstacle. Element B9, however, is adjacent to obstacles of four different heights, with the biggest difference in height noticed to the B10 ($h = 1.72$).

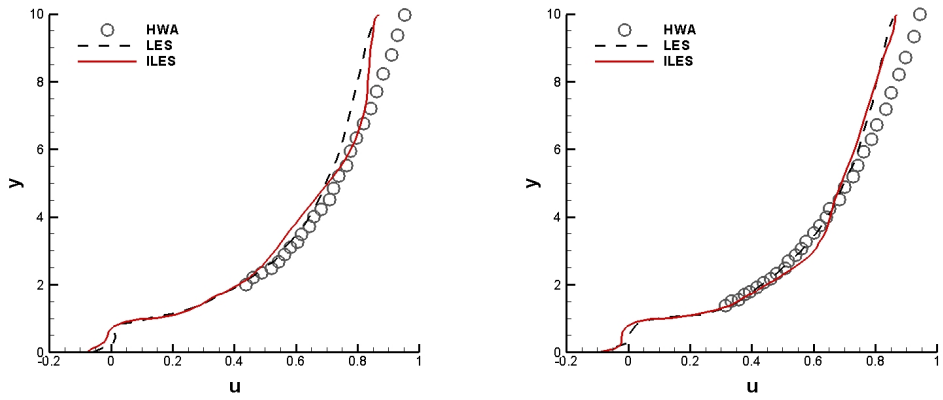

(a) Location (3,2) (b) Location (1,6)

Figure 4.13: Obstacle configuration dependency in terms of mean statistics.

As seen in Figure 4.13(a), the numerical simulations (ILES and LES) seem to predict a similar velocity magnitude up to a certain height, whereas both profiles diverge from the HWA data as the flow approaches the top boundary. Specifically, ILES is in good agreement with the HWA data up to approximately eight times h_{mean} while LES produces slightly better results, but diverges earlier of approximately 6 times h_{mean}. Nonetheless, it can be stated that ILES captured the shape of the velocity profile in an appropriate manner. A different picture is seen in the wake of B6 in Figure 4.13(b).

Both numerical simulations appear to diverge from the HWA data at an even earlier point. Up to four times the mean obstacle height, ILES appears to follow the shape of the HWA profile while after that height the profile becomes steeper. LES and ILES seem to achieve the same velocity value at the top of the domain.

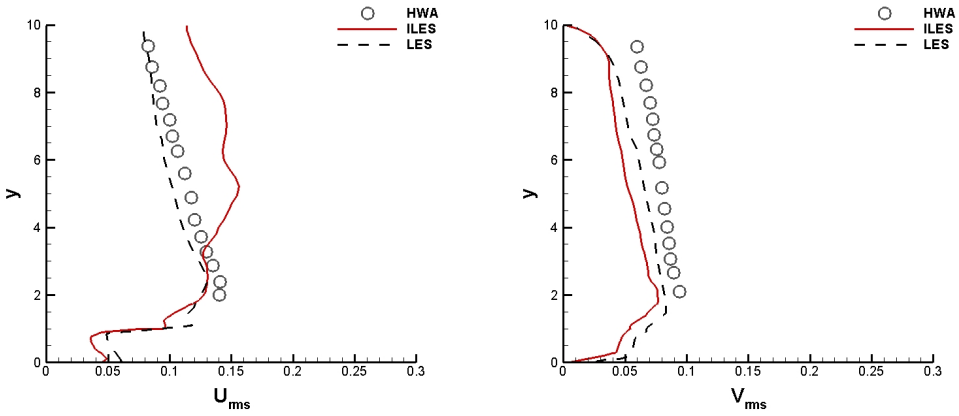

(a) Streamwise Reynolds stresses (b) Crosswise Reynolds stresses

Figure 4.14: Reynolds stresses at location (3,2) - Station A.

Reynolds stresses at Station A are given in Figure 4.14. The streamwise and crosswise stresses are compared against available experimental and LES data. In Figure 4.14(a), ILES appears to follow the LES profile below the height of the highest building however it is lacking in magnitude. The shear layer is underpredicted as well. Above approximately three times the h_{mean}, the ILES U_{rms} profile seems to diverge from the HWA and LES data. One possible explanation could be the reduced resolution above the highest element of the array. Figure 4.14(b) presents comparisons in terms of crosswise Reynolds stresses. Different behaviour is seen here, with the ILES profile having the same shape as LES but relatively less in magnitude. Nonetheless, both numerical methods seem to underpredict the Reynolds stresses when compared against the HWA data.

Figure 4.15 shows comparisons in terms of Reynolds stresses at Station B. In Figure 4.15(a), the streamwise profile appears to be captured better at the specific location. The shape of the profile is predicted correctly up to four times h_{mean}. Past that point and for approximately two times the h_{mean}, the ILES stresses deviate. However the shape of profile is recovered and retained until the top boundary. Figure 4.15(b) shows crosswise Reynolds stresses at Station B. The magnitude of the stresses appears reduced in comparison to the LES and HWA data. The shear layer is predicted at a higher location than expected (near the top boundary of the tallest element of the array). As at Station A (Figure 4.14(b)), both LES and ILES are below the HWA data.

Figure 4.16 shows the comparison between the two profiles obtained over the non uniform obstacle array and the velocity profile behind the cube as found in Chapter 3. To facilitate the comparison, the velocity profiles are shown only up to four times

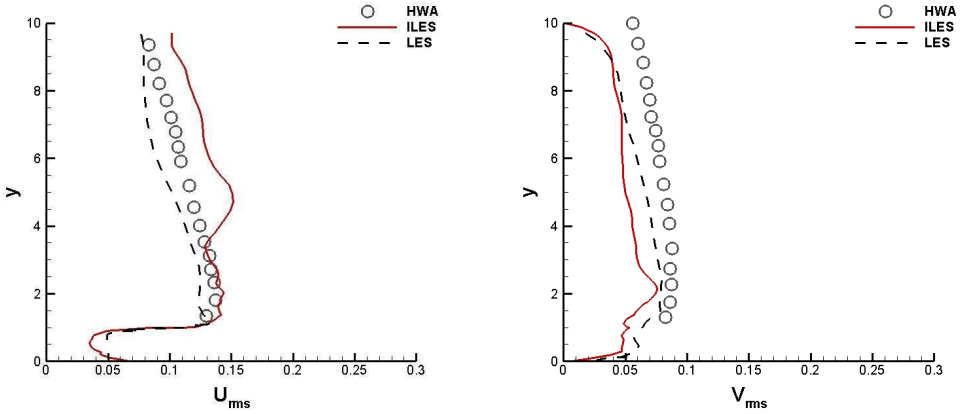

(a) Streamwise Reynolds stresses (b) Crosswise Reynolds stresses

Figure 4.15: Reynolds stresses at location (1,6) - Station B.

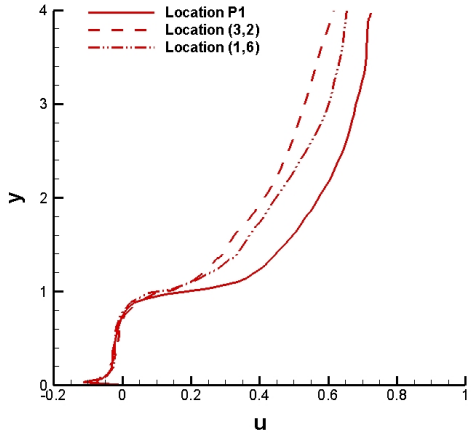

Figure 4.16: Comparison between random and uniform element array.

h_{mean} which corresponds to the top boundary of the four cubes case. There is a clear discrepancy of the velocity profiles in magnitude. The profiles are sharper for the non uniform block array and the velocity values are smaller than the ones seen in the case of the four cubes. Since the top boundary has been lowered to just two times the height of the highest building for the sake of comparison, it can be said the flow has not recovered yet and it is still developing. Thus the velocity magnitude is lower than in the case of the four cubes.

Spatially Averaged Velocity Profile

In this section, the spatially averaged mean velocity profile will be fitted to a logarithmic law curve. Taking the given random and complex geometry into account, it was decided to investigate whether the specific unit could produce enough information so that the logarithmic law wind profile is obtained in the same manner as in the case of the four cubes. Therefore, sixty four locations at heights above the highest element were identified as shown in Figure (4.17).

For simplicity, the acronyms of LDA_UH and HWA_RH will be used when referring to the experimental surface parameters of uniform height and random height array, respectively. Acronyms will also be used for the ILES data. $ILES\_RH2$ and $ILES\_RH3$ represent the parameters obtained using the two and three-parameter fit respectively. Since, both fitting procedures produced similar results for the case of uniform height element array, the cases will be referred as $ILES\_UH$ hereafter.

The information gathered was fitted into a logarithmic curve following two procedures. The first procedure concerns the fit of the spatial averaged velocity profiles using linear regression analysis with least square fitting of two unknown parameters, u_*/U_r and d, while z_0 was set equal to 0.064 as in the experimental study of Cheng and Castro [12]. The second one involved a fit where all three parameters were unknown. The surface parameters were compared against those found in the experimental study of Cheng and Castro [12], but also against the parameters found in the four cubes case. A summary of the surface characteristics obtained from the HWA experiment and ILES, for both uniform and variable obstacle height, is given in Table 4.1.

As seen in Table 4.1, experimental data collected within the inertial and roughness sublayer show that the slope of the velocity profile (given by the ratio u_*/U_r) remains almost identical in the case of the uniform and non uniform array. This is an indication that the shape of the profile is preserved despite the variable element height. However, the values of d and z_0 are higher, stating that the random surface is rougher than the one in uniform height array.

Comparisons between the HWA and ILES data showed that, despite the different linear regression approaches, the values of the surface parameters are reasonable and comparable to the experiment. Specifically, the ratios of u_*/U_r are slightly higher than the HWA ratio. The value of d is underpredicted when z_0 is known, whereas d is overpredicted when z_0 is deduced as well. The difference in both cases is approximately ± 0.2 which corresponds to an approximate average of $\pm 16\%$ as seen in Table 4.2. Finally, the fitted value of z_0 seems to be in very good agreement with the HWA data; an indication that the curve fit with three degrees of freedom is able to produce valid results for the case of random height element array.

Comparisons between the ILES surface parameters within the uniform and non uniform array are shown in Table 4.1. All parameters are higher than in the case of four cubes. However, the slope of the curve does not seem to change significantly within the two arrays. Specifically, it was noted that, when the numerical data is fitted using

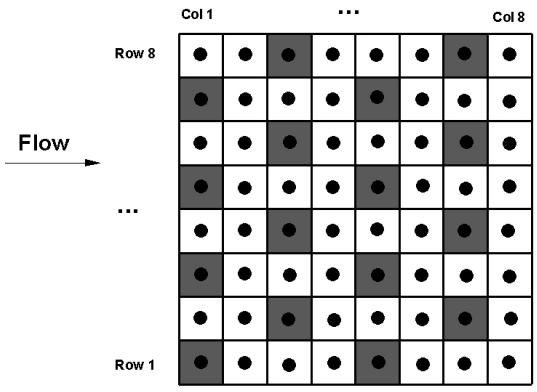

Figure 4.17: Locations of spatial averaged mean velocity profiles.

linear regression with two degrees of freedom, the ratio of u_*/U_r is higher than the one in the four cubes case but also higher than the three parameter fit. Considerably higher are the values of d and z_0. However, this remark is consistent with the idea that the array consists of more elements with ranging heights (thus increased roughness).

Roughness parameters	*LDA_UH*	*HWA_RH*	*ILES_UH2*	*ILES_UH3*	*ILES_RH2*	*ILES_RH3*
u_*/U_r	0.0635	0.0644	0.0652	0.0655	0.06835	0.0675
d	0.835	1.24	0.8203	0.7946	1.065	1.47
z_0	0.0405	0.064	0.0405	0.0419	0.064	0.0675

Table 4.1: Surface parameters obtained from ILES data.

Roughness parameters	*HWA_RHvsILES_RH2*	*HWA_RHvsILES_RH3*
u_*/U_r	6.1%	5%
d	14%	18%
z_0	0%	5.4%

Table 4.2: Percentage difference between ILES and HWA surface parameters.

4.3.4 Energy Spectral Analysis

As described in Chapter 2, the existence of fully developed turbulence can be proven based on Kolmogorov's theory of $k^{-5/3}$ assuming the turbulence as isotropic and homogeneous. To obtain this information, the time signal of instantaneous streamwise velocity was gathered in the wake of five elements, each representing one of the five different block heights. The signal was then transformed using a Fourier series (for

more details revisit Chapter 2) and the results were compared against Kolmogorov's theory as seen in Figure 4.18.

Based on the results, it can be stated that the slope of the velocity signal approaches Kolmogorov's (-5/3) in the wake of the highest building, B10, and not behind B5. The observation is verified by the summary of the energy spectral slopes given in Table 4.3. As seen in Figure 4.10(a), the wake of B5 is dominated by the tallest elements. Thus, the flow requires additional time to reach the fully turbulent stage due to the blockage effect of B10. Using the same argument for the wake of B10, it can be said that the flow adapts quicker to changes due to the presence of shorter buildings, hence Kolmogorov's (-5/3) is finally reached. As mentioned before in Section 3.3.6, the peaks at k=10 is noise.

Schemes	wake of B1	wake of B5	wake of B6	wake of B7	wake of B10
$5thM\_LM$	-1.67	-1.75	-1.68	-1.67	-1.65

Table 4.3: Energy spectral slopes for random height array.

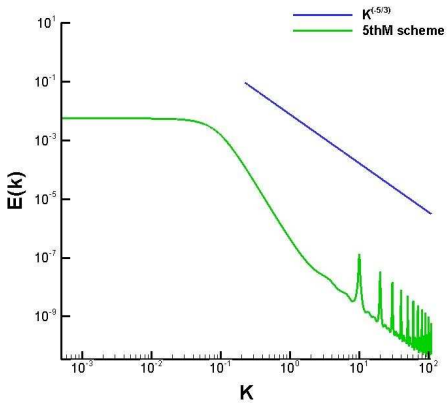

(a) In the wake of B1

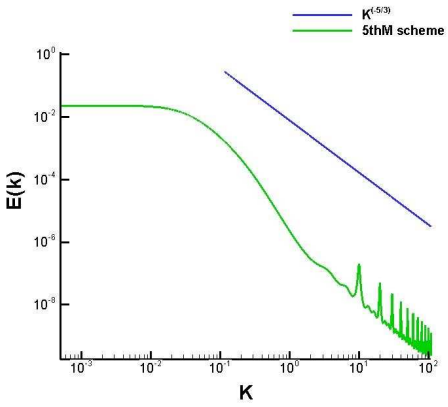

(b) In the wake of B5

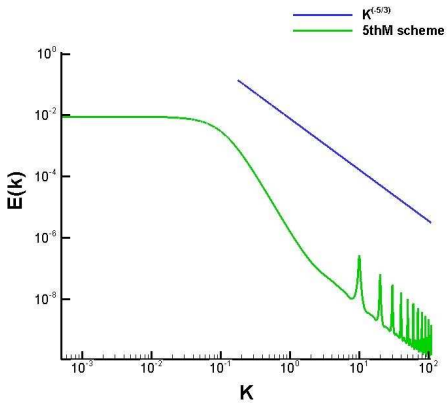

(c) In the wake of B6

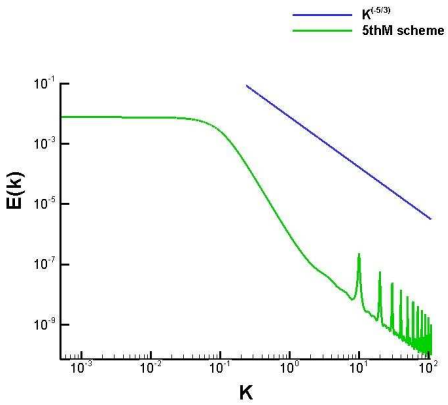

(d) In the wake of B7

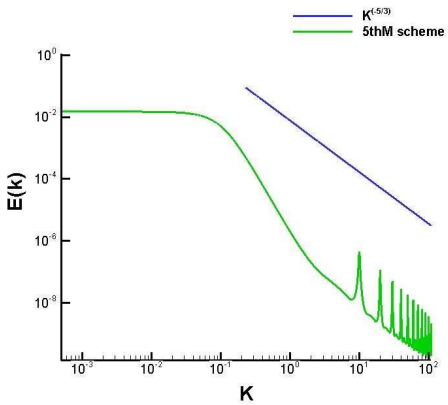

(e) In the wake of B10

Figure 4.18: Energy spectral in non uniform obstacle array.

4.4 Summary

Flows within an array of variable height roughness elements representing real urban environment was investigated in the context of Implicit Large Eddy Simulation. The prediction of such complex flows was examined using the 5^{th} order MUSCL scheme combined with the Low Mach Correction Treatment. The simulations were performed on only one computational grid of 16x16x16 grid points per mean building height.

The effect of the imposed constant pressure gradient was investigated by performing two simulations, with different value of $\frac{\partial p}{\partial x}$. Results obtained in terms of mean velocity statistics showed a dependency on the choice of the pressure gradient. The effect of Reynolds number was also examined at a given constant pressure gradient. Based on the results, it was concluded that different flow conditions produced different magnitude of the velocity profiles, a statement that contradicts the findings of the experimental and LES studies. Detailed information regarding the way that the pressure gradient was imposed in the LES study is not available, therefore, it is not possible to proceed with an explanation regarding those opposite findings.

Mean velocity profiles were extracted in the wake of buildings with the same height in order to investigate the effect of the neighbouring obstacles. The results were compared against HWA and LES data at the same stations, and also with the velocity profile behind a cube as described in Chapter 3. The profiles were found to be steeper and lower in magnitude. To progress it further, the profiles were fitted to a logarithmic curve and the roughness parameters were calculated. The fit produced parameters that were in good agreement with the HWA data. Additionally, the slope of the fitted curve was comparable with the one found in the case of the four cubes. Finally, from the energy spectral analysis, it was found that Kolmogorov's theory of $k^{-5/3}$ is reached slower behind the highest building of the array due to its sheltering effect.

CHAPTER 5

Conclusions and Future Work

IN this thesis, a range of subjects related to the numerical prediction of flow around wall mounted obstacles was covered in the context of Implicit Large Eddy Simulation. The findings of the specific investigation will be presented here. Additionally, suggestions for future work will be given that would increase the reliability of the numerical simulations so that a more accurate representation of reality is produced at a reasonable computational cost.

5.1 Conclusions

Flows in real urban environment are characterised by separation and reattachment due to the wind's interaction with any roughness element, from rocks and trees to building structures. Thus, it produces an excellent testcase for assessing the applicability of Implicit Large Eddy Simulation to the specific type of flows. In the first case under investigation, the performance of high-resolution schemes, namely the 2^{nd} order Van Albada, the 5^{th} order MUSCL, the 5^{th} order WENO and the 9^{th} order WENO, has been assessed for the flow within a uniform height obstacle array in a staggered arrangement. The schemes were used either on the original form or coupled with the Low Mach Correction Treatment which was mainly designed to reduce the excessive dissipation produced by the 5th order MUSCL scheme. In the same context, the effects of the choice of numerical parameters such as grid resolution and temporal discretisation were also investigated. Simulations were performed on three computational meshes with different number of grid points per cube side. The results were compared against available experimental data produced by the Laser Anemometer method and against other numerical studies DNS and LES studies. It was concluded that simulations performed either on the coarse or medium grid produced results which were in very good agreement with the experimental and the numerical data. However, the mean velocity statistics were deteriorating with increasing grid resolution. One possible explanation could be that the production of dissipation could not be adequate enough when high grid resolution grids and high order numerical schemes are combined. The latter observation gave rise to the interest of investigating the numerical scheme dependency in combination with the Low Mach Correction Treatment.

Almost all numerical schemes exhibit similar behaviour and result in very good agreement with the experimental data without being affected by the Low Mach Correction Treatment. However, strong effects were seen when the 9th WENO scheme was used. It appears that the combination of high-order scheme (which could be considered similar to producing results in a very fine grid) and Low Mach Correction Treatment produces over-turbulent results. The specific finding verified the initial thought that high-resolution schemes and Low Mach Correction Treatment may not be always compatible.

As an additional measure of the schemes applicability, the mean vertical velocity profiles were fitted to a logarithmic curve and the roughness parameters characterising the flows were obtained. According to calculations, the 2ndVA and the 5th order MUSCL scheme with Low Mach Correction produced results with the best agreement with LDA data based on shear stresses calculation within the inertial and roughness sublayer. Hence, it was concluded that it is possible to produce accurate results on a relatively coarse grid, given that a high order spatial discretisation scheme is used.

The effect of temporal discretisation was examined as well by reducing the value of CFL in a case using the 9th order WENO scheme. As expected, accurate results can be calculated at high CFL numbers when high order spatial discretisation schemes are used. Finally, energy spectral were calculated from the decomposed instantaneous streamwise velocity signal at specific locations around a cube. From the comparisons with Kolmogorov's theory of $k^{-5/3}$, it was found that the slope of $-5/3$ was approached quicker in the wake of the cube.

In summary, it can be said that ILES was successfully validated against the LDA data for flow over a uniform height obstacles array. The most interesting finding was the part that ILES was proven able to produce results with DNS characteristics on a coarser grid when high order spatial discretisation schemes were employed. This is a very important conclusion because this proves that apart from the simpler formulation of ILES in comparison with the conventional LES, ILES using high resolution methods is capable of producing results at a reasonable computational cost.

The second case under examination considers flow within a more realistic representation of urban areas. Results were obtained by using the 5^{th} MUSCL scheme coupled with the Low Mach Correction Treatment on one only grid resolution since grid resolution and numerical scheme dependency were extensively investigated in the four cubes case. The areas under investigation involved validation of the method of imposing a constant pressure gradient as a driving force in every cell as well as the Reynolds number effects. More specifically, the ILES results revealed that the mean velocity profiles are overpredicted when the case specific pressure gradient is used. Hence, it is believed that presumably the preservation of a constant level of mass flow rate could lead to more consistent results.

Regarding the Reynolds number dependency, it was found that there is indeed a degree of sensitivity that produces different shapes of profiles, a point that contradicts the statement of Cheng and Castro [12] and Xie et al. [88] that flow conditions that

correspond to the Reynolds number range of 5000 to 50000 produce mean and turbulent statistics with insignificant differences. Finally, the mean vertical velocity profiles were spatially averaged and fitted into a curve assuming that logarithmic wind profile is present. The roughness parameters were then obtained and their values were found comparable with the HWA data.

As it was stated in Grinstein et al. [27], although ILES has been proven accurate in simulating classical cases of turbulence such as shock waves and mixing materials, it has not been enough to persuade the scientific community of its applicability for simulating complex flows. With this thesis, it is believed that the point has been made that Implicit Large Eddy Simulation using high-resolution methods is indeed able to accurately reproduce the flow conditions in obstacle arrays representing urban areas without any model modifications.

5.2 Future Work

A considerable amount of work has been produced in this thesis. However, there is always space for improvement. For the case of the staggered array of four cubical elements, further investigation of the discrepancies seen on results obtained with different grid resolutions might be required. The fact that the mass flow rate was found higher than expected on the finer grid leads to the suggestion of using an alternative approach. It might be worth investigating whether maintaining a constant mass flow rate through a variable pressure gradient could be a more appropriate method. The specific suggestion requires additional experimental information which at the present study was not available. Further investigation of the boundary conditions might also be required. The symmetry condition imposed on the top boundary of the computational domain is artificial and does not correspond to the flow conditions found in the boundary layer. The reason for choosing the specific condition was based solely on facilitating direct comparison with DNS and LES studies found in the literature. However, it is proposed to progress the case further and impose conditions that resemble open air conditions such as the farfield condition.

A number of additional investigations is also proposed for flows over variable height roughness elements. Firstly, further investigation is proposed in the direction of increasing the size of the computational domain. According to the four cubical element case, the domain consisted of four times a repeating unit consisting of one element. Therefore, it is suggested to create a larger computational domain which will include four times the existing domain of the non uniform height obstacle array. The intention here is to examine whether the size of the domain affects the outcome of the simulations despite the imposed periodic boundary conditions. Secondly, it would be useful to perform additional simulations with different grid resolutions in order to examine whether the solution deterioration with increasing grid resolution was case specific or it is also present in the non uniform height element array.

Finally, regarding both studies presented in this thesis, it is suggested to proceed with

cases which do not deal exclusively with the height variability. Real urban flow conditions are affected by a number of other parameters such as variability of building shape, alignment and area density (distance between the buildings). Thus, it is believed that combinations of the above parameters will be one of the next steps to be taken in the context of Implicit Large Eddy Simulation of Building Aerodynamics.

Bibliography

[1] http://images.google.com/.

[2] J. D. Anderson. *Computational Fluid Dynamics: The Basics with Applications*. McGraw-Hill, New York, 1995.

[3] Kh. Ashrafi and Gh. A. Hoshyaripour. A Model to Determine Atmospheric Stability and its Correlation with CO Concentration. *International Journal of Environmental Science and Engineering*, 2, 2010.

[4] R.S. Azad. *The Atmospheric Boundary Layer for Engineers*. Kluwer Academic Publishers, 1993.

[5] D. S. Balsara and C.-W. Shu. Monotonicity preserving weighted essentially non-oscillatory schemes with increasingly high order of accuracy. *Journal of Computational Physics*, 160:405–452, 2000.

[6] J Bardina, H Ferziger, and W C Reynolds. Improved Subgrid Scale Models for Large Eddy Simulation. In *13th AIAA Fluid & Plasma Dynamics Conference*, 1980.

[7] G Bartoli and F Ricciardelli. Characterisation of pressure fluctuations on the leeward and side faces of rectangular buildings and accuracy of the quasi-steady loads. *Journal of Wind Engineering and Industrial Aerodynamics*, 2010.

[8] J. P. Boris, F. F. Grinstein, E. S. Oran, and R. L. Kolbe. New insights into large eddy simulation. *Fluid Dynamics Research*, 10:199–228, 1992.

[9] R.E. Britter and S.R. Hanna. Flow and Dispersion in Urban Areas. *Annual Reviews in Fluid Mechanics*, 35:469–496, 2003.

[10] I.P. Castro and A.G. Robins. The Flow around a Surface Mounted Cube in Uniform and Turbulent Stream. *Journal of Fluid Mechanics*, 79:307–335, 1977.

[11] I.P. Castro, H. Cheng, and R. Reynolds. Turbulence over urban type roughness:Deductions from wind-tunnel measurements. *Boundary Layer Meteorology*, 118:109–131, 2006.

[12] H. Cheng and I. Castro. Near wall flow over urban-like roughness. *Boundary-Layer Meteorology*, 104:229–259, 2002.

[13] Y. Cheng, E. Lien, F.S.and Yee, and R. Singlair. A comparison of large eddy simulations with the standard k-e reynolds averaged navier stokes model for the prediction of a fully developed turbulent flow over a matrix of cubes. *Journal of Wind Engineering and Industrial Aerodynamics*, 91:1301–1328, 2003.

[14] O. Coceal, T.G. Thomas, I.P. Castro, and S.E. Belcher. Mean flow and turbulent statistics over groups of urban-like cubical obstacles. *Boundary Layer Meteorology*, 121:491–519, 2006.

[15] A.G. Davenport, C.S.B. Grimmond, T.R Oke, and J Wieringa. Estimating the Roughness of Cities and Sheltered Counrty. In *Conference of Applied Climatology*, 2000.

[16] J.W. Deardorff. A numerical study of three dimensional turbulence channel flow at large Reynolds numbers. *Journal of Fluid Mechanics*, 41:453–480, 1970.

[17] D. Drikakis. Advances in turbulent flow computions using high-resolution methods. *Progress in Aerospace Sciences*, 39:405–424, 2003.

[18] D. Drikakis and W. J. Rider. *High-Resolution Methods for Incompressible and Low-Speed Flows*. Springer, 2004.

[19] D. Drikakis and S. S. Tsangaris. On the solution of the compressible navier-stokes equations using improved flux vector splitting methods. *Applied Mathematical Modelling*, 17:282–297, 1993.

[20] D. Drikakis and S. Tsangaris. Multigrid Scheme for the Compressible Euler Equations. *Journal of Applied Mathematics & Mechanics (Zeitschrift fr Angewandte Mathematik Mechanik; ZAMM)*, 70:663–666, 1990.

[21] D. Drikakis, M. Hahn, A. Mosedale, and B. Thornber. Large-eddy simulation using hgh-resolution and high-order methods. *Phylosophical Transaction of the Royal Society*, 367:2985–2997, 2009.

[22] J. Ehrhard and N. Moussiopoulos. On a new nonlinear turbulence model for simulating flows aroud building-shaped structures. *Journal of Wind Engineering and Industrial Aerodynamics*, 88:91–99, 2000.

[23] C. Fureby, M Liefvendahl, U. Svennberg, L. Persson, and T. Persson. *Implicit Large Eddy Simulation*, chapter 10, pages 301–328. Cambridge University Press, 2006.

[24] J.R. Garratt. *The atmospheric boundary layer*. Cambridge University Press, 1994.

[25] S Ghosal. An Analysis of Numerical Errors in Large Eddy Simulations of Turbulence. *Journal of Computational Fluids*, 125:187–206, 1996.

[26] C.S.B. Grimmond and T.R. Oke. Aerodynamic Properties of Urban Areas Derived from Analysis of Surface Form. *Journal of Applied Meteorology*, 38, 1998.

[27] F. Grinstein, L Margolin, and W. Rider. *Implicit Large Eddy Simulation*. Cambridge University Press, 2006.

[28] F. F. Grinstein, C. Fureby, and C. R. DeVore. On miles based on flux-limiting algorithms. *International Journal for Numerical Methods in Fluids*, 47:1043–1051, 2005.

[29] H. Guillard. Recent developments in the computation of compressible low Mach number flows. *Flow Turbulence and Combustion*, 76:363–369, 2006.

[30] M. Hahn. *Implicit Large Eddy Simulation of Low-Speed Separated Flows Using High-Resolution Methods*. PhD thesis, Cranfield University, 2008.

[31] M. Hahn and D. Drikakis. Implicit Large-Eddy Simulation of Swept-Wing Flow Using High-Resolution Methods. *AIAA Journal*, 47, 2009.

[32] J. Halitsky. Gas diffusion near buildings. *Meteorology and Atomic Energy*, page 221, 1968.

[33] J. Hang, M Sandberg, and Y. Li. Effect of urban morphology on wind condition in idealized city models. *Atmospheric Environment*, 43:869–878, 2009.

[34] A. Harten. High Resolution Schemes for Hyperbolic Conservation. *Journal of Computational Physics*, 49:357–393, 1983.

[35] A. Harten, B. Engquist, S. Osher, and J. Chakravarthy. *Journal of Computational Physics*, 71:231, 1987.

[36] J. He and C.C.S. Song. Evaluation of pedestrian winds in urban area by numerical approach. *Journal of Wind Engineering and Industrial Aerodynamics*, 81:295–309, 1999.

[37] A.K. Henrick, T.D. Aslam, and J.M. Powers. Mapped weighted essentially non-oscillatory schemes:Achieving optimal order near critical points. *Journal of Computational Physics*, 207:542–567, 2005.

[38] J.C.R. Hunt, C.J. Abell, J.A. Peterka, and H. Woo. Kinematical Studies of the Flows Around Free or Surface Mounted Obstacles. Applying Topology to Flow Visualization. *Journal of Fuild Mechanics*, 86:179–200, 1977.

[39] J-Y Hwang and K-S Yang. Numerical study of vortical structures around a wall-mounted cubic obstacle in channel flow. *Physics Of Fluids*, 16, 2004.

[40] J. Jeong and F. Hussain. On the identification of a vortex. *Journal of Fluid Mechanics*, 285:69–94, 1995.

[41] G.-S. Jiang and C.-W. Shu. Efficient Implementation of Weighted ENO Schemes. *Journal of Computational Physics*, 126:202–228, 1996.

[42] M. Kanda, R. Moriwaki, and F. Kasamatsu. Large-eddy simulation of turbulent organized structures within and above explicitly resolved cube arrays. *Boundary Layer Meteorology*, 112:343–368, 2004.

[43] K. H. Kim and C. Kim. Accurate, efficient and monotonic numerical methods for multi-dimensional compressible flows. Part II: Multi-dimensional limiting process. *Journal of Computational Physics*, 208:570–615, 2005.

[44] I.W. Kokkinakis. *Investigation of High Resolution Methods in Large Eddy Simulation of Subsonic and Supersonic Wall Turbulent Flows*. PhD thesis, Cranfield University, 2009.

[45] A. N. Kolmogorov. The local structure of turbulence in incompressible viscous fluid for very large Reynolds number. *Doklady Akademii Nauka SSSR*, 30:299–303, 1941.

[46] S. Krajnovic and L. Davidson. Large-eddy simulation of the flow around a bluff body. *AIAA Journal*, 40, 2002.

[47] T. Kubota, M. Miura, Y. Tominaga, and A. Mochida. Wind tunnel tests on the relationship between building density and pedestrian-level wind velocity: Development of guidelines for realizing acceptable wind environment in residential neighborhoods. *Building and Environment*, 43:1699–1708, 2008.

[48] C. B. Laney. *Computational Gasdynamics*. Cambridge University Press, 1998.

[49] R. J. LeVeque. *Finite Volume Methods for Hyperbolic Problems*. Cambridge University Press, 2002.

[50] Paul A. Libby. *Introduction to Turbulence*. Taylor & Francis, 1996.

[51] X.-D. Liu, S. Osher, and T. Chan. Weighted Essentially Non-oscillatory Schemes. *Journal of Computational Phyics*, 115:200–212, 1994.

[52] N. MacDonald, E. Minty, J. Malard, T. Harding, S. Brown, and M. Antonioletti. Wrinting Message Passing Parallel Programs with MPI. Edinburgh Parallel Computing Centre, University of Edinburgh.

[53] R. Martinuzzi and C. Tropea. The flow around surface mounted prismatic obstacles placed in a fully developed channel flow. *ASME Journal of Fluids Engineering*, 115:85–92, 1993.

[54] E.R. Meinders and K. Hanjalic. Vortex structure and heat transfer in turbulent flow over a wall mounted matrix of cubes. *International Journal of Heat and Fluid*, 20:255–267, 1999.

[55] M Metzger, B. J. McKeon, and h Holmes. The near-neutral atmospheric surface layer: turbulence and non-stationarity. *Philosophical Transactions of the Royal Society*, 365:859–876, 2007.

[56] A. Mosedale and D. Drikakis. Assessment of very high-order of accuracy in les models. *ASME Journal of Fluids Engineering*, 129:1497–1503, 2007.

[57] A.D. Mosedale. *Modelling Shock Induced Instabilities, Transition and Turbulent Mixing using High Order Methods*. PhD thesis, Cranfield University, 2008.

[58] S. Murakami. Comparison of various turbulence models applied to a bluff body. *Journal of Wind Engineering and Industrial Aerodynamics*, 46/47:21–36, 1993.

[59] S. Murakami. Current status and future trends in computational wind engineering. *Journal of Wind Engineering and Industrial Aerodynamics*, 67/68:3–34, 1997.

[60] S. Murakami, K. Uehara, and H. Komine. Amplification of wind speed at ground level due to construction of high rise building in urban area. *Journal of Wind Engineering and I ndustrial Aerodynamics*, 4:343–370, 1979.

[61] P. S. Pacheco. *Parallel Programming with MPI*. Morgan Kaufmann Publishers, San Francisco, 1997.

[62] S. B. Pope. *Turbulent Flows*. Cambridge University Press, 2000.

[63] M. Princevac, J-J Baik, X Li, H Pan, and S-B Park. Lateral channelingwithin-rectangulararraysofcubicalobstacles. *Journal of Wind Engineering and Industrial Aerodynamics*, 2009.

[64] L. F. Richardson. *Weather Prediction by Numerical Process*. Cambridge University Press, 1922.

[65] W. Rodi. Comparison of les and rans calculations of the flow around bluff bodies. *Journal of Wind Engineering and Industrial Aerodynamics*, 69:55–75, 1997.

[66] W. Rodi, J.H. Ferziger, M. Breuer, and M. Pourquie. Workshop on LES of flows past bluff bodies. *Transactions of the ASME.*, 119:248–262, 1995.

[67] M. Roth. Review of atmospheric turbulence over cities. *Q.J.R. Meteorol. Soc*, 126:941–990, 2000.

[68] W. Schofield. Turbulent shear flow over surface mounted obstacles. *ASME Journal of Fluids Engineering*, 112:376–385, 1990.

[69] K. Sedighi and M. Farhadi. Three dimensional study of vertical structure around a cubical bluff body in a channel. *Mechanical Engineering*, 4:1–16, 2006.

[70] K.B. Shah and J.H. Ferziger. A fluid mechanicians view of wind engineering: Large Eddy Simulation of flow past a cubical model. *Journal of Wind Engineering and Industrial Aerodynamics*, 67/68:211–224, 1997.

[71] J. Smagorinsky. General circulation experiments with the primitive equations: I. The basic experiment. *Monthly Weather Review*, 91(3):99–164, March 1963.

[72] T. Stathopoulos and R. Storms. Wind Enviromental Conditions in Passages between Buildings. *Journal of Wind Enginnering and Industrial Aerodynamics*, 24: 19–31, 1986.

[73] T. Stathopoulos and Hanqing Wu. Generic models for pedestrian-level winds in built-up regions. *Journal of Wind Engineering and Industrial Aerodynamics*, 54/55:515–525, 1995.

[74] T. Stoesser, F. Mathey, J. Frohlich, and R. Wolfgang. LES of flow over multiple cubes. *ERCOFTAC Bulletin*, 2003.

[75] R.B. Stull. *An Introduction to Boundary Layer Meteorology*. Kluwer Academic Publishers, 1988.

[76] B Thornber. *Implicit Large Eddy Simulation for Unsteady Multi-Component Compressible Turbulent Flows*. PhD thesis, Cranfield University, 2007.

[77] B. Thornber, D. Drikakis, R.J.R Williams, and D. Youngs. On entropy generation and dissipation of kinetic energy in high resolution shock capturing schemes. *Journal of Computational Physics*, 227:4853–4872, 2008.

[78] B. Thornber, A. Mosedale, D. Drikakis, D Youngs, and R.J.R. Williams. An improved recosntruction method for compressibel flows with low Mach number features. *Journal of Computational Physics*, 227:4873–4894, 2008.

[79] V.A. Titarev and E.F. Toro. Finite Volume WENO schemes for three dimensional conservation laws. *Journal of Computational Physics*, 201:238–260, 2004.

[80] E. F. Toro. *Riemann Solvers and Numerical Methods for Fluid Dynamics – A Practical Introduction*. Springer Verlag, Heidelberg, 1997.

[81] M. Tutar and G. Oguz. Computational modelling of wind flow around a group of buildings. *International Journal of Computational Fluid Dynamics*, 18:651–670, 2004.

[82] B. van Leer. Towards the ultimate conservative difference scheme. Part II: Monotonicity and conservation combined in a second order scheme. *Journal of Computational Physics*, 14:361–370, 1974.

[83] H. K. Versteeg and W. Malalasekera. *An introduction to computational fluid dynamics – The finite volume method*. Addison Wesley Longman Limited, 1995.

[84] J. Von Neumann and RD. Richtmyer. A method for the numerical calculation of hydrodynamic shocks. *Journal of Applied Physics*, 21:232, 1950.

[85] D.C. Wilcox. *Turbulence Modelling for CFD*. DCW Industries ,Inc., 1994.

[86] Z. Xie and I.P. Castro. Large Eddy Simulation for Urban Micro-Meteorology. In *Conference of Global Chinese Scholars on Hydrodynamics*.

[87] Z. Xie and I.P Castro. LES and RANS for turbulent flow over arrays of wall-mounted obstacles. *Flow Turbulence Combust*, 76:291–312, 2006.

[88] Z. Xie, O. Coceal, and I. Castro. Large-Eddy Simulation of Flows over Random Urban-like Obstacles. *Boundary Layer Meteorology*, 129:1–23, 2008.

[89] A. Yakhot, T. Anor, H. Liu, and N. Nikitin. Direct numerical simulation of turbulent flow around a wall mounted cube:spatio-temporal evolution of large scale vortices. *Journal of Fluid Mechanics*, 566:1–9, 2006.

[90] J. Zoltak and D. Drikakis. Hybrid upwind methods for the simulation of unsteady shock-wave diffraction over a cylinder. *Computer Methods in Applied Mechanics and Engineering*, 162:165–185, 1998.

APPENDIX **A**

Viscous Stress Tensor

According to Stoke's hypothesis the summation of the normal stresses is zero in order to maintain equilibrium in a control volume [83]. Therefore the second viscosity coefficient is given by

$$\lambda = -\frac{2}{3}\mu \tag{A.0.1}$$

where λ represents the second viscosity coefficient and μ is the dynamic viscosity of the fluid.

Based on the above hypothesis, the viscous stress components of an isotropic Newtonian fluid can be written as

$$\begin{aligned}
\tau_{xx} &= \left(-\frac{2}{3}\,\mu\, div\,\mathbf{u} + 2\,\mu\,\frac{\partial u}{\partial x} \right), \\
\tau_{yy} &= \left(-\frac{2}{3}\,\mu\, div\,\mathbf{u} + 2\,\mu\,\frac{\partial v}{\partial y} \right), \\
\tau_{zz} &= \left(-\frac{2}{3}\,\mu\, div\,\mathbf{u} + 2\,\mu\,\frac{\partial w}{\partial z} \right), \\
\tau_{xy} &= \tau_{yx} = \mu \left(\frac{\partial u}{\partial y} + \frac{\partial v}{\partial x} \right), \\
\tau_{xz} &= \tau_{zx} = \mu \left(\frac{\partial u}{\partial z} + \frac{\partial w}{\partial x} \right), \\
\tau_{yz} &= \tau_{zy} = \mu \left(\frac{\partial v}{\partial z} + \frac{\partial w}{\partial y} \right).
\end{aligned}$$

APPENDIX **B**

Reynolds Stresses Comparisons With LDA Data

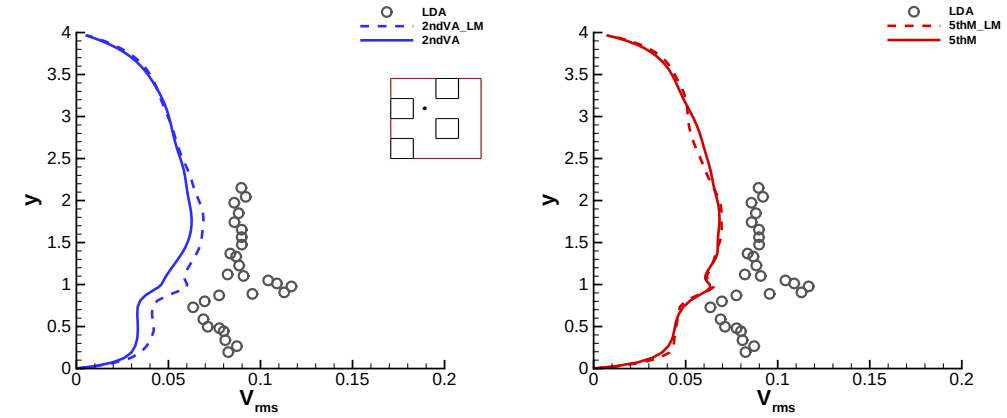

(a) 2nd Order MUSCL with Van Albada limiter

(b) 5th Order MUSCL

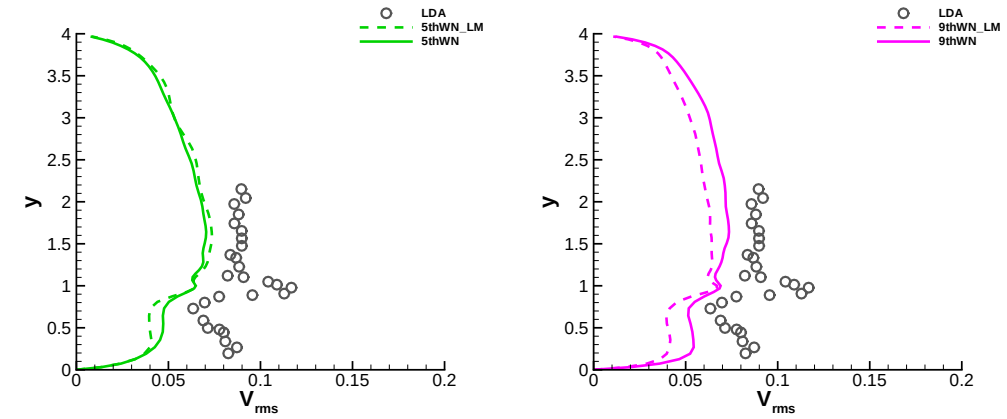

(c) 5th Order WENO

(d) 9th Order WENO

Figure B.1: Time-averaged crosswise stresses at location p1.

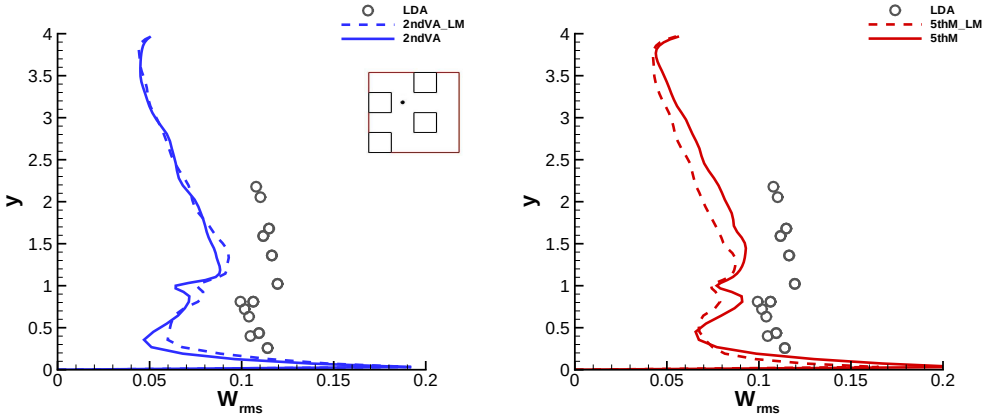

(a) 2nd Order MUSCL with Van Albada limiter

(b) 5th Order MUSCL

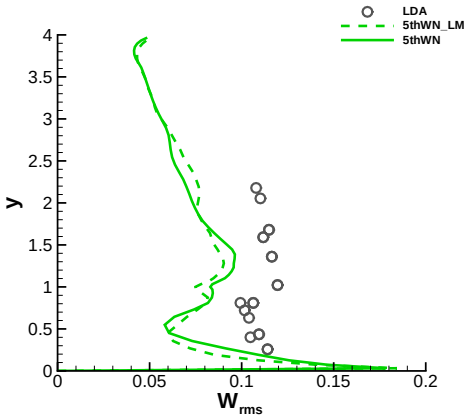

(c) 5th Order WENO

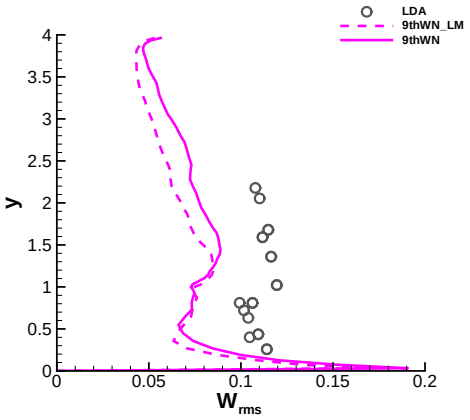

(d) 9th Order WENO

Figure B.2: Time-averaged spanwise Stresses at location p1.

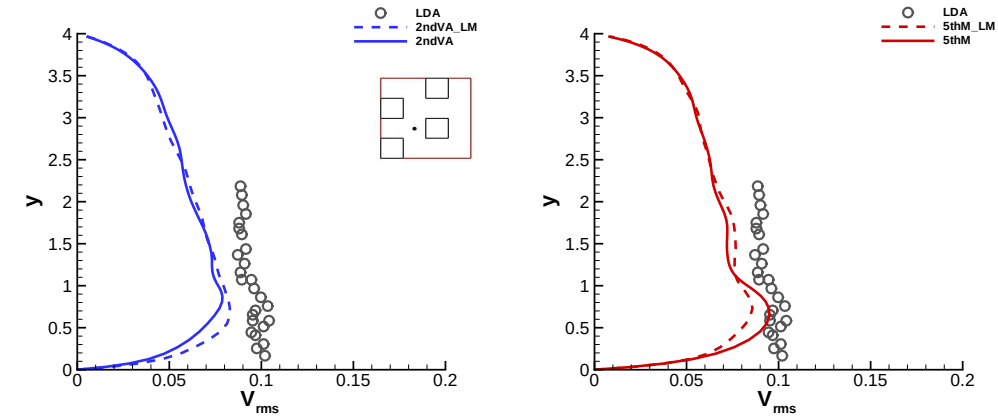

(a) 2nd Order MUSCL with Van Albada limiter (b) 5th Order MUSCL

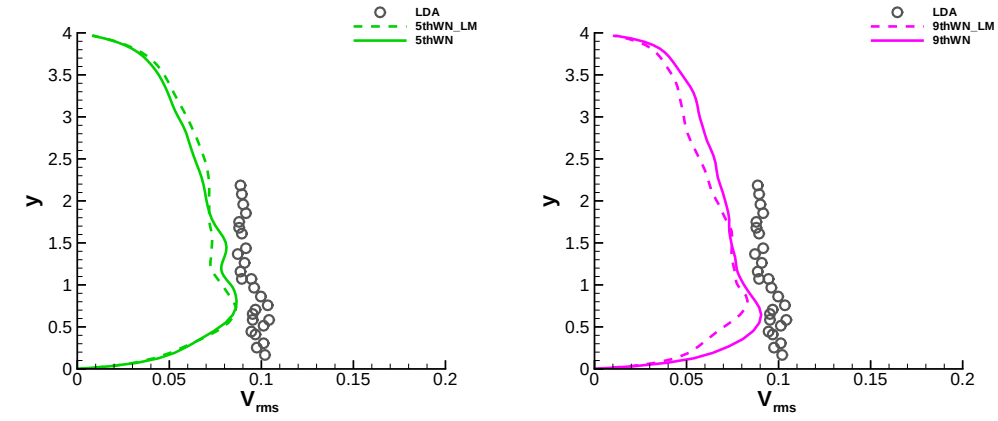

(c) 5th Order WENO (d) 9th Order WENO

Figure B.3: Time-averaged crosswise stresses compared against LDA data at location p2.

APPENDIX C

Reynolds Stresses Comparisons With DNS and LES Data

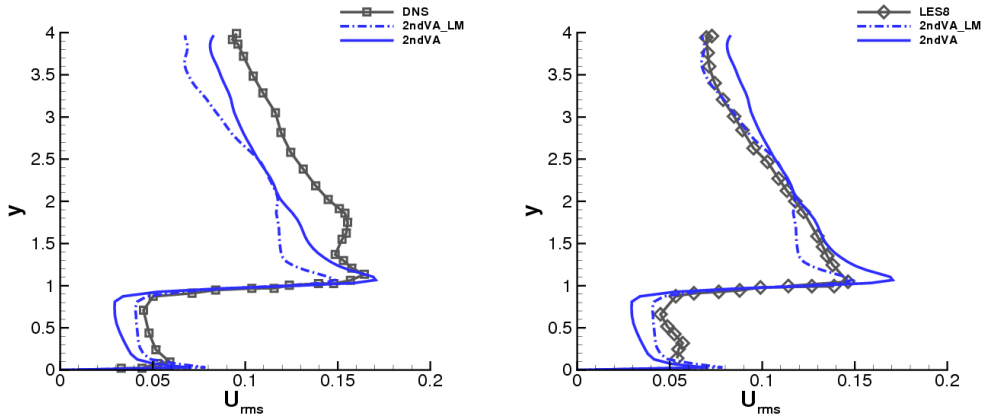

(a) ILES16 vs DNS 2ndVA

(b) ILES16 vs LES8 2ndVA

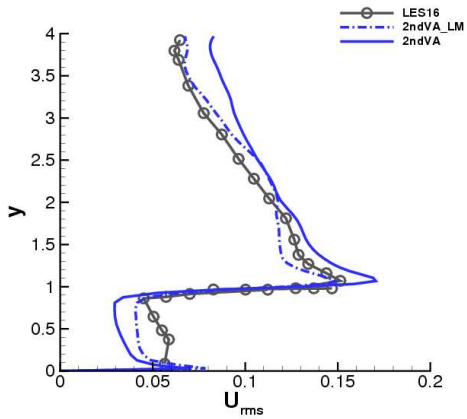

(c) ILES16 vs LES16 2ndVA

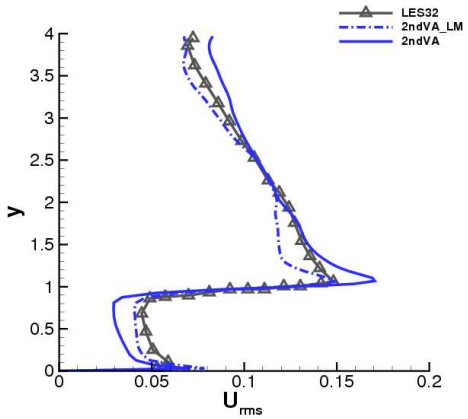

(d) ILES16 vs LES32 2ndVA

Figure C.1: Time-averaged turbulent intensities obtained with 2ndVA scheme at location p1.

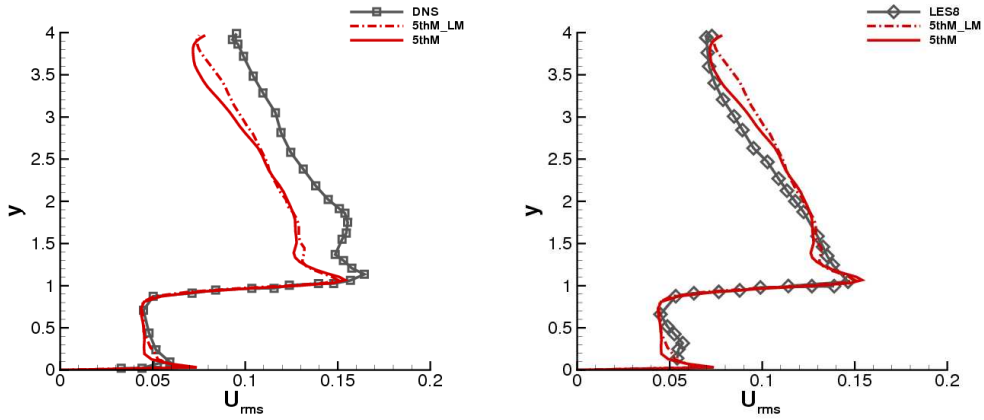

(a) ILES16 vs DNS 5thM

(b) ILES16 vs LES8 5thM

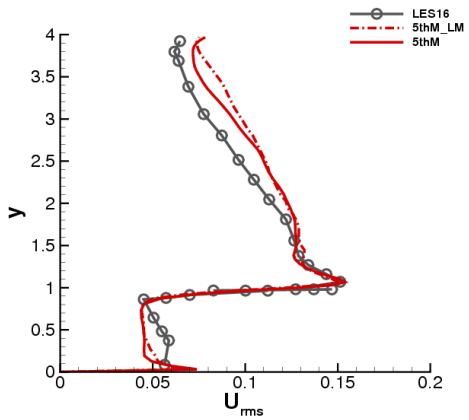

(c) ILES16 vs LES16 5thM

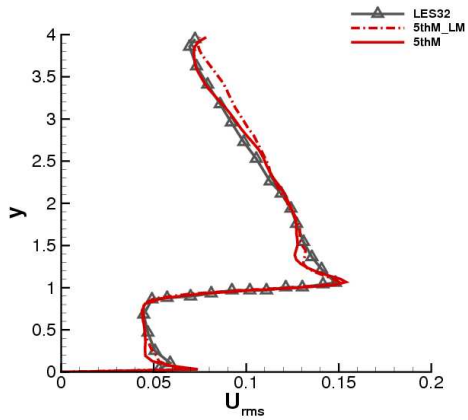

(d) ILES16 vs LES32 5thM

Figure C.2: Time-averaged turbulent intensities obtained with 5thM scheme at location p1.

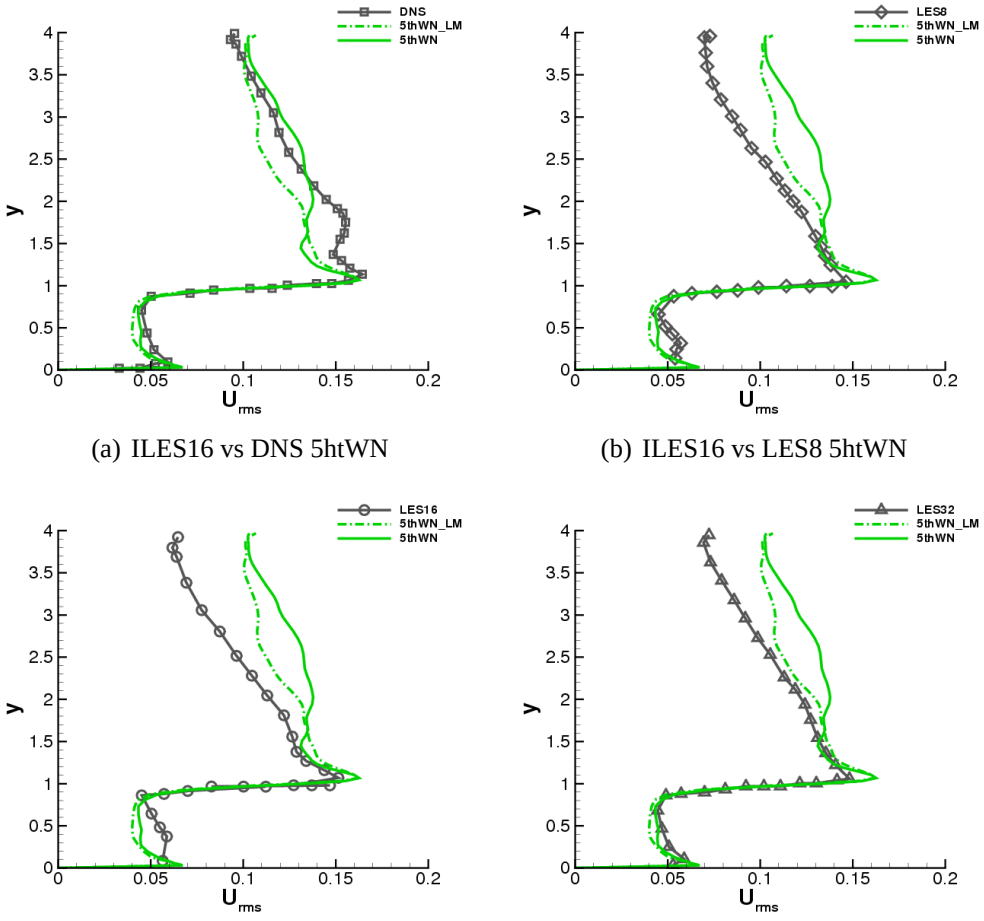

(a) ILES16 vs DNS 5htWN (b) ILES16 vs LES8 5htWN

(c) ILES16 vs LES16 5htWN (d) ILES16 vs LES32 5htWN

Figure C.3: Time-averaged turbulent intensities obtained with 5thWN scheme at location p1.

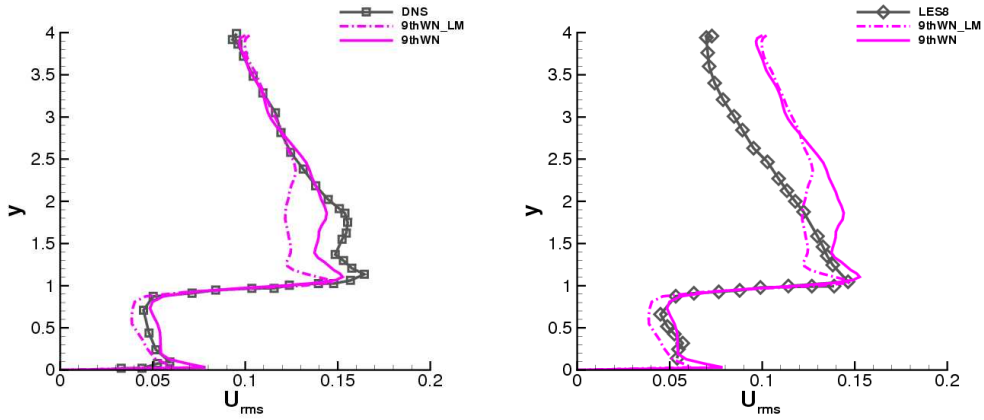

(a) ILES16 vs DNS 9htWN

(b) ILES16 vs LES8 9htWN

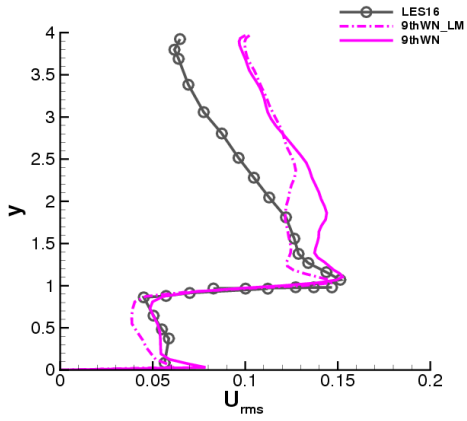

(c) ILES16 vs LES16 9htWN

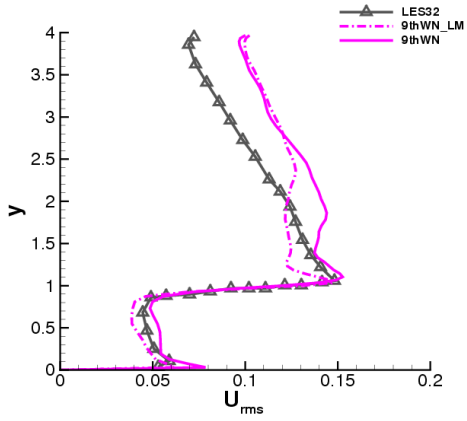

(d) ILES16 vs LES32 9htWN

Figure C.4: Time-averaged turbulent intensities obtained with 9thWN scheme at location p1.